

ABSTRACT

Title of dissertation: IR DETECTION AND ENERGY
HARVESTING USING ANTENNA
COUPLED MIM TUNNEL DIODES

Filiz Yesilkoy, PhD Dissertation, 2012

Dissertation directed by: Professor Martin Peckerar
Department of Electrical
and Computer Engineering

The infrared (IR) spectrum lies between the microwave and optical frequency ranges, which are well suited for communication and energy harvesting purposes, respectively. The long wavelength IR (LWIR) spectrum, corresponding to wavelengths from $8\mu m$ to $15\mu m$, includes the thermal radiation emitted by objects at room temperature and the Earth's terrestrial radiation. Therefore, LWIR detectors are very appealing for thermal imaging purposes. Thermal detectors developed so far either demand cryogenic operation for fast detection, or they rely on the accumulation of thermal energy in their mass and subsequent measurable changes in material properties. Therefore, they are relatively slow. Quantum detectors, allow for tunable and instantaneous detection but are expensive and require complex processes for fabrication. Bolometer detectors are simple and cheap but do not allow for tunability or for rapid detection.

Harvesting the LWIR radiation energy sourced by the Earth's heating/cooling cycle is very important for the development of mobile energy resources. While speed

is not as significant an issue here, conversion efficiency is an eminent problem for cheap, large area energy transduction. This dissertation addresses the development of tunable, fast, and low cost wave detectors that can operate at room temperature and, when produced in large array format, can harvest Earth's terrestrial radiation energy.

This dissertation demonstrates the design, fabrication and testing of Antenna Coupled Metal-Insulator-Metal (ACMIM) tunnel diodes optimized for $10\mu m$ wavelength radiation detection. ACMIM tunnel diodes operate as electromagnetic wave detectors: the incident radiation is coupled by an antenna and converted into a 30 Terahertz signal that is rectified by a fast tunneling MIM diode. For efficient IR radiation coupling, the antenna geometry and its critical dimensions are studied using a commercial finite-element based multi-physics simulation tool, and the half-wave dipole-like bow-tie antennas are fabricated using simulation-optimized geometries.

The major challenge of this work is designing and fabricating MIM diodes and coupled antennas with internal capacitances and resistances small enough to allow response in the desired frequency range (~ 30 THz) and yet capable of efficiently coupling to the incident radiation. It is crucial to keep the RC time constant of the tunnel junction small to achieve the requisite cut-off frequency and adequate rectification efficiency. Moreover, a low junction resistance is necessary to load the coupled AC power across the MIM junction. For energy harvesting applications, the device has to operate without an external bias, which requires asymmetry at the zero bias operation point. To address these requirements, the MIM tunnel junction is established so that one electrode has a field enhancing sharp tip (cathode) and the

other is a rectangular patch. This asymmetric geometry not only offers asymmetric current-voltage behavior at the zero bias point, but also it decouples the junction resistance and capacitance by concentrating the charge transport in a small volume around the tip.

Various fabrication methods are developed in order to create small junction area (= low parasitic capacitance), low junction resistance (= effective power coupling through antenna), asymmetry (= zero bias operation), high fabrication yield and low cost ACMIM tunnel diodes. High resolution fabrication needs are accomplished by electron-beam lithography and nano-accuracy in the junction area is achieved by employing dose modifying proximity effect correction and critical alignment methods. Our Ni/NiO_x/Ni ACMIM diodes with an optimized insulation layer created with O₂ plasma oxidation are the most successful devices presented to date. A novel fabrication technique called “strain assisted self lift-off process” is used to achieve small junction area devices without relying on lithographic resolution. This technique eliminates the rival parasitic capacitance issue of today’s ACMIM tunnel diodes and does not rely on extreme-high resolution lithography technologies.

IR DETECTION AND ENERGY HARVESTING USING
ANTENNA COUPLED MIM TUNNEL DIODES

by

Filiz Yesilkoy

Dissertation submitted to the Faculty of the Graduate School of the
University of Maryland, College Park in partial fulfillment
of the requirements for the degree of
Doctor of Philosophy
2012

Advisory Committee:
Professor Martin Peckerar/Advisor
Professor Mario Dagenais
Professor Christopher Davis
Professor Neil Goldsman
Professor Jeremy Munday
Professor Lourdes Salamanca-Riba

© Copyright by
Filiz Yesilkoy
2012

I dedicate this thesis to my parents, Ayse and Ergun Yesilkoy, for their unconditional love and infinite support throughout my life.

Acknowledgements

I would like to express my sincere gratitude to my advisor, Prof. Martin Peckerar, for the continuous support, patience, and enthusiasm he has provided during my time at Maryland. I feel extremely lucky to have been mentored by someone with deep knowledge, solid experience and infinite motivation to learn, investigate and invent.

I would also like to thank all the members of my PhD committee for generously devoting time to judge my work and providing insightful comments.

I would like to express my deep gratitude to CoolCAD Electronics and to Dr. Siddharth Potbhare for allowing us to use their CO_2 source, measuring tools and techniques developed by CoolCAD for evaluation of my ACMIM diodes. I would also like to acknowledge the staff of CoolCAD for many interesting and useful discussions on the subject of the work presented here.

I have had the privilege to collaborate with many people at the ECE Department in the last five years. Particularly, I would like to thank to Dr. Kwangsik Choi for generously training me in the cleanroom, Vincent De Chacus for coding data analysis software, and Nick Kratzmeier for patiently working with me on the simulation part of my thesis. I would also like to dearly thank to my fellow labmates Scott Bauman, Gavin Liu, Wei Zhao, Sunil Mittal, Mahsa Dornajafi, Shahrzad Salemi, and Jeyron Amirloo. Also, many thanks to the FABLAB staff, particularly Tom Loughran, John Abrahams, and Jon Hummel for teaching me nanofabrication, fixing the tools magically fast, and most importantly entertaining me with their cutest

jokes while I am involved in serious work.

Even though I was far away from home and family during my time at Maryland, I had great friends that became family to me. I would like to thank Anita Roychowdhury, Ayanah George, Federica Rangel, John Biddle, Juliana Dutra, Marcos Vasconcelos, Nima Mesgarani, Ranit Sengupta, Sevil Altiparmak, and Sowmya Subramanian for being there to cheer me up whenever I was down and to share the happy moments. I would also like to present my deepest gratitude to Vera Romero and Tulio Arvelo for providing me with a warm home during their visits to US and treating me as their daughters.

I would like to thank Gulden Gun, Dilek Uludag, Sebnem Tuncdemir, Hatice Sinem Sas, and Timir Datta, for helping me grow as a person and a researcher. They have been and will always be my mentors and best friends.

I am deeply thankful for having a wonderful family who has sacrificed a lot to bring me to where I am today. I could not have done this without the unconditional love and infinite support of my parents, Ayse and Ergun, my brother Hakki, my grandmother Hatice, and my grandparents Havva and Halil, both of whom I lost during my doctoral study.

I would like to close by saying that the best thing that happened to me in these past five years was meeting my boyfriend, Eduardo Arvelo. I cannot convey my feelings to him in words. He has been a best friend who accepts me as I am, a most loyal colleague who helps me find my way whenever I am lost, and a family member who is always proud of me and has infinite faith in me. He has been and will always be my inspiration in life!

Table of Contents

1	Introduction	1
1.1	Motivation	2
1.1.1	Infrared Detection	3
1.1.2	Infrared Energy Harvesting from Terrestrial Radiation	5
1.2	ACMIM Tunnel Diode Design Specifications	8
1.3	Thesis Contribution	11
1.4	Thesis Organization	12
2	Background	14
2.1	ACMIM Diodes in the Literature	14
2.1.0.1	Point Contact MIM Diodes	14
2.1.0.2	Thin Film MIM Diodes	16
2.1.0.3	Recent Technologies in Thin Film MIM Diodes	17
2.2	Conduction Mechanisms in Thin Films	22
2.3	Rectification Analysis	28
2.4	Rectenna Design	32
2.5	Total Efficiency Estimation	37
2.6	Summary	41
3	Finite Element Simulation Results	43
3.1	Electrostatic Simulation Results	43
3.1.1	Mesh Density Analysis	44
3.1.2	Tip Radius Analysis	45
3.1.3	Gap Width Analysis	50
3.1.4	Flare Angle Analysis	51
3.1.5	Capacitance Analysis	53
3.1.6	Imperfection Effects	55
3.2	Time-Dependent Simulation Results	59
3.2.1	Antenna Length Optimization	63
3.2.2	Polarization Effects	65
3.2.3	Substrate and Air Coupling Comparison	66
3.3	Summary	68
4	Fabrication	71
4.1	Substrate	71
4.2	Electron Beam Lithography (EBL)	73
4.2.1	EBL Proximity Effect Control	74
4.2.1.1	Implementation of PEC Method on Planar ACMIM Diodes	74
4.2.1.2	Adapting PEC to ACMIM Patterning	77
4.2.2	EBL Aligning	78
4.3	Materials	80
4.3.1	Ni Oxidation Methods	82

4.4	Fabrication Methods	84
4.4.1	Single Step Lithography	85
4.4.1.1	Polysilicon/ SiO_2 /Polysilicon Planar ACMIM Tunnel Diodes	85
4.4.1.2	Ni/NiOx/Ni Planar ACMIM Tunnel Diodes	87
4.4.2	Double Step Lithography	88
4.4.2.1	Ni/NiOx/Ni ACMIM Tunnel Diodes	89
4.5	Packaging	93
4.6	Summary	98
5	Experimental Results	100
5.1	DC Current-Voltage Analysis	100
5.1.1	Single-Step Lithography ACMIM Diodes	103
5.1.2	Statistical Analysis on Double-Step Lithography Ni/NiOx/Ni ACMIM Diodes	104
5.1.2.1	Junction Area Effects	105
5.1.2.2	Oxidation Method Selection	109
5.1.2.3	Asymmetry Analysis	115
5.1.2.4	Process Variation Analysis	115
5.1.2.5	Time Variation Analysis	119
5.2	RF Response	120
5.3	IR Response	121
5.3.1	IR Test Set-up	122
5.3.2	IR Detection Results	124
5.4	IR Detector Performance: Figures of Merit	131
5.4.1	Responsivity	131
5.4.2	Signal-to-Noise Ratio	133
5.4.3	Noise Equivalent Power	133
5.4.4	Detectivity	134
5.5	Summary	136
6	Conclusions and Suggestions for Further Work	138
A	MIM Conduction Mechanisms	142
A.1	Field-Assisted Tunneling Current	142
A.2	Thermionic Emission Current	143
A.3	Poole-Frenkel Effect	144
B	Proximity Effect Correction using Linear Programming Methods	146
B.1	Electron Solid Interactions	146
B.2	Mathematical Modeling of Electron Beam	147
B.3	Physical Factors Affecting the PSF	148
B.4	A Mathematical Formal Statement of Proximity Effect Problem	150
B.5	Mathematical Redefinition of the PE as a Linear Optimization Problem	153

Chapter 1

Introduction

Antenna Coupled Metal-Insulator-Metal (ACMIM) tunnel diodes are attractive candidates for future infrared (IR) detectors and IR energy harvesters. They push the limits of the fastest rectification operation via tunneling. The small dimensions of diode minimizes parasitic capacitance and resistance. The antenna-diode combination (also known as a rectenna) operates as a frequency sensitive wave detector. The micro-scale antenna couples the incident IR wave and loads the MIM junction with AC power. The tunnel diode, having the ability to operate at terahertz frequency, performs the rectification of the oscillating charge across the insulating thin film between the metal antenna parts and returns a DC signal to be detected. The ACMIM structure is shown in figure 1.1.

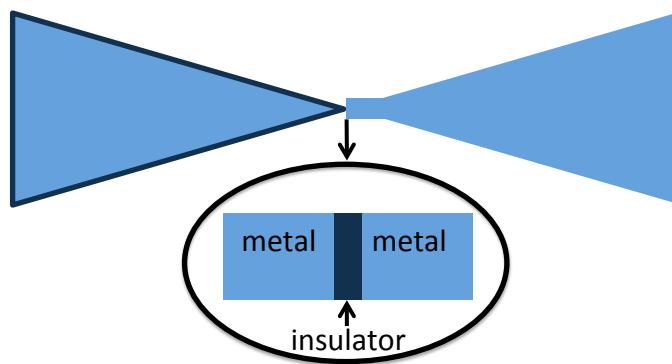


Figure 1.1: ACMIM tunnel diode schematic.

1.1 Motivation

We propose two main applications for the ACMIM diodes: 1) IR detection, and 2) IR energy harvesting. The main operational difference between ACMIM diodes used as IR detectors and those used as harvesters arises in the operating bias point. For energy harvesting purposes, the device must be operated at zero external bias. On the other hand, for detection applications the highest responsivity point can be tuned to maximize the detection efficiency. Therefore, using ACMIM diodes as IR harvesters is more challenging than using them as IR detectors. For example, it requires an asymmetric tunnel diode current-voltage relation across the zero bias to create zero diode turn-on point for rectification. Also, since the responsivity at zero bias is strictly determined by the asymmetry, the rectification efficiency is much lower than the maximum nonlinear point. The design we propose in this dissertation addresses all these requirements and it is suitable for IR detection and energy harvesting.

In spite of the mature microbolometer technology that leads the IR detector market, there is high demand for affordable, efficient, room temperature operating detectors [46]. IR imagers are of great interest to both military (surveillance, target detection & tracking) and civilian needs. For example, IR cameras are used by firefighters to see through smoke. Moreover, IR detector arrays are used at space observatories to investigate planetary atmospheres and interstellar material compositions. According to David Leisawitz from NASA-GSFC, 98 % of the photons released since the big-bang lie in the sub millimeter and far-IR [3].

On the other hand, harvesting Earth’s reradiating solar energy that peaks at $10\mu m$ wavelength is highly desirable. Since Bailey proposed harnessing the solar energy using RF rectification techniques in 1972 [30], research on IR energy harvesting has thrived [29],[20]. Berland et al. was the first to use fast MIM tunnel diodes to rectify the antenna coupled IR radiation [4]. Despite the continuous research efforts on IR harvesting, there has been no record showing direct IR energy conversion from the ambient. Figure 1.2 shows a scheme of ACMIM diodes array construction.

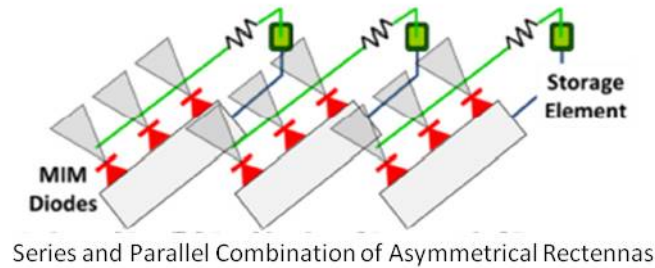


Figure 1.2: ACMIM array construction.

1.1.1 Infrared Detection

Long wave infrared (LW-IR) detectors that can operate at $10\mu m$ wavelength (our particular wavelength of interest) can be analyzed under three different categories: thermal detectors, quantum detectors, and wave detectors. Thermal detectors, fabricated using micro-electro-mechanical (MEMS) technology, operate by monitoring a physical change in the material as a result of the temperature increase due to the incident electromagnetic wave. Thermocouples that function based on the Seebeck Effect and bolometers that sense the change in the resistivity of a material are the two most common thermal IR detectors. Thermal detectors do not perform

instantaneous detection, and do not provide particular incident wavelength information because they have slow response time and sense the accumulated incident power integrated over wavelength. However, they can operate at room temperature and are relatively low-cost devices.

Quantum detectors make use of quantum confinement to create “bandgap engineered” solids with pre-determined energy levels not usually found in nature. Photon energy at LW-IR frequencies are smaller (at $10\mu mE = 0.12eV$) than the band gap of common semiconductors such as Si ($1.11eV$), Ge ($0.67eV$), GaAs($1.43eV$). Therefore, IR can only excite electron-hole pairs in extremely small band gap semiconductors, such as Mercury Cadmium Telluride (HdCdTe) or MCT, which are synthesized by alloying multiple elements. The detection mechanism can either be done by applying a potential and measuring current change (photo-conductors) or by charge collecting through a potential barrier as in photovoltaics. Quantum Well Infrared Photodetectors (QWIPs) are also common in LW-IR detection. These devices are made by sandwiching a small band-gap semiconductor in between two large band-gap semiconductors creating a quantum well.

The incident IR photons cause inter-sub-band excitation of electrons in the quantum well and these excited electrons can be detected as a result of the conductivity variation in the material. Quantum detectors instantaneously sense the change that is caused by the incident photons. In addition, they can be tuned so that a very narrow IR frequency range is detectable. However, for extraordinary high sensitivity and fast response, quantum detectors must be operated at cryogenically cooled temperatures because even the room temperature phonon energy can excite

electrons in these small band-gap semiconductors, creating noise and degrading the detection [27], [46].

IR wave detectors exploit the wave nature of the incident electromagnetic waves and use properly designed antennas to detect the incident power in a narrow frequency band. Moreover, they are fast detectors because the coupled power is simultaneously rectified by the tunnel diode. They can operate at room temperature because tunneling, not thermally excited electrons, dominates the detection mechanism. The antenna coupled tunnel diodes, which is the main focus of this study, fall into the wave detectors category. Offering room temperature operation, tunability, and fast response, wave detectors bring the advantages of thermal detectors and quantum detectors together on a simple, cheap and CMOS compatible design. As a result, antenna coupled MIM tunnel diodes are the only candidates that meet the needs of IR detection technology.

1.1.2 Infrared Energy Harvesting from Terrestrial Radiation

Objects above the absolute zero of temperature radiate IR waves in order to reach a thermodynamic equilibrium. The total IR energy radiated from the surface of an object and the spectrum of this radiation have been well studied and summarized by the “Planck Radiation Law”, the “Stefan-Boltzmann Law”, and the “Wien Displacement Law”. The electromagnetic spectrum on the Earth’s surface has two energy peaks, created by the blackbody radiation of the Sun and of the Earth, corresponding to their temperatures. The peak generated by the Sun’s ra-

diation (also called short-wave radiation) occurs in the visible range ($\lambda = 0.5\mu m$), and the Earth's radiation (also called long-wave radiation or Terrestrial radiation) occurs at the LW-IR ($\lambda = 10\mu m$).

The total solar radiation flux that strikes the Earth's outer tangential surface with a 90 degree incidence angle can be calculated as $1377W/m^2$, considering the radius of the Sun and the Earth, and also the distance in between. However, only 51% of the incident flux is absorbed by the land and oceans due to atmospheric absorption and reflection, which is schematically illustrated in Figure 1.3.

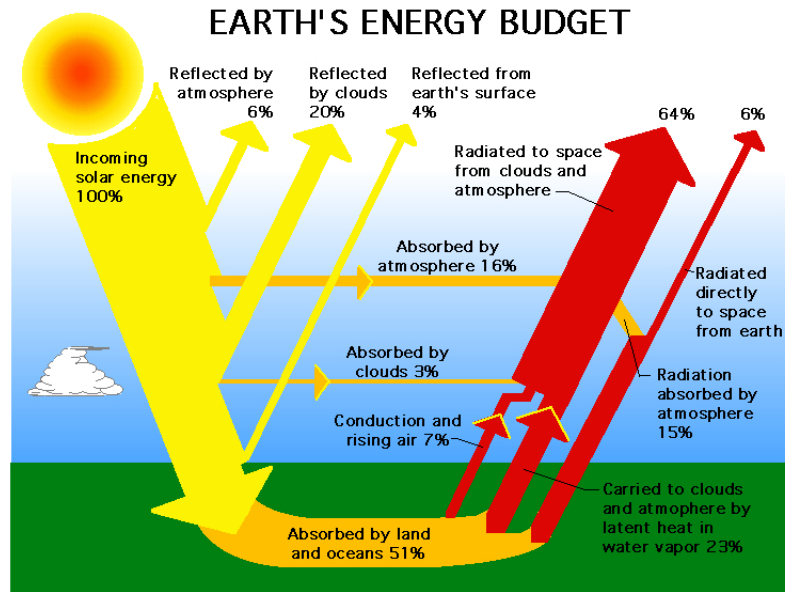


Figure 1.3: Solar radiation energy distribution at the Earth by Frank van Mierlo from <http://education.gsfc.nasa.gov>.

The solar energy that is absorbed by the Earth brings the planet to a thermal equilibrium and the Earth reradiates at a longer wavelength. Both the long-wave and the short-wave radiation flux spectrum can be seen in Figure 1.4, which shows that between $7\mu m$ to $13\mu m$ there exists about $100W/m^2$ energy flux.

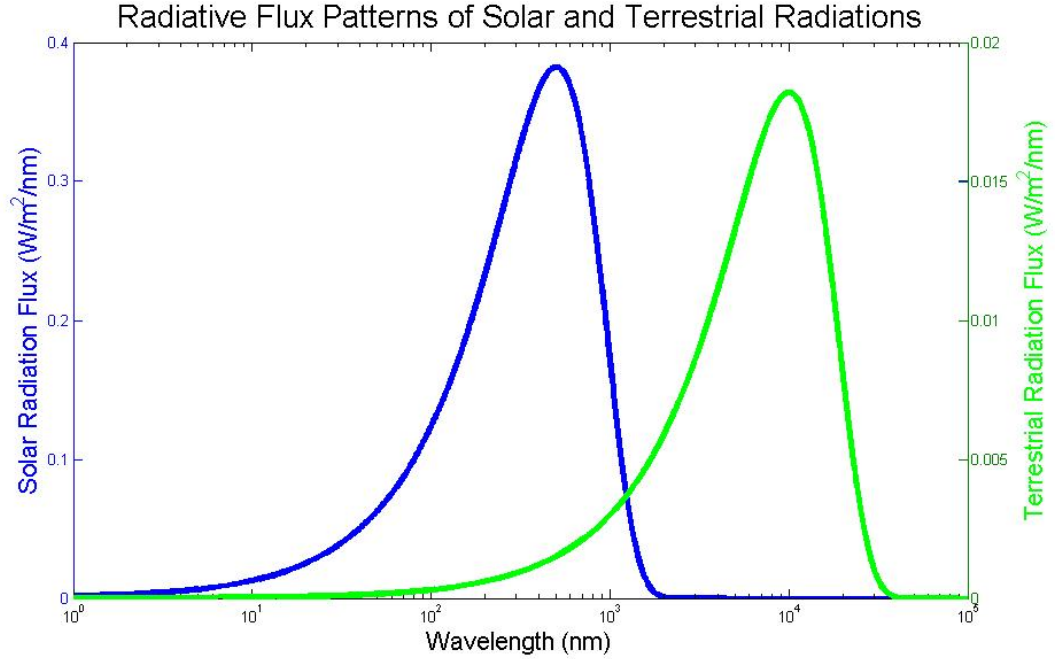


Figure 1.4: Solar and terrestrial radiation flux patterns.

The long-wave radiation shows a more uniform distribution with the latitude change than the shortwave radiation because the main source of long-wave radiation is heat, which is transferred to the higher latitudes by ocean and air flows. In addition, there is not a dramatic variation in the long-wave radiation flux between day and night time as in the shortwave solar radiation. Moreover, between $8\mu m$ to $14\mu m$, where the long-wave radiation peaks, the absorption in the atmosphere is very low. These advantages make terrestrial radiation an attractive constant energy source that does not show much time and latitude dependence. The only possible tool proposed so far to harvest this LW-IR energy is the ACMIM tunnel diodes due to their simple and cheap fabrication technique, which enables large area implementation. These motivates out interest in LWIR energy harvesting.

1.2 ACMIM Tunnel Diode Design Specifications

The antenna part of the ACMIM tunnel diodes convert IR radiation into detectable AC signal and channel it onto the built-in MIM junction. There are two important aspects of the antenna design: geometry and material. The target band of frequency lies in the Long Wave Infrared (LWIR), particularly around 30 THz. According to half-wave dipole antenna theory, at this frequency, half-length antenna resonance should occur at $5\mu m$, which is within the resolution capability of today's lithography technologies. However, more than a dipole antenna resonance is necessary to harness the IR radiation of the natural sources effectively. The need of a broadband antenna is obvious as the objects at a certain temperature emit IR with continuous spectrum corresponding to the blackbody radiation. Moreover, an antenna pattern that can accommodate wide polarization angle span of the incident wave is necessary to increase the total coupled power.

The metal antenna parts, separated from each other by an insulator film, form the MIM tunnel diode. Free electrons potential energy rises relative to the opposite electrode as a result of the AC signal across the MIM junction. The energized electrons start tunneling through the insulator film. Any imbalance between the positive and negative tunneling cycles of the AC signal results in a net DC current, namely rectification occurs. Probability of electron transport through the barrier is dependent on both the potential barrier height (difference between the metal Fermi level and the insulator conduction band edge) and the barrier width. As a result, both the material type and the thickness of the insulator effects the rectification

efficiency. In fact, tunneling current increases exponentially as the barrier width and the height decreases.

The coupled AC signal can be rectified and detected only if the diode response time is faster than one wave cycle. The tunneling mechanism itself does not bring a restriction to the IR detection because it is reported that the electron transition time through a $2nm$ insulator is less than $10^{-15}s$ [35, 23]. Therefore, fast electron tunneling can sustain IR frequencies. On the other hand, the physical formation of the tunnel junction brings an RC time constant that determines the cut-off frequency limit. It is not possible to modulate the RC time constant solely by decreasing the junction. Since the junction resistance and capacitance are coupled to each other, decreasing the junction area leads to a low parasitic capacitance but increases the junction resistance. A low junction resistance is not only necessary to minimize the RC time constant, but also important to match the diode impedance to the antenna radiation impedance for maximum power transfer.

For rectification, asymmetry is required across the operation point of the MIM I-V curve. While biasing the device can provide the asymmetry, for energy harvesting purposes zero bias operation is required. Work function difference between the materials can initiate a built-in potential off-set leading to asymmetry at zero bias when different metals are used as MIM electrodes. However, different metals create high potential barriers and increase junction resistance [20]. It is necessary to establish a low electron injection barrier on both sides of the junction to keep the resistance low. Therefore, material asymmetry is not the optimum method to create asymmetry at the MIM junction.

Design of the base substrate on which the ACMIM diodes are fabricated is also fundamental. A silicon wafer topped with SiO_2 film is commonly used. An insulating substrate is necessary both to eliminate substrate leakage current and minimize capacitive coupling between the antenna and the silicon. However, electron beam lithography, used to pattern the ACMIM diodes, is not straightforward on insulating surfaces because of the resolution-degrading charging problem.

In addition, array construction of ACMIM diodes is required for both the IR detection and harvesting applications. Therefore minimum performance variation among the array of devices and stability are needed. Moreover, fabrication methods should be proper for mass fabrication and the material selection should allow for low-cost large-area applications.

Next, we summarize our design approach to tackle the aforementioned ACMIM diode specifications. Our motivation is to surmount the problems of parasitic resistance and capacitance, asymmetric I-V response, tunneling efficiency bandwidth through the following:

- Bow-tie antennas that offer broadband frequency and large polarization span coupling are adapted to serve as the antenna part of ACMIM diodes. Nickel, whose plasma frequency is much above the LWIR, is used in our ACMIM diode fabrication.
- To improve tunneling efficiency, the native oxide of the nickel is used as a tunnel barrier. This not only allows for relative control over the film thickness, but also improves conduction since the barrier height between Ni/NiOx is

known to be small (0.2 eV) [25].

- A geometric asymmetry is established between the MIM electrodes by creating a sharp tip on one side and a rectangular patch on the other. The sharp tip also enhances the field at the junction lowering the forward resistance, and the capacitance. This geometry decouples the junction resistance from the capacitance.
- A thick ($1.5\mu\text{m}$) SiO_2 film is used on silicon wafer for isolation. The EBL charging problem is resolved by coating a thin conductive film on the e-beam resist.
- Fabrication methods are adopted to enable low cost mass production. Device stability and the parameter variation are investigated in detail.

1.3 Thesis Contribution

This thesis discloses, for the first time:

- A geometrically asymmetric bow-tie antenna coupled Ni/NiOx/Ni MIM junction, designed for $10\mu\text{m}$ wavelength IR detection, allowing for the creation of a diode-like device with rectification capability.
- A finite element method based multi-physics simulation results, used to optimize the antenna and the MIM junction geometry.
- A decoupling of the MIM junction resistance from the parasitic capacitance by designing one of the electrodes as a sharp tip. This creates more current

by local field enhancement and actually lowers parasitic capacitance as shown by simulation. This, in turn, allows RC time constant to be controlled for Terahertz detection.

- A processing method developed for the fabrication of ACMIM diodes that allows for high yield, low cost mass production; and high precision junction area control.
- An oxidation method to create a thin and robust oxide layer for efficient and stable ACMIM diodes.
- A chip packaging method developed to prepare the ACMIM diodes for testing.
- The feasibility of increasing sensor output power by summing individual elements connected in parallel.
- An image of an IR laser beam is generated by scanning the beam over the device. This is the first image generated by an IR wave detector in history.

1.4 Thesis Organization

The rest of the thesis is organized as follows: In Chapter two, physical phenomena behind the ACMIM diode operation are considered and the total IR detection efficiency expression is derived. In chapter three, ACMIM diode radiation coupling performance is investigated through some simulation results computed by a commercial software. Material and fabrication details are described in Chapter four,

while Chapter five gives the experimental results. And finally, in Chapter six, the thesis contribution is summarized and future project directions are discussed.

Chapter 2

Background

This chapter reviews both the experimental work related to the ACMIM diodes presented in the literature to date and the computational approaches used to elucidate the physical phenomena behind the conduction mechanisms occurring in these devices. Based on their nonlinear I-V relation, the rectification capability of the junction is evaluated and small-signal parameters are derived in order to model the tunneling diode. Lastly, the total efficiency expression of the ACMIM diodes is formulated.

2.1 ACMIM Diodes in the Literature

2.1.0.1 Point Contact MIM Diodes

The first generation MIM tunnel junctions were first reported as point contact-type (also known as cat-whisker) diodes in early 1960's [12]. The structure of this device was relatively simple: a tungsten wire acting as an antenna and a MIM diode that forms at the sharp tip of the wire leaning against a polished metal surface. The oxidized outer surface of the tungsten whisker prohibits the formation of ohmic contact between the whisker and the metal plate and electron transition occurs only via tunneling. The structure is shown in Figure 2.1. The nonlinear behavior of the tunneling mechanism enables the direct wave detection, harmonic generation and

frequency mixing. Point contact tunnel diode operation was shown for millimeter and sub-millimeter ($227\mu m - 0.6328\mu m$) waves [26, 14, 18, 56, 22, 54, 48, 15, 56].

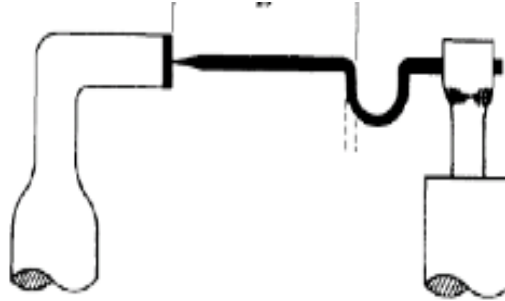


Figure 2.1: First generation point contact MIM diodes [12]

In this configuration the MIM diode contact area is controlled by the physical sharpness of the wire and the pressure applied to push the wire onto the metal plate. Hence, the contact area tends to be very small. This is the main advantage of this structure since it minimizes the parasitic capacitance, enabling very fast operation. The direct wave detection achieved at IR and optical frequencies using point-contact diodes was only possible because of the small contact area of point contacts and the single side field enhancing sharp tip. However, these devices lacked stability and reproducibility because their performance depended on a mechanical system. Moreover, their fabrication was not CMOS compatible, so their application as IR detector or imager is not feasible.

Point contact MIM diodes were important because they opened a new path for direct wave detection using an antenna and a tunneling diode system at much higher frequencies than the communication technology. In addition, the theory on the

quantum mechanical tunneling phenomenon, which had been previously developed, was experimentally verified.

Point contact MIM diodes have not only been an important leading first prototype for our work, but also the inherent asymmetry between the electrodes is the first exploitation of geometric asymmetry and the field enhancing sharp tip electrode.

2.1.0.2 Thin Film MIM Diodes

Second generation thin-film MIM diodes came into play in the 1970's to eliminate the mechanical instability problem of point contact diodes [53, 57, 13, 22, 24]. This approach allowed the implementation of antenna and tunnel junction by integrating them on a substrate using lithography. Thin film structures enabled the CMOS compatible fabrication and developments in this field closely followed the advancements in lithography.

Initially overlap structures are formed by optical lithography using various metal combinations. However, due to resolution limitations the junction area could not go beyond $10^{-12}m^2$. In 1978, the "Edge-MOM" technique was introduced by Heiblum et al. [24]. This technique managed to decrease the junction area by sandwiching the first metal structure between two insulator layers, oxidizing the edge of the first metal layer and limiting the contact with the second metal only to this side opening. Two orders of magnitude improvement in contact area was achieved with this method. The "edge-MOM" structure can be seen in Figure 2.2.

Another turning point in the fabrication of ACMIM diodes happened when

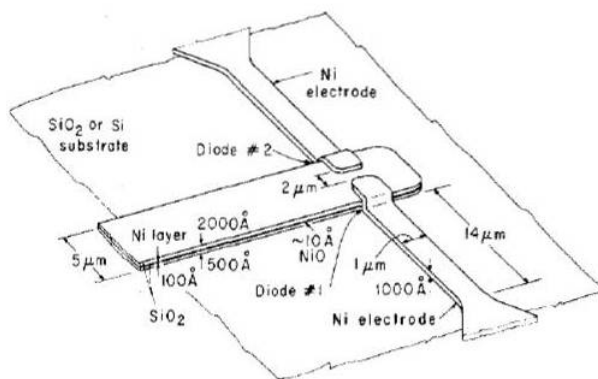


Figure 2.2: Thin film edge-MOM [24]

high resolution electron-beam lithography (EBL) was used for patterning [17]. For integrated devices, the challenge was to minimize the tunnel junction area for high speed operation, as well as the dimension control of the antenna to provide optimization at IR frequencies. EBL facilitated μ -scale antenna integration and allowed for smaller junction areas. EBL is still the major lithography technique that is being used in the active research of integrated MIM structures, however additional methods are employed to enhance its fidelity and resolution. Two types of ACMIMs produced with EBL patterning technique are presented in Figure 2.3.

2.1.0.3 Recent Technologies in Thin Film MIM Diodes

As a result of the developments in EBL and resist technology, μm -dimension antenna patterning became straightforward in the 2000s. Currently, the main fabrication challenge is to form a fast (small RC constant) but efficient tunnel junction. Making small junctions reduces capacitance. But area reduction of the diode increases forward resistance, which degrades the power coupling into the junction.

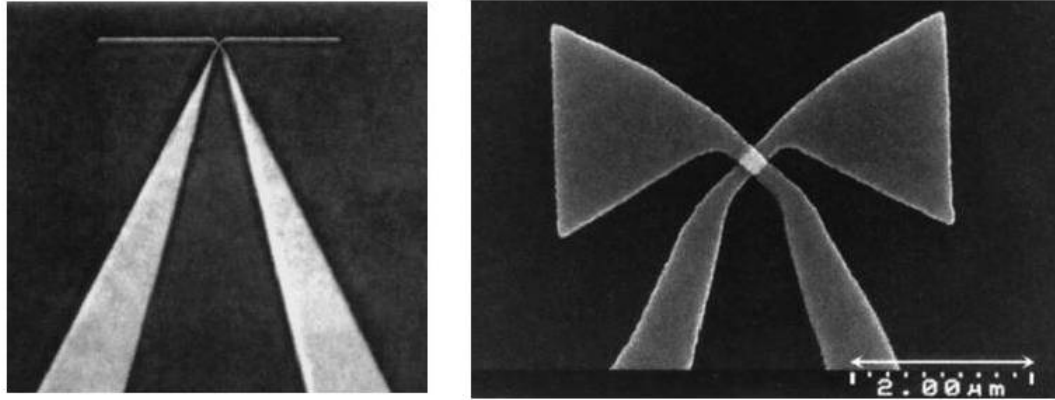


Figure 2.3: Thin film ACMIMs left: dipole antenna, right: bowtie antenna [17]

Therefore, the recent research in this field has changed its direction to discover the optimum insulator of the MIM along with the MIM area minimization that enables tunneling and provides long term device stability.

Two recent methods to decrease the junction area were proposed by Bean et al. [5] and Hobbs et al. [25]. Bean et al. developed a single step EBL technique where a double layer resist is used in conjunction with a high voltage, high resolution e-beam (see figure 2.4). The e-beam lithography was followed by precise shadowed metal deposition and the MIM area is set by the degree of metal deposition angle. This method is important because it allows for the deposition of both electrodes without breaking the vacuum. Hence, the oxide is grown in vacuum where gas and temperature are critically controlled. While dispensing successful results on individual devices, this method cannot be applied to large area fabrication as high-resolution EBL is the key to its success. Moreover, Pt - a rare and expensive metal - increases the total cost of this method.

Hobbs. et al. also used single step EBL followed by angled deposition (2.5).

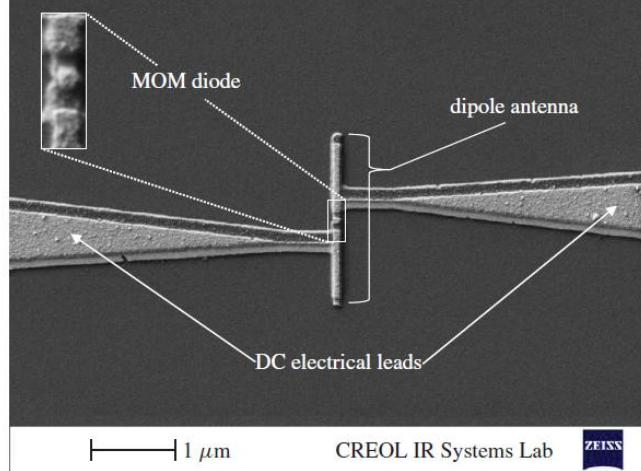


Figure 2.4: Micro-graph of an Al/AlO_x/Pt ACMIM fabricated by shadow evaporation method [5].

In this work, to improve antenna coupling, radiation is sent through a waveguide and $1.6\mu\text{m}$ wavelength detection is shown. Also in this method, successful results are demonstrated on individual devices, but large area fabrication is not applicable due to the complex methods used in the processing.

Another recent approach for the ACMIM fabrication has been introduced by Gupta et al [21]. To eliminate the lithographic resolution dependence of the ACMIM junction area and the gap width, a selective atomic layer deposition (ALD) method is used. After non-critically patterning electrodes, copper is grown in ALD chamber in monolayer cycles and, in between cycles, the junction conduction is electrically checked by applying a bias. The growth is stopped once the desired tunnel junction resistance is achieved. The schematic of this ACMIM is shown in Figure 2.6. Although it allows for precise MIM junction control, this method is far from satisfying the goal of large area fabrication for detection and harvesting purposes.

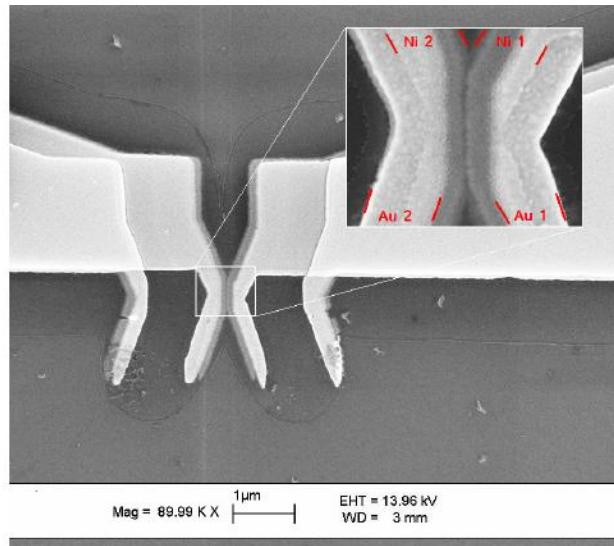


Figure 2.5: Micro-graph of a waveguide integrated Ni/NiO_x/Ni ACMIM fabricated by shadow evaporation method [25].

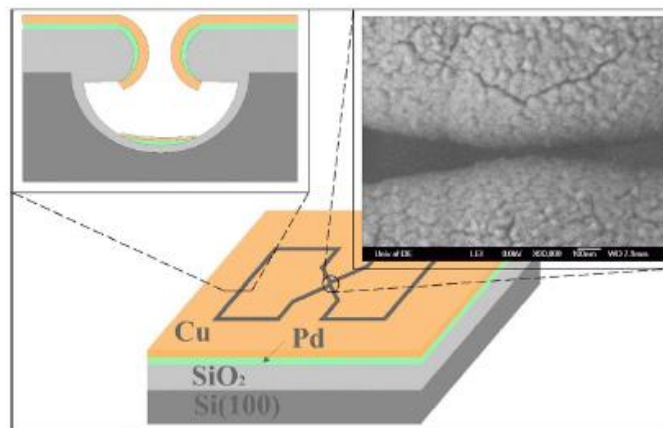


Figure 2.6: Schematic view of the Cu/Air/Cu ACMIM fabricated by ALD [21].

Choi et al. created the base technology of our approach in the fabrication of ACMIM diodes[9]. In his work, Ni/NiOx/Ni ACMIM diodes are fabricated in two-step EBL. Figure 2.7 shows SEM micro-graphs of the ACMIM diodes in two different geometries. First, the junction area is large ($0.01\mu m^2$) compared to the other recent ACMIMs. Second, total antenna length is $2.5\mu m$, which is half of the dipole resonance antenna length. And lastly, despite the large area junctions, resistances reported in this work are much higher ($\sim M\Omega$) than the ones reported in [5].

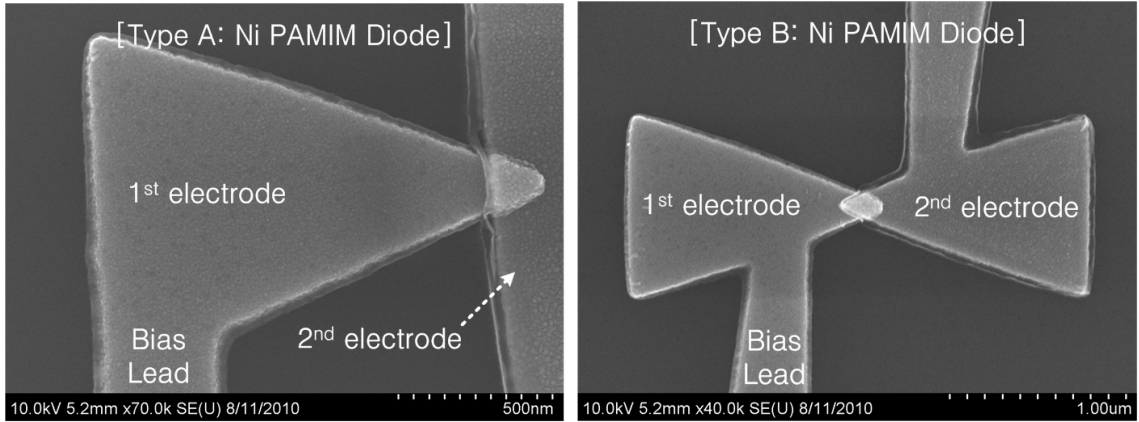


Figure 2.7: Ni/NiOx/Ni ACMIM diodes in two different geometries [9].

Figure 2.8 shows a typical SEM micrograph of our Ni/NiOx/Ni ACMIM diodes. In our process, resolution of the EBL is improved by incorporating proximity effect correction methods and the alignment of the two electrodes is optimized to control the MIM junction area. In addition, an extensive metal oxidation study is performed to form the thinnest and the most durable oxide. The geometric parameter effects of the rectenna are both analyzed through simulation and experimental results. Every aspect of the design is statistically analyzed with experimentally ob-

tained data. Lastly, a packaging method is developed and IR tests are performed successfully.

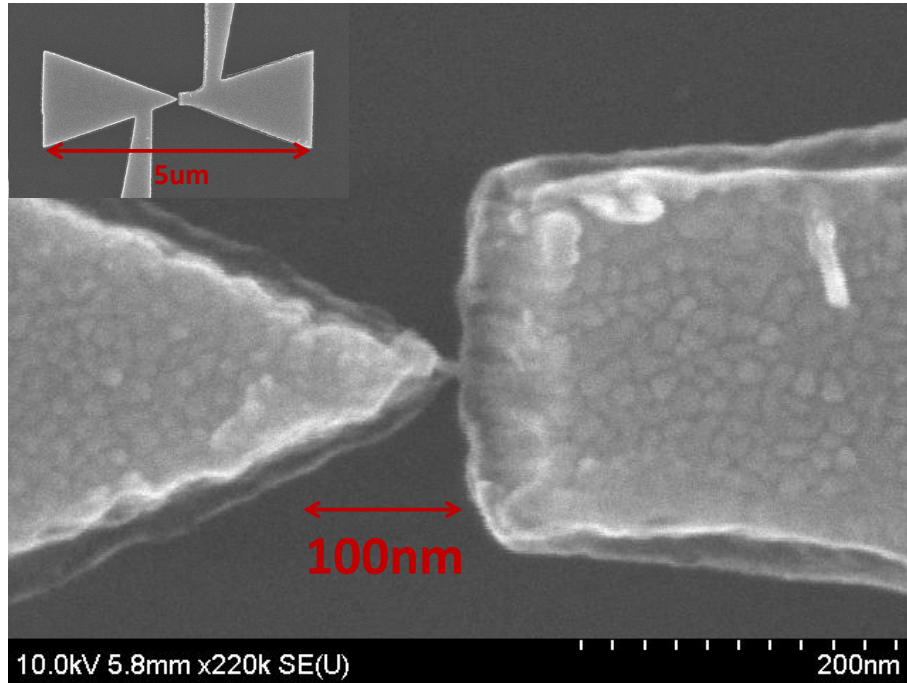


Figure 2.8: SEM micrograph of a Ni/NiO_x/Ni ACMIM fabricated during this thesis work.

2.2 Conduction Mechanisms in Thin Films

Electron transition through a thin insulating film sandwiched between two conductive materials occur as a result of a number of physical processes. A one dimensional representation of an MIM structure is shown in Figure 2.9. In the scheme d and ϕ represent the insulating film thickness and the barrier height (difference between the work function of metal and the affinity of insulator), respectively. To some extent, the conduction dynamics in MIM structures corresponds to the “field-

induced electron emission theory”, which was intensely studied in 1920s by Schottky, Millikan, Oppenheimer, Fowler and Nordheim [16, 33, 49, 37]. According to their work, electron emission or transport through a potential barrier can be analyzed under two main categories: cold-field electron emission (field-assisted tunneling) and Schottky electron emission (thermal-assisted tunneling). In the former case, the emitter is in thermodynamic equilibrium and electron tunneling through the potential barrier takes place near the Fermi level as a result of an external field. This conduction mechanism was formulated by Fowler and Nordheim who considered the trapezoidal barrier tip curving due to the image charge effect. The cold electron emission process is shown in Figure 2.10 a. In the thermionic electron emission, electrons either gain energy due to the phonon interaction created by the excessive heat in the material and they are thermally excited to higher energy states where tunneling is more likely. Electrons may also be transported to the emitting region where they have enough kinetic energy to surmount the barrier without tunneling (see Figure 2.10 b). In addition, electron transport as a result of photo-excitation is possible. This phenomenon is called “photon assisted tunneling” and it has been studied since the discovery of the photoelectric effect in 1887 by Hertz (see Figure 2.10 c).

Simmons, who adapted the field-induced electron emission theory for vacuum systems to dielectric films sandwiched between metals and semiconductors (such as MIM junctions), made two very important observations in [50]: 1) reproducibility of MIM junctions is a challenge due to the imperfections in the compound insulator thin films and 2) conduction in thin dielectric films cannot adequately be described

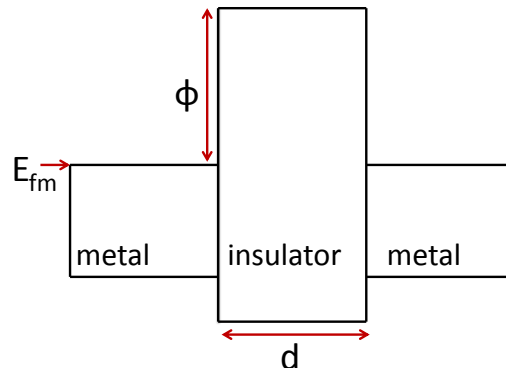


Figure 2.9: Energy band diagram of Metal-Insulator-Metal tunnel diodes

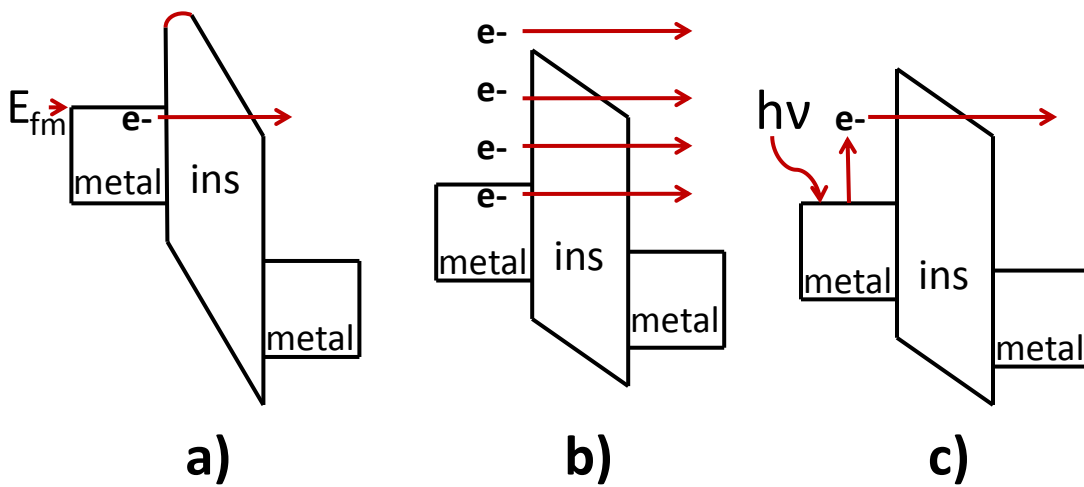


Figure 2.10: Conduction mechanisms in MIM tunnel junctions. a) Field assisted tunneling b) Thermal assisted tunneling c) Photon assisted tunneling

by a single conduction process.

Stoichiometrically and geometrically, perfect crystal films of metal and compound insulators are not possible to prepare using conventional metal film deposition methods, such as evaporation. Defect and impurity-oriented extrinsic conductivity should always be considered in MIM junctions. First, the evaporated metal thin films in many cases are in amorphous form. For example, the grain size is on the order of 10nm in the nickel film used in this work. As a result, the insulator film deposited or grown on the metal (to form the native oxide of the metal) has perfect crystal behavior only locally. In the long term, these crystallites host grain boundary defects that play an important role in the conduction. Second, it is very common to come across contamination problems in both the metal evaporation and oxidation processes. The contamination in the metal evaporation could stem from the impurities in the crucible or the wall degassing in the multi metal vacuum chambers operated by multi-users. On the other hand, the native oxide of the evaporated metal film is used as the insulator in our MIM junction process. An effective oxidation method we use is plasma oxidation of the metal. The metal film is exposed to all the contaminants in the plasma chamber where the RF power is utilized together with the high oxygen gas pressure.

Throughout the analysis on conduction mechanisms in MIM junctions, an energy band diagram that represents perfect crystal structures will be used. It should be noted that a rigorous border between the forbidden gap and the conduction/valance band is only valid in local crystal structures. The overall current transport cannot be solely evaluated on the theory developed using these energy band

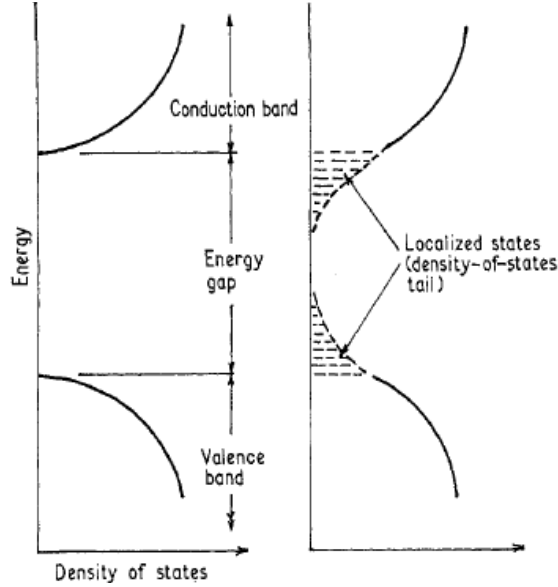


Figure 2.11: Energy band diagram of a perfect crystal (left) and amorphous (right) film[50].

diagrams. The discrepancies between the experiment and the theory stem mainly from the non-crystalline metal and oxide films. Figure 2.11, provided by Simmons in [50], illustrates the band diagram difference between a crystal and amorphous solid. This scheme shows the existence of transition states at the conduction/valence band and the forbidden gap interface. The localized states in the forbidden region are mostly the result of diffusion of the bands and the traps.

Thermal- and field-assisted tunneling are the two major conduction mechanisms in MIMs. The incident IR, absorbed by the substrate, may lead to a temperature increase and excite electrons by $k_B\Delta T$ where k_B is the Boltzman constant. Thermal excitation is usually a slow process. Depending on the thermal mass of the sensing material, it may not be possible for the thermally driven process to create terahertz response [19]. But thermal process can contribute to the conduction

background. Field-assisted tunneling should be the dominant mechanism in the antenna coupled MIM diodes. In other words, the most efficient IR detection can be launched by transferring the radiation energy directly into electron motion on the antenna surface instead of converting it into heat through absorption and relying on this thermal energy to assist tunneling.

The design of the barrier (d and ϕ), the potential applied across the junction and the temperature of the material determine the observed current. For terahertz wave rectification, field-assisted tunneling efficiency can be increased by decreasing the barrier thickness because the tunneling efficiency increases as the barrier thickness decreases. As a result, for barrier thicknesses in the order of nanometers ($\leq 5nm$) the dominant conduction mechanism can be stated as quantum mechanical tunneling. The thermal emission can be considered as the secondary conduction mechanism. If the incident radiation interacts with the antenna more than the substrate, radiation absorption and heat accumulation in the substrate can be limited. This can be achieved by increasing the density of devices on the focal plane. Lastly, conduction in the bulk insulator can be considered in the existence of donor levels in the bulk insulator. These act as “stepping stones” to assist electron transport and the Poole-Frenkel effect can be utilized to contribute to the total conduction. These conduction mechanisms: electrode limited (tunneling and thermal emission) and the bulk limited (Poole-Frenkel) will be detailed in Appendix A.

2.3 Rectification Analysis

Conventionally, either Schottky diodes or MIM tunnel diodes are used as rectification elements in rectennas. Schottky diodes function efficiently up to 5THz and MIM tunnel diode operation has been shown up to 150 THz [34]. There are three different physical phenomena that limits the operation frequency of MIM tunnel diodes: 1) The response time of the oscillating electrons on the metal antenna 2) The electron transition time through the barrier 3) The electro-dynamical response of the tunnel junction (RC time constant) [34]. First, metals whose plasma frequency are in the UV range, such as nickel, are used for the antenna material. Therefore, the conduction electrons in metals will respond well in both the IR and visible frequencies. Second, the limitation due to the electron transit time can be approximated by assuming that electrons will move with their corresponding Fermi velocity through the barrier. An electron at the Fermi energy of nickel ($5eV$) can transmit a barrier of width $d = 1nm$ with Fermi velocity $V_f = 1.3 \times 10^6 m/s$ in $t_{tun} = 0.77 \times 10^{-15} s$. This yields a cut-off frequency $f_{cut-off} = \frac{1}{2t_{tun}} = 7 \times 10^{14} Hz$ (calculated using Equation 2.1) imposed by the barrier transit time of electrons. Thus, detection up to visible frequencies ($4.3 \times 10^{14} Hz - 7.5 \times 10^{14} Hz$) is possible with MIM tunnel junctions.

$$V_f = \sqrt{\frac{2E_f}{m_e}} = d * \frac{1}{2t_{tun}} \quad (2.1)$$

What limits the operation speed of the MIM junctions is the electro-dynamical response time (RC time constant). In conventional planar diodes the junction resistance (R) and capacitance (C) are coupled to each other as defined in Equation

2.2:

$$C = \epsilon \frac{A}{d} \quad \text{and} \quad R = \frac{dV}{dI} = \frac{dV}{AdJ} \quad (2.2)$$

The junction capacitance is directly proportional to the junction area (A), whereas the junction resistance is inversely proportional to it. Our solution to the RC time constant limitation is to decouple the junction resistance from the junction parasitic capacitance by adapting the point contact MIM junctions to two dimensions. In planar ACMIM diodes, current is not directly proportional to the junction area but it is dominantly determined by the sharpness of the cathode tip. The sharper tip allows for charge transport in small areas and the forward resistance of the diode decreases without increasing junction area (so the capacitance). Thus the junction resistance and capacitance can be decoupled [55].

Rectification requires an imbalance between the forward and reverse currents formed during the positive and negative cycles of the AC potential at the junction. This imbalance can be implemented using various methods that can bring asymmetry to the DC electrical behavior of the diode at the operation point. Material asymmetry, thermal asymmetry, and geometric asymmetry can introduce asymmetry at the zero bias enabling rectification without an applied bias. By applying a bias, the operation point can be moved to the diode turn-on point where efficient rectification can be achieved for detector applications. However, for energy harvesting applications, it is necessary to operate the diode at zero bias. Our goal is to use geometric asymmetry, where junction electrons encounter different potential barrier during forward and reverse bias conditions due to the uneven field enhancement

across the MIM junction. This “geometric” approach to asymmetry was theoretically proposed by [36, 31] but our research shows it experimentally [7].

More recently, a complete theoretical analysis of the geometrically asymmetric Metal-Vacuum-Metal (MVM) junctions was done by Mayer et al. [32]. After defining the cathode as a protrusion and the anode as a flat, three dimensional asymmetric geometry of the junction was computed. First the potential-energy distribution was mapped and, using transfer matrix methodology, the forward and reverse currents were calculated in the existence of geometric, material and temperature differences between the junction electrodes. This analysis revealed that rectification can be realized over MVM junctions with either geometric, material or temperature asymmetries.

It is very common to explain the rectification with a classical approach based on Taylor-expansion. However, this classical approach is only valid if the period of the coupled AC signal is much larger than the electron’s transit time through the tunnel barrier. Since this transit time is in the order of femtoseconds in the MIM junctions, classical analysis can be used at the IR frequencies [31].

The extraction of the rectification parameters starts by taking the nonlinear DC current-voltage relation of the quantum mechanically derived tunneling current. The total current when the voltage $V(t) = V_{DC} + V_{AC} \cos(\omega t)$ is applied can be found using Taylor series expansion as:

$$I(t) = \sum_{n=0}^{\infty} \frac{1}{n!} \frac{d^n I(V_{DC})}{dV_{DC}^n} [V(t) - V_{DC}]^n \quad (2.3)$$

$$= I_{DC} + \frac{dI_{DC}}{dV_{DC}} V_{AC} \cos(\omega t) + \frac{1}{2} \frac{d^2 I_{DC}}{dV_{DC}^2} V_{AC}^2 \cos^2(\omega t) + \dots \quad (2.4)$$

This expansion can be rewritten in the following form:

$$I(t) = \sum_{n=0}^{\infty} I_n \text{Cos}(n\omega t) \quad (2.5)$$

where traditional trigonometric relations are used. The dominant non-oscillatory terms define the DC current and it is approximated ignoring the higher order terms as:

$$\langle I(t) \rangle = I_{DC} + \frac{V_{AC}^2}{4} \frac{d^2 I_{DC}}{dV_{DC}^2} \quad (2.6)$$

$$= I_{DC} + I_{rect} \quad (2.7)$$

$$I_{rect} = \frac{V_{AC}^2}{4} \frac{d^2 I_{DC}}{dV_{DC}^2} \quad (2.8)$$

In addition, the total energy transferred onto the electrons that cross the barrier can be calculated as:

$$\langle P \rangle = \frac{\omega}{2\pi} \int_0^{\frac{2\pi}{\omega}} V(t)I(t)dt \quad (2.9)$$

$$= V_{DC}I_{DC} + \frac{V_{AC}^2}{2} \frac{dI_{DC}}{dV_{DC}} \quad (2.10)$$

Moreover, the equivalent rectified DC voltage component can be extracted as:

$$V_{rect} = \frac{I_{rect}}{dI_{DC}/dV_{DC}} \quad (2.11)$$

$$= \frac{V_{AC}^2}{4} \frac{d^2 I_{DC}/dV_{DC}^2}{dI_{DC}/dV_{DC}} \quad (2.12)$$

Once the incident power on the tunnel junction and the rectified current are derived, we define the quantum efficiency of the rectification process as the total rectified current per unit oscillating energy transferred to the electrons that cross the barrier at the quantum limit $e/\hbar\omega$ and can be derived as below:

$$\eta_{quant} = \frac{1}{2} \frac{\hbar\omega}{e} \frac{d^2 I_{DC}/dV_{DC}^2}{dI_{DC}/dV_{DC}} = \frac{1}{2} \frac{\hbar\omega}{e} * S \quad (2.13)$$

To summarize, three important parameters that directly determine the rectification efficiency will be used in order to quantify the MIM tunnel diodes in this work: 1) Junction resistance: $R = 1/(dI_{DC}/dV_{DC})$ 2) Nonlinearity of the device: $N = d^2I_{DC}/dV_{DC}^2$ 3) Sensitivity or responsivity (directly proportional to the quantum efficiency): $S = \frac{d^2I_{DC}/dV_{DC}^2}{dI_{DC}/dV_{DC}}$.

2.4 Rectenna Design

The geometry of the ACMIM tunnel diodes are structured in a way that the MIM junction forms at the center fed point of a bow-tie antenna. According to antenna operation principles, when a radiation is incident on the antenna, it induces surface charge fluctuations that results in a surface current distribution. The bow-tie antenna dimensions are arranged based on the half-wave dipole antenna. That is, the total antenna length is set as half the IR radiation wavelength ($L_{total} = \lambda/2$) because this particular geometry maximizes the coupled antenna current and the voltage differential at the center (see Figure 2.12). Therefore, the antenna focuses the coupled radiation power at the center knot point where the MIM junction is located. The enhanced E-field ($E = dV/dx$) across the junction modulates the potential barrier, allowing for the electron transition through tunneling. Since tunneling has a nonlinear relation between the voltage and the current, rectification of the AC charge oscillations takes place across the junction.

The bow-tie antenna pattern provides various advantages in terms of maximum transfer of the radiation power into the MIM junction. Overall, the design evokes

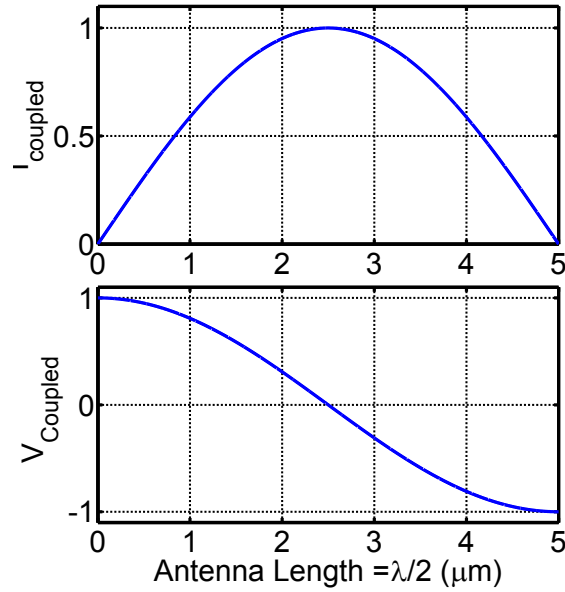


Figure 2.12: Normalized voltage and current distribution on a half-wave dipole antenna.

broadband antenna, which couples a range of incident frequencies. But antenna bandwidth can be further controlled by varying the flare angle. This is a desirable property for both the IR detection and harvesting applications because IR sources in nature emit black body radiation, which has a continuous spectrum (also called Plank's spectrum). Moreover, unlike dipole antennas, bow-tie antenna polarization dependence is not as sharp. As the flare angle increases, a wider polarization angle range can be coupled. This is a crucial property as the IR detector in real world will interact with non-collimated light incident in every direction. And lastly, the bow-tie shape having a sharp tip of nano-size radius-of-curvature can focus the radiation power in a nm^2 -sized area. This is an indispensable requirement for a rectenna that must operate at ultra high (Terahertz) frequencies.

The magnitude of the current density on the antenna surface is computed for our novel bow-tie antenna geometry and the results are exhibited in Figure 2.13, where both the whole antenna surface (left) and focused junction (right) are shown to prove the power concentration property. On these images it can be observed that the surface currents concentrate towards the tip in the existence of the perpendicular, 30 THz IR radiation. As expected the maximum current density occurs at the tip with an amplitude of $1.4 \times 10^7 A$ for an incident IR power density of $2.7 \times 10^{-3} W/m^2$.

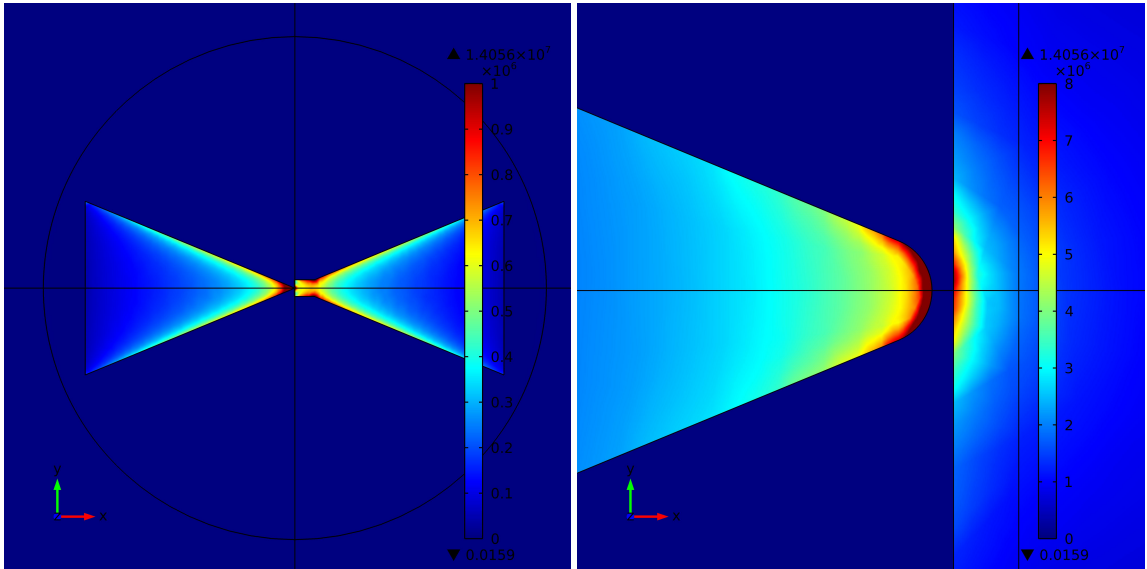


Figure 2.13: Surface current density magnitude on the whole antenna (left), focused at the junction (right). Color scales from left: Red ($1 \times 10^6 A$) to Blue (0A) and right: Red ($8 \times 10^6 A$) to Blue (0A).

In addition to the geometry, the antenna material also plays an important role in effective wave coupling. In the ACMIM diode fabrication, nickel is widely used. The optical parameters of nickel at 30 THz are $n = 6.8$ and $k = 37$ [40] and it leads to conductivity of $\sigma = 2nk\epsilon_0\omega = 2.5 \times 10^5 (\Omega m)^{-1}$, which shows that

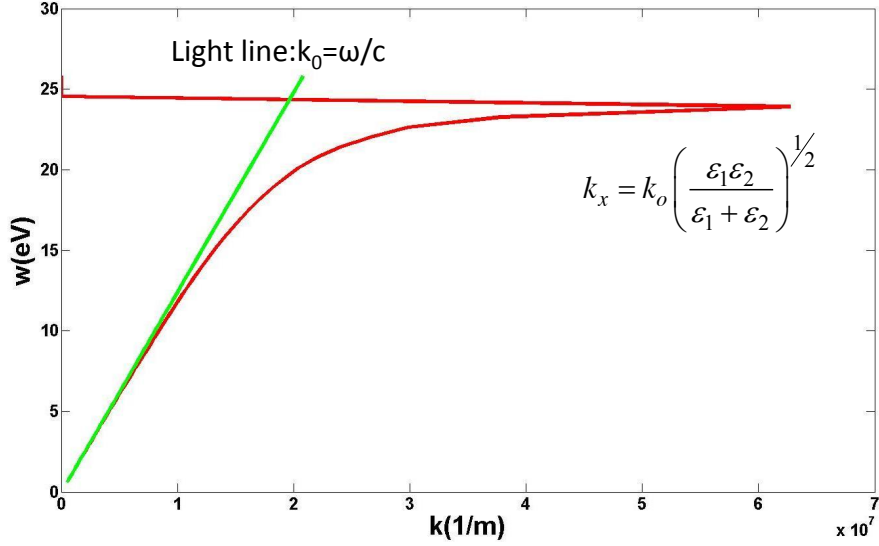


Figure 2.14: Evanescent wave dispersion curve propagating at the air-Ni interface and light line.

nickel at IR frequencies is almost lossless and it is a perfect conductor (IR is far below nickel’s plasmon frequency.). A perfectly conductive antenna minimizes the resistive losses and creates pure evanescent waves on the antenna surface. In Figure 2.14 the dispersion curve of the evanescent wave launched between air and nickel media is compared to the dispersion curve of a wave traveling in the air. The 30 THz frequency corresponds to 0.12eV and, in this low energy IR range, the evanescent wave dispersion coincides with the light line. Hence, this also demonstrates that the phase velocity of the evanescent wave coupled on the antenna surface has the same phase velocity as the wave propagating in the air, which is expected for the broadband antenna coupling.

Our novel geometric design of ACMIM, shown in Figure 2.13, is a 2-D realization of the point contact diodes. Although a symmetrical bow-tie antenna is used for

field coupling, at the MIM junction the symmetric geometry is distorted by keeping one side of the antenna as a sharp tip and the other side as a flat patch. Electron emission from the sharp tip is easier than the electron extraction from the flat edge under the same applied field. Thus, the asymmetry in the electrode pattern results in an asymmetry in the tunneling current leading to a rectifying behavior. In Figure 2.15, the geometric asymmetry induced rectification is illustrated schematically on the potential energy band diagrams. When the electrode with the sharp tip is negatively biased, potential decays rapidly close to the tip and the effective barrier through which electrons tunnel is narrow. This forward bias configuration allows for an effective electron emission as shown in Figure 2.15 b). Opposite bias leads to a reverse effect and creates wide barrier to tunnel for the electrons of the rectangle patch as shown in Figure 2.15 c)[58].

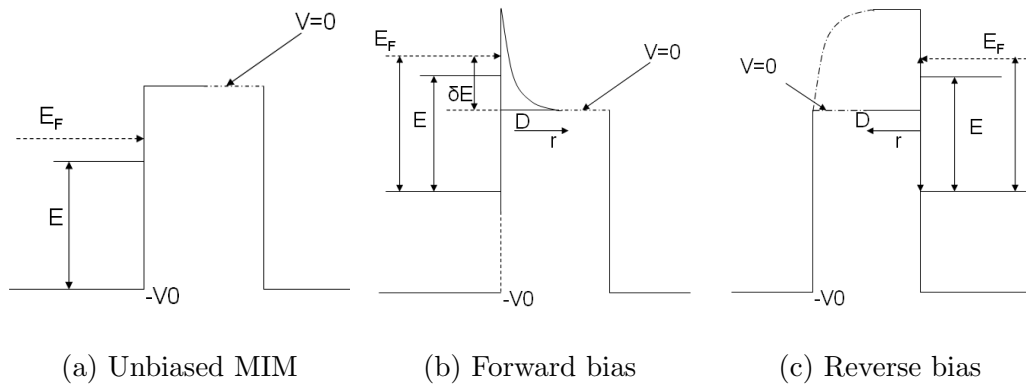


Figure 2.15: Asymmetric geometry induced rectification illustration on the potential energy band diagrams [58].

2.5 Total Efficiency Estimation

The total IR detection efficiency of the ACMIM tunnel diodes was studied by Kale et al. [28] and it is stated in terms of four different components given in Equation 2.14:

$$\eta = \eta_a \eta_s \eta_c \eta_q \quad (2.14)$$

Antenna efficiency, which corresponds to the total power coupled by the antenna per unit of intercepted power, is represented by η_a . An antenna designed for IR harvesting operates as a receiving antenna that interacts with the incident EM wave (Incident wave can be taken as a uniform plane wave assuming a far source.). The incident wave induces current on the metal antenna surface (assuming a perfectly conducting antenna, the tangential component of the electric field at the boundary disappears leaving surface currents on the metal) which constitutes the power coupled by the antenna. In the circuit representation of the rectenna, shown in Figure 2.16, the total coupled power by a receiving antenna can be taken in the Thevenin equivalent form as an AC voltage source and an antenna impedance ($R_A + jX_A$). The MIM tunnel diode is formulated with a voltage dependent resistor ($R_D(V)$) in parallel with a capacitor (C_D) and a resistor (r) in series for the conductive losses on the antenna arms. The total power provided by this voltage source is determined by the antenna efficiency η_a .

The next efficiency component considers the losses that occur while the currents at the antenna surface flow onto the antenna node where the tunnel junction is formed. It is represented by η_s . This parameter strictly depends on the material

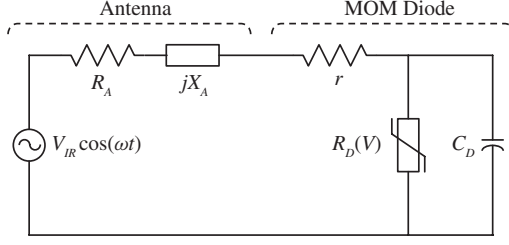


Figure 2.16: Circuit representation of the ACMIM tunnel diode.

conduction property at the operating frequency. In our case, nickel is used as the antenna material and it can be considered to be a perfect conductor at 30 THz frequency and the series resistor r in the circuit can be ignored. Therefore, η_s is taken as 1.

The impedance matching between the antenna radiation resistance and the diode resistance forms a very crucial component of the total efficiency, represented by η_c . The tunnel diode is characterized with a capacitance and a voltage dependent resistor in this circuit model. In order to achieve efficient coupling with the input power it is important to keep the diode resistance R_D value as close as possible to the antenna resistance R_A . Here the junction resistance value should be the value at the operating bias voltage, which is zero-bias $R_D(0)$ for IR harvesting applications and $R_D(V_{bias})$ for IR detecting case. $R_D(V_{bias})$ is always lower than $R_D(0)$ due to the nonlinear I-V characteristic of tunnel diodes. And lastly, η_q is the quantum efficiency derived in Section 2.3 as in Equation 2.16.

$$\eta_c = \frac{R_D}{R_D + R_A} \quad (2.15)$$

$$\eta_q = \frac{1}{2} \frac{\hbar\omega}{e} * S \quad (2.16)$$

The incident power intensity or Poynting vector (S) is the time averaged power per unit area of the incident radiation. The incident electric field E_{rms} can be related to the Poynting vector using the vacuum impedance $Z_0 = \sqrt{\mu_0/\epsilon_0} = 377\Omega$ as in Equation 2.17 below:

$$S = \frac{P_{inc}}{A} = \frac{E_{rms}^2}{Z_0} = \frac{E_p^2}{2 * Z_0} [W/m^2] \quad (2.17)$$

The amplitude of the coupled potential across the antenna arms V_A is related to the incident electric field (E_p) and the effective antenna length l_{eff} as in Equation 2.18. The effective antenna length (l_{eff}) is a function of the incident wave direction and the antenna length L_{ant} as formulated in Equation 2.19 [39]. When the beam is incident perpendicularly $\theta = 90^0$, l_{eff} can be approximated as the antenna physical length L_{ant} .

$$V_A = l_{eff} * E_p \quad (2.18)$$

$$l_{eff} = L_{ant} \sin(\theta) \quad (2.19)$$

Here an important parameter called antenna aperture efficiency or antenna fill factor comes into play. Antenna fill factor f can be defined as in Equation 2.20. It is a dimensionless parameter and is equivalent to antenna coupling efficiency η_a . Conceptually, it describes how well the antenna can couple the incident radiation.

$$f = \frac{A_{eff}}{A} = \frac{L_{ant}^2}{A} = \eta_a \quad (2.20)$$

Thus, the coupled voltage V_A can be expressed in terms of the incident power as:

$$V_A = \sqrt{\frac{P_{inc} * 2Z_0 * L_{ant}^2}{A}} = \sqrt{P_{inc} * 2Z_0 * f} \quad (2.21)$$

When the AC electric field excites surface electrons, electron motion on the antenna surface induces electric field and re-radiates a fraction of the coupled power. This loss in the re-radiated power is represented by a virtual resistance called “antenna radiation resistance R_A ” and it is determined by the geometry of the antenna. The antenna coupling efficiency can also be formulated by circuit representation where the total radiation power is shared between the vacuum impedance Z_0 and antenna radiation resistance R_A as in Equation 2.22. Rutledge et al. calculates the antenna resistance of a bow-tie antenna with a flare angle 45° as 175Ω [47]. The fill factor can be estimated as 0.32.

$$f = \frac{R_A}{R_A + Z_0} = \frac{175}{175 + 377} = 0.32 \quad (2.22)$$

Once the antenna potential is defined in terms of the incident radiation, the impedance matching efficiency η_c should be used to define the power that forms across the diode as in Equation 2.23.

$$P_D = \frac{V_A^2}{(R_A + R_D)^2} * R_D [W] \quad (2.23)$$

The first component of total efficiency is defined as power transfer efficiency (η_t). This term determines the fraction of the incident power that can reach the diode from the antenna section. It can be derived as in Equation 2.24 using Equations 2.23 and 2.21:

$$\eta_t = \eta_a * \eta_s * \eta_c = \frac{P_D}{P_{inc}} = \frac{2 * f * Z_0 * R_D}{(R_A + R_D)^2} \quad (2.24)$$

When $R_D \gg R_A$: $\eta_t \sim \frac{2*f*Z_0}{R_D}$. For example, $f = 0.32$, $Z_0 = 377\Omega$, $R_D = 10k\Omega$ yield $\eta_t = 0.024$, where transfer efficiency falls to 2.4%.

The total efficiency, which is the ratio of the detected DC power and the incident radiation power, can be defined as in Equation 2.25 below:

$$\eta = \eta_t * \eta_q = \frac{2 * f * Z_0 * R_D}{(R_A + R_D)^2} * \frac{1}{2} \frac{\hbar\omega}{e} * S \quad (2.25)$$

Taking $R_D = 10k\Omega$ (as is typical for MIM diodes) and $S = 6$ (typical diode sensitivity), also the antenna fill factor $f = 0.5$ (assuming that the coupling efficiency is improved), the total IR (30THz) detection efficiency can be estimated as $\sim 1\%$:

$$\eta = \frac{2 * 0.32 * 377}{10000} * \frac{1}{2} * 4.1 \times 10^{-15} * 3 \times 10^{13} * 6 = 0.009 \quad (2.26)$$

2.6 Summary

- Conduction mechanisms in MIM junctions are introduced. Field-assisted and thermal-assisted tunneling are concluded to be the possible conduction mechanisms.
- Expected divergence from the theoretical estimations is reasoned by the use of non-crystalline materials.
- The DC rectified signal expressions and the quantum efficiency are derived by a semi-classical approach based on the diode nonlinear current-voltage relation.
- Design of the antenna geometry and material is justified for the optimum 30 THz IR radiation coupling.
- Method of decoupling junction resistance from capacitance is introduced to improve RC time constant limitation.

- Asymmetric geometry effect on the rectification is expressed.
- Total efficiency of ACMIM diodes is derived and estimated as 1% for typical diode parameters.

Chapter 3

Finite Element Simulation Results

In this chapter, a proof of concept for the design of ACMIM tunnel diodes will be presented using simulation tools. The majority of the physical concepts will be modeled utilizing COMSOL Multiphysics, a Finite Element Method (FEM) based commercial software package. The main goal of this study is to observe the geometry and the material effects on the performance of the ACMIM tunnel diodes on both electrostatic and AC harmonic simulations.

3.1 Electrostatic Simulation Results

Electrostatic analysis is performed on the ACMIM diodes. For simplicity, the geometry of the rectenna is modeled within a single plane of metal film. The sharp tip of a triangular bow-tie antenna is separated from the edge of a rectangle by a small gap as shown in Figure 3.1. Throughout the analysis a constant $1V$ is applied on the triangle terminal and the rectangular terminal is grounded. The maximum magnitude of the electric field in the direction of the tip arrow (referred as “E-field Norm”) that forms at the gap is monitored to fully evaluate the geometric effects on the field enhancement.

Some important geometric parameters used in this study are as follows:

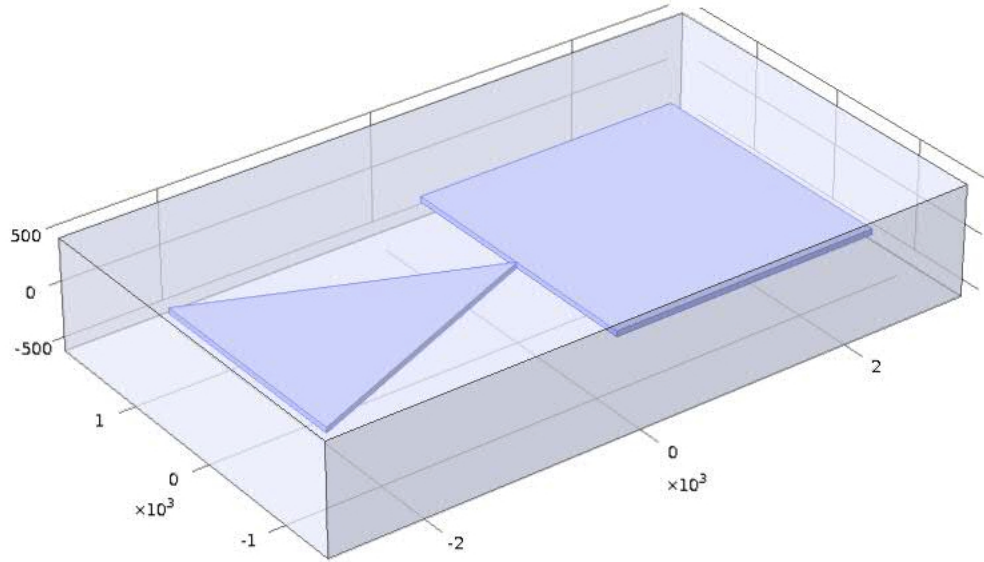


Figure 3.1: Geometric model used in the majority of the simulations. Dimension units are in nm .

L : Length of the triangle and dimension of the square

r : Radius of curvature of the tip

θ : Flare angle of the antenna

d : Gap width between the triangle and the square

t : Metal film thickness

3.1.1 Mesh Density Analysis

The validity of the solutions obtained using FEM is strictly dependent on how well the problem is discretized by meshing. Computer aided numerical modeling tool divides the problem space into discrete finite-size volume elements, over which the solution is taken as uniform. In order to convert a continuous real-world problem

into a discrete numerical model, a large number of elements is necessary.

To ensure realistic solutions, a mesh density analysis is initially performed. The electrostatics module is run on various mesh density profiles with a fixed geometry ($L = 2.5\mu m, \theta = 45, r = 5nm, t = 50nm, d = 10nm$). The maximum magnitude of E-field detected on a plane that slices the structure in the middle is used as a metric to determine the optimum mesh profile. First, the default mesh parameter combinations (normal, fine, finer, extra fine, extremely fine) are used, then custom made profiles are generated where the number of elements are increased gradually. In Figure 3.2, the convergence of the metric parameter starting from “Extremely Fine” mesh profile is shown. The mesh profile preferred in all studies has 2.6×10^6 elements. Around the junction area, which is of great importance to this study, a mesh refine box with a finer mesh density is included to get more accurate results without increasing the simulation time considerably (see Figure 3.3).

3.1.2 Tip Radius Analysis

A MIM junction with a sharp tip is indispensably important in the ACMIM design. First, it determines the degree of E-field enhancement. A sharp tip concentrates the electron transport to a small area. Thus, it minimizes the junction capacitance while the junction resistance stays constant (decouples the junction resistance and the capacitance). Moreover, the asymmetric geometry (the sharp tip is only on one side of the junction.) generates an imbalance in the magnitude of the E-field that forms at the gap. As a result, the magnitude of current flow varies

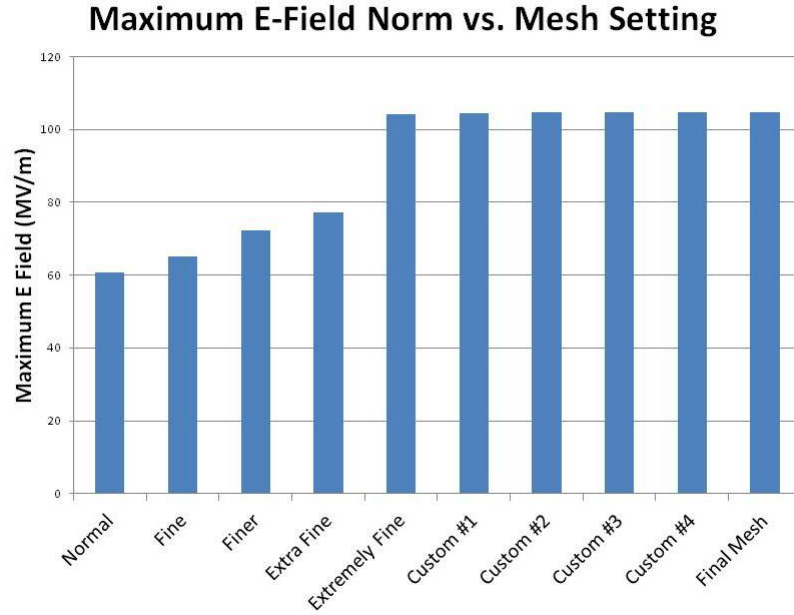
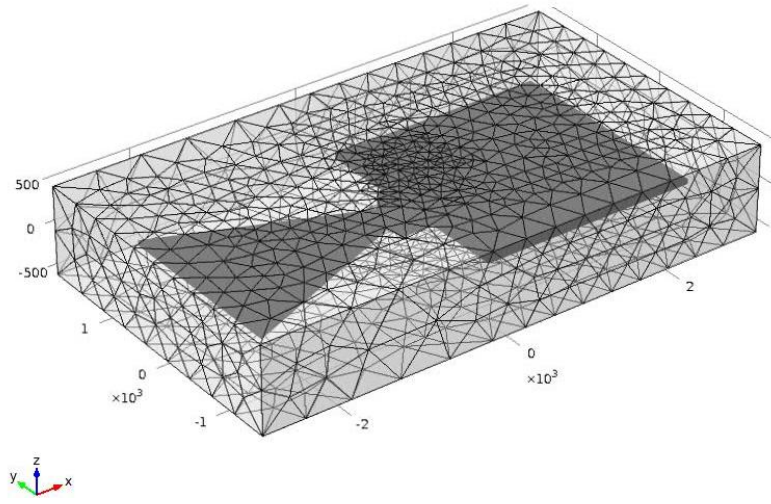


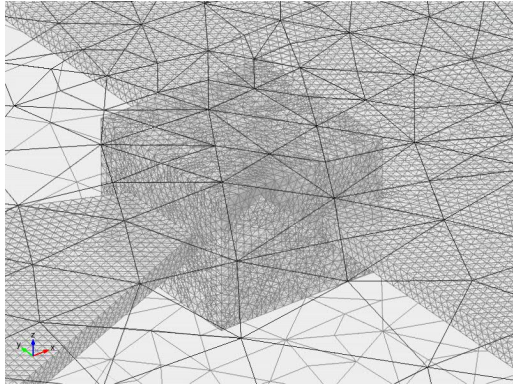
Figure 3.2: Maximum E-field magnitude values computed at various mesh profiles.

asymmetrically, facilitating rectification.

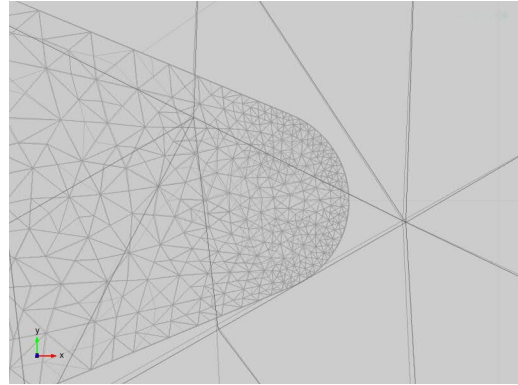
Achievable minimum tip radius-of-curvatures are dictated by process features. The resolution limit of the lithography is the most important factor. EBL is used along with the proximity effect correction to achieve the highest available resolution consistently. This allows us to get into a regime in which the tip radius-of-curvature is limited by the grain size and other thin film inhomogeneties of the metal film. This is illustrated in Figure 3.4, where two tips fabricated under identical process conditions are shown. One exhibits $10nm$ and the other a $3nm$ radius-of-curvature. This introduces a certain level of variation in the device performance as we will discuss later. In addition, the flare angle of the tip has a significant effect on the tip's radius-of-curvature. In Figure 3.5, the tips with 45° and 90° flare angles are presented. Antenna flare angle vs. tip radius-of-curvature plot quantifies the flare



(a) Whole simulation domain.



(b) Finer mesh box at the junction.



(c) Finer mesh at the tip.

Figure 3.3: Mesh profile used for FEM analysis

angle effect on the tip. For the angles less than 45° this effect diminishes, and the tip radius of curvature becomes only dependent on the lithographic resolution and the metal grain structure.

A parametric sweep is run on the asymmetric ACMIM by keeping all the geometric parameters constant ($L = 2.5\mu m, \theta = 45, t = 50nm, d = 2nm$) and changing the tip radius-of-curvature from $3nm$ to $10nm$ in $1nm$ steps. The two

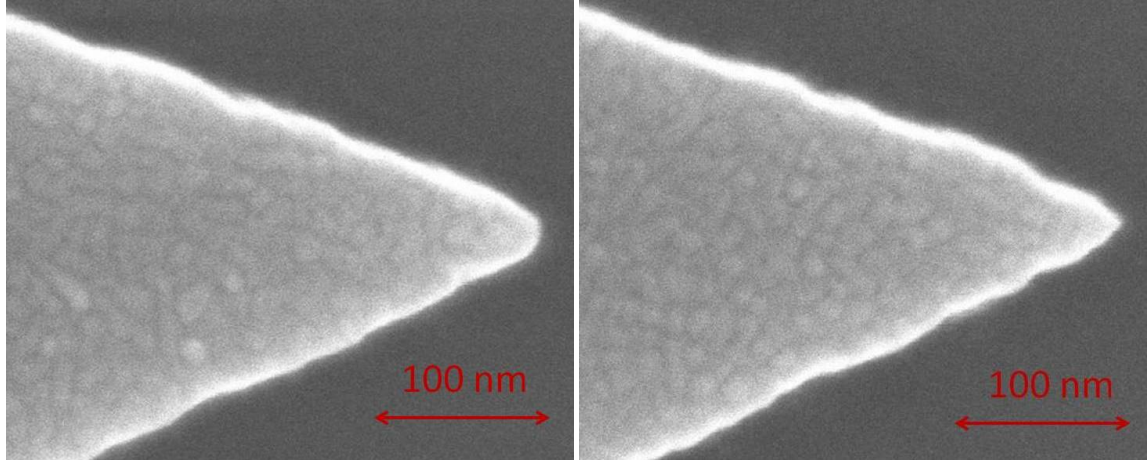


Figure 3.4: Micro-graphs of two tips with 10nm (left) and 3nm (right) radius of curvatures.

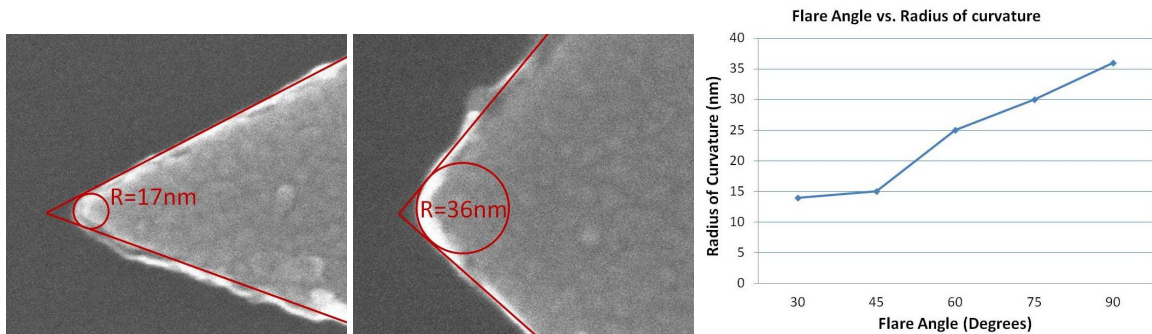


Figure 3.5: Radius of curvature of the tips with 45° (left) and 90° (middle) flare angles. Antenna flare angle vs. tip radius of curvature plot (right).

dimensional surface plots of the E-field magnitude distribution that forms as a result of a 1V potential difference is shown in Figure 3.6. The color scale (red being the highest and blue lowest field) represents the effect of tip sharpness on the E-field enhancement. Not only the maximum E-field enhancement is higher ($6 \times 10^8\text{V/m}$) in the 3nm tip (right) than in the 10nm tip ($5.3 \times 10^8\text{V/m}$), but also the high field volume is more focused in the 3nm tip.

In addition, in Figure 3.7 the E-field distribution at the gap is shown as a function of tip radius-of-curvature. These line plots disclose both the advantages of asymmetric geometry and the sharp tip electrode. Contrary to a symmetric MIM, the E-field is not uniform in the gap of the asymmetric junction. E-field peaks right next to the tip and decays non-linearly towards the flat edge. Thus, when the sharp tip electrode is negatively biased (electrons extracted from the tip) the current magnitude is higher than the case when it is positively biased (electrons are being extracted from the edge). As a result, the cathode of ACMIM tunnel diode can be defined as the sharp tip electrode. Moreover, both the magnitude of the E-field near the tip and the divergence of E-field between the electrodes increase as the radius-of-curvature decreases (see also Figure 3.8). Since the tunneling current is dependent on the E-field, it is expected to generate higher current in a smaller volume as the tip sharpness increases.

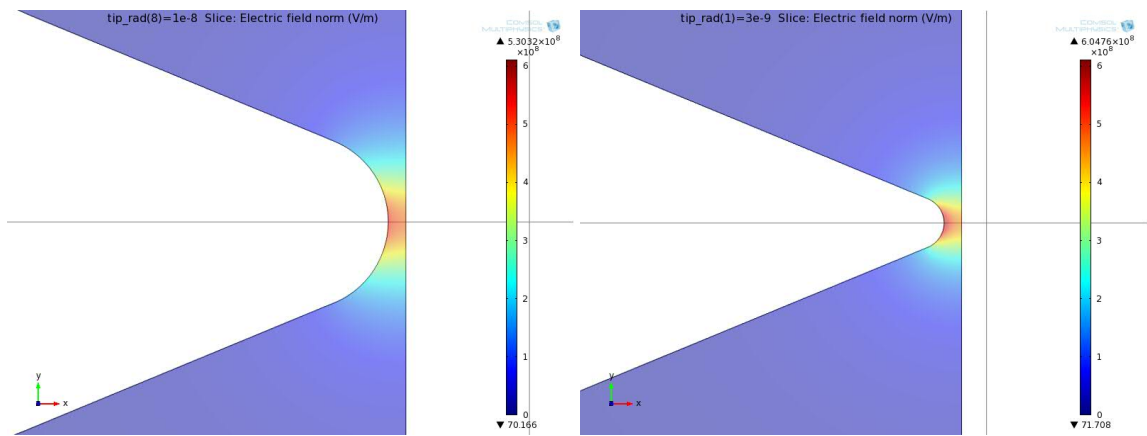


Figure 3.6: E-field norm surface plots with tip radius-of-curvature 10nm (left) and 3nm (right).

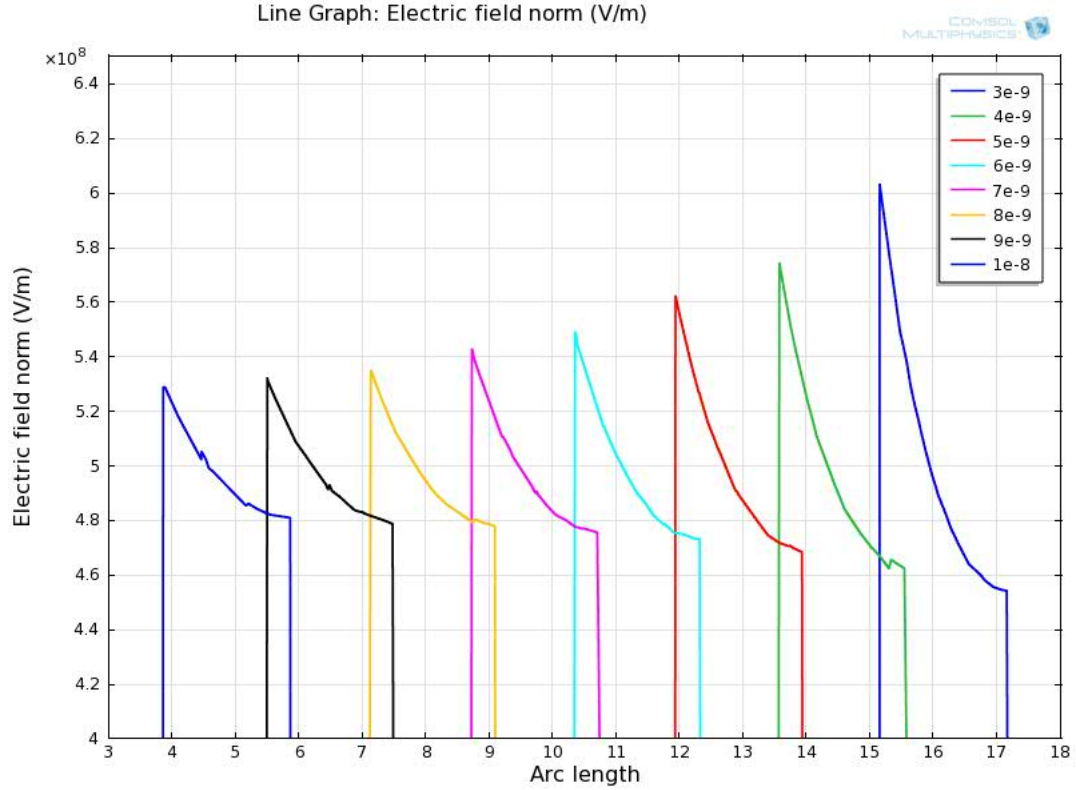


Figure 3.7: E-field norm line graphs at the $2nm$ gap with tip radius $3nm$ to $10nm$.

3.1.3 Gap Width Analysis

The gap width (the barrier width for tunneling electrons) between the electrodes is another very crucial geometric parameter in the ACMIM design. To quantify its effect on the E-field that forms between the electrodes, a parametric sweep of the gap width from $1nm$ to $10nm$ in $1nm$ increments, and then from $10nm$ to $25nm$ in $5nm$ increments is performed. In Figure 3.9, the norm of the E-field as a function of the gap width is shown. The maximum E-field decays with a rate of $x^{-0.78}$, whereas the minimum E-field decays with $1/x$. These decay rates indicate that the difference between the maximum and the minimum E-field magnitudes decreases (the asymmetric geometry effect decreases) as the gap width increases. Also

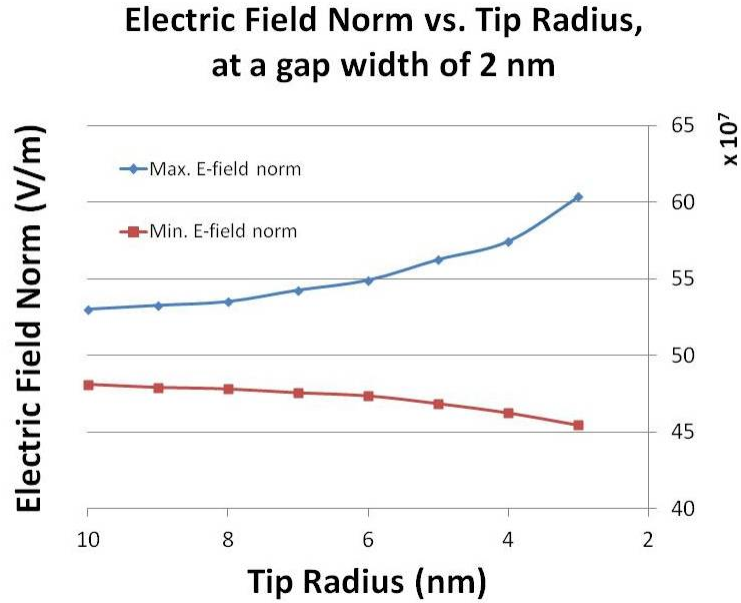


Figure 3.8: Max and Min E-field norms observed at the $2nm$ gap as a function of tip radius.

in Figure 3.10, surface plots of the norm of the E-field with gap widths $7nm$, $10nm$, and $25nm$ are shown on the same color scale. The E-field norm variation plots can be seen in Figure 3.11 for gap widths between $1nm$ and $10nm$, revealing the effect of the gap width on the E-field enhancement.

3.1.4 Flare Angle Analysis

The flare angle of the triangle electrode is important for the antenna design, particularly for the design of antenna bandwidth. To understand the effect of the flare angle on the E-field enhancement at the junction, a set of simulations are performed varying the flare angle from 30° degrees to 180° degrees (parallel plates) in 15° degree increments and keeping the other geometric parameters constant ($L =$

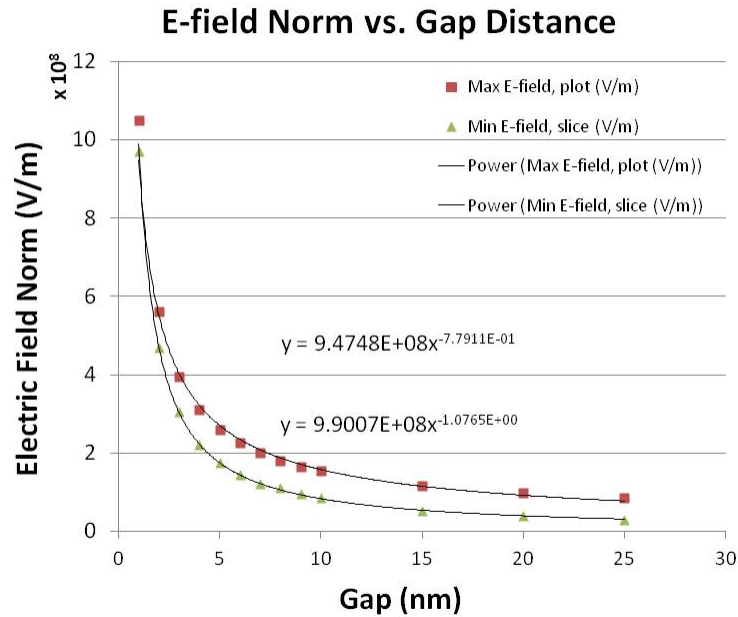


Figure 3.9: Max and Min E-field norm observed at the gap with changing gap width.

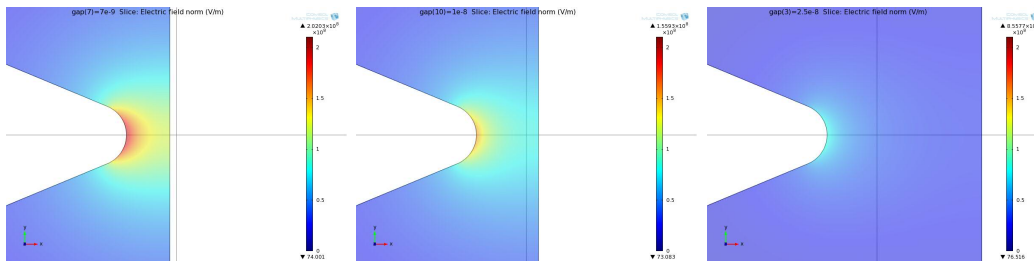


Figure 3.10: E-field norm surface plots with gap width 7nm (left), 10nm (middle) and 25nm (right).

$2.5\mu\text{m}$, $r = 5\text{nm}$, $d = 2\text{nm}$, $t = 50\text{nm}$). In Figure 3.12, minimum and maximum norms of the E-field in the gap can be seen as a function of the flare angle. The data illustrates that the E-field does not depend on the flare angle substantially for angles less than 120° . It is the tip's radius-of-curvature and the gap width that dominates the E-field distribution at the gap for flare angles $\leq 120^\circ$

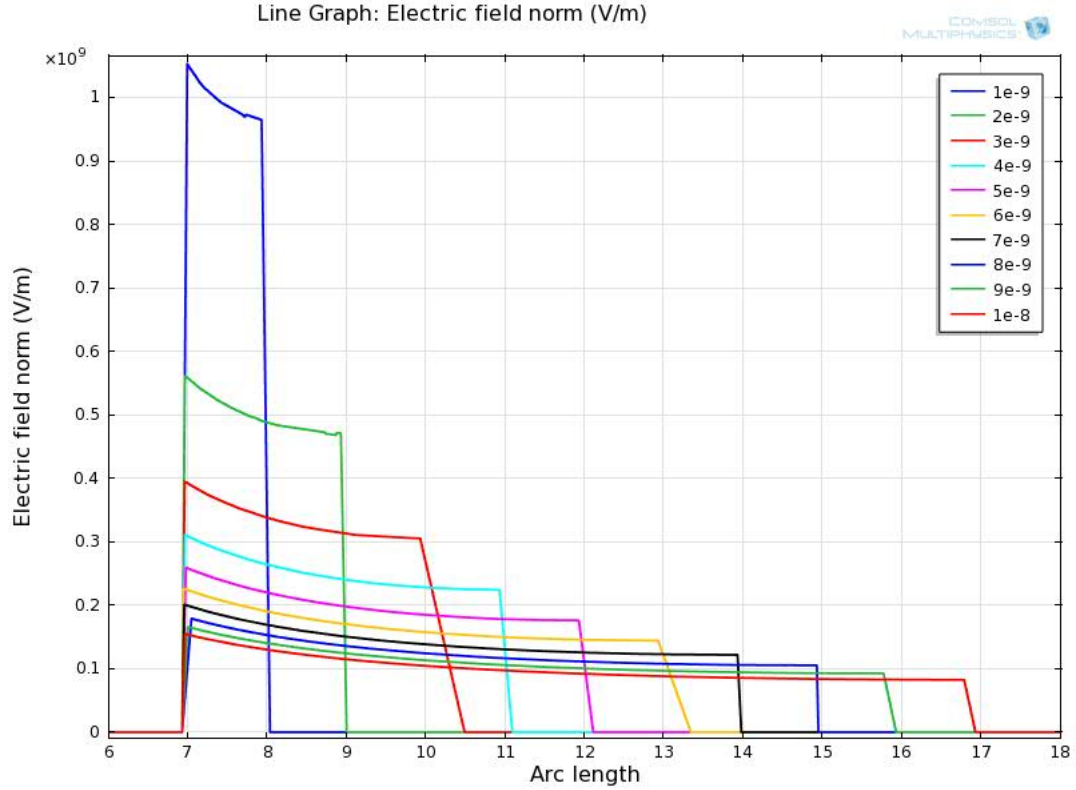


Figure 3.11: E-field norm line graphs with gap widths between 1nm to 10nm.

degrees. However, at very large angles ($\geq 120^\circ$) the E-field enhancement disappears and field distribution becomes uniform as in the case of parallel plates ($E = V/d = 1V/2nm = 5 \times 10^8 V/m$). Also, in Figure 3.13, the surface E-field distributions with two angles (30° and 150°) are shown.

3.1.5 Capacitance Analysis

The junction capacitance of the MIM junction (which determines the time constant / operation speed of the device) is one of the major considerations in the ACMIM tunnel diode design. In order to measure the geometric effects on the junction capacitance, a set of simulations is carried out. In essence, the tip

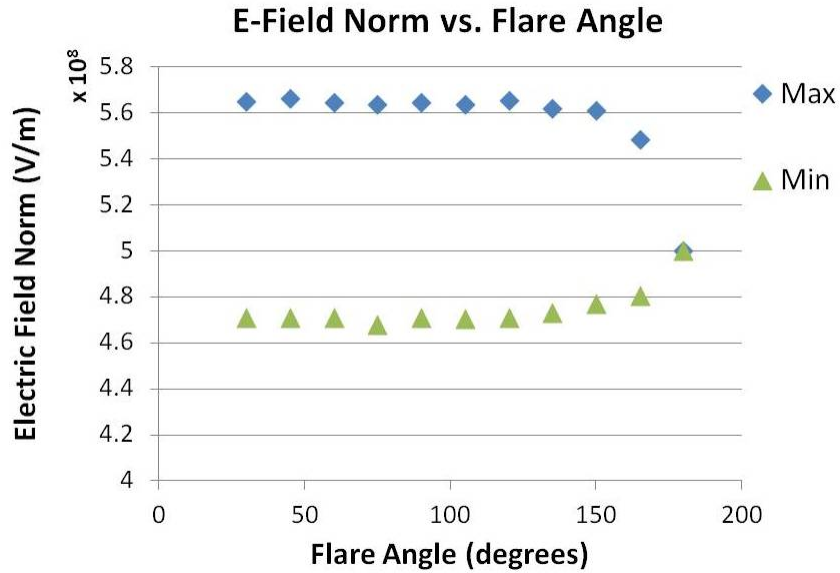


Figure 3.12: Max and Min E-field norms at the gap with changing flare angle.

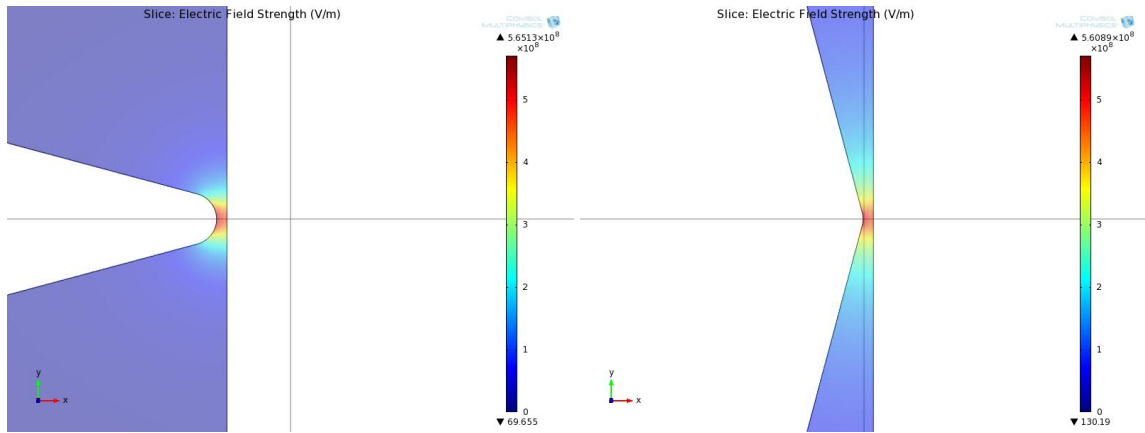


Figure 3.13: E-field norm surface plots with flare angles 30° (left) and 150° (right) degrees.

radius-of-curvature, gap width and flare angle effects are studied. COMSOL offers a built-in capacitance calculation module. In order to explore the use of this built-in feature, a concurrent voltage sweep is performed and we are led to understand that computation of the change in the total terminal charge with respect to the voltage change (dQ/dV) is COMSOL's method of capacitance estimation.

The first study demonstrates the effect of tip radius-of-curvature on the capacitance. Simulation results suggest a linear relationship where the capacitance increases as the tip radius-of-curvature rises (see Figure 3.14). According to this numerical estimation, for a geometry with $r = 3nm$ and $d = 2nm$, junction capacitance equals $C = 3.1509 \times 10^{-17}F$. Secondly, the junction capacitance decreases nonlinearly as the gap width increases (see Figure 3.15). The MIM junctions with asymmetric geometry have weaker gap width dependence than the parallel plate capacitors. This relation stems from the strong E-field enhancement-gap width relation, as shown in Figure 3.9. In this particular geometry, the charge coupling between the electrodes is highly dependent on the gap width, unlike the parallel plate capacitor where the coupling decreases linearly as the distance between the electrodes decrease. Lastly, the flare angle dependence of the junction capacitance is derived (Figure 3.16). A linear increase can be observed in the capacitance as the flare angle increases up to 120° degrees. However, for larger angles ($\geq 120^\circ$) the capacitance starts increasing rapidly as the geometry resembles a parallel plate capacitor.

3.1.6 Imperfection Effects

It is very common to encounter imperfections due to the fabrication variability and material inhomogeneity. Particularly at sub-micron dimensions patterning defects are prevalent. In Figure 3.17, a common defect observed in the ACMIM tunnel diode tip is shown. In this study, imperfection influence on the performance

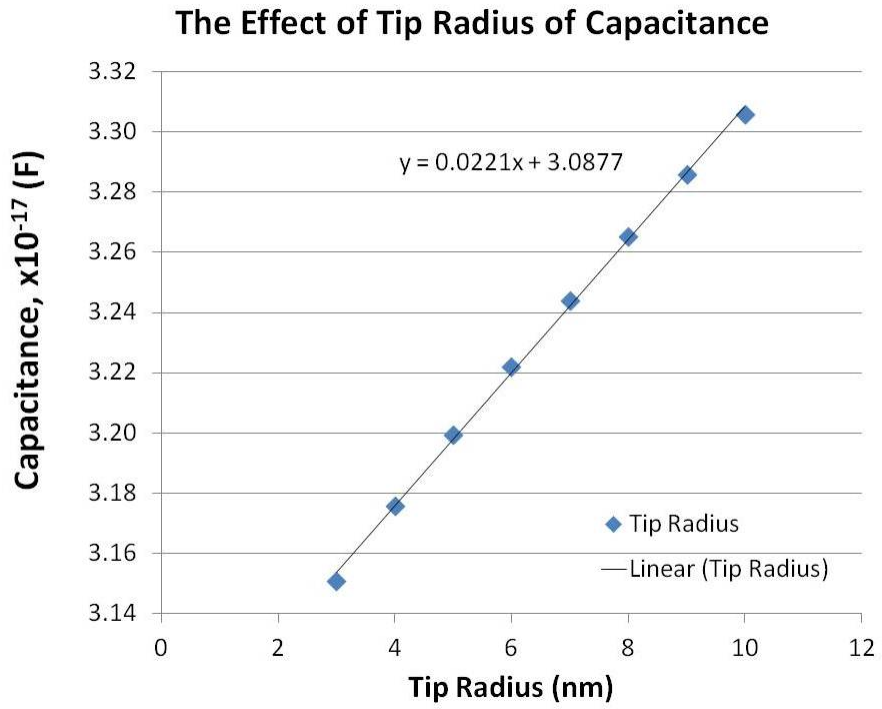


Figure 3.14: Junction capacitance vs tip radius plot.

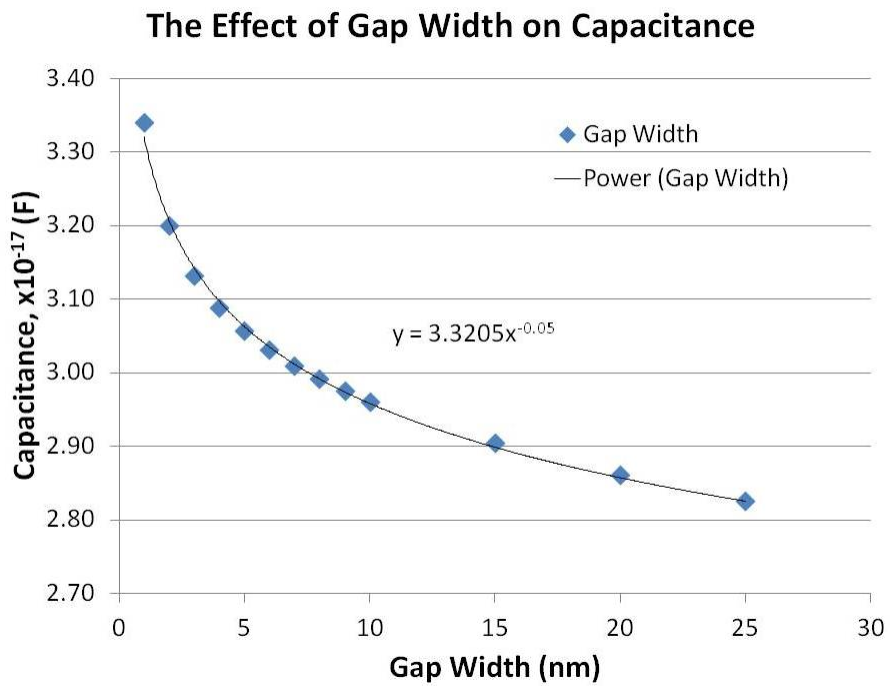


Figure 3.15: Junction capacitance vs gap width plot.

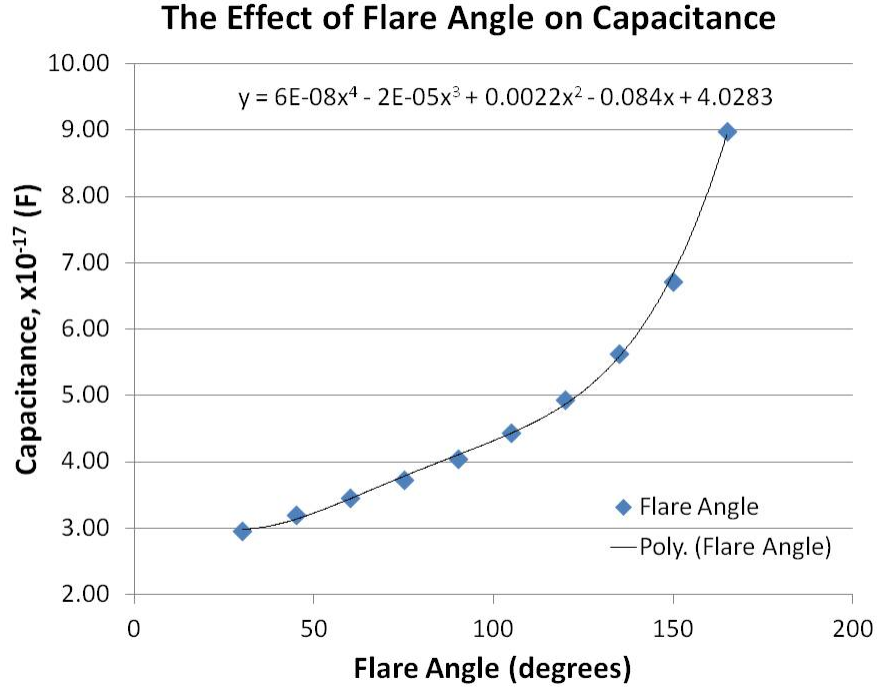


Figure 3.16: Junction capacitance vs flare angle plot.

of the device is analyzed. The imperfections are modeled by placing circles with radius-of-curvatures $1nm$ and $2nm$, with their centers located on the tip line. For comparison, a simulation is done on a geometry without imperfections ($r = 10nm$, $\theta = 45$, $d = 2nm$) and the maximum E-field norm and capacitance measured with this baseline test is $E = 5.33 \times 10^8 V/m$ and $C = 3.3 \times 10^{-17} F$, respectively.

In essence, these imperfections provide hot spots, focusing the E-field even further into much smaller volumes as shown in Figure 3.18. The efficacy of the imperfection on the E-field that forms between the electrodes depends both on its location (distance from the grounded terminal) and shape (tip radius-of-curvature). When the imperfection appears closer to the ground terminal than the major electrode tip, it boosts the E-field locally as shown in top row of Figure 3.18. In order

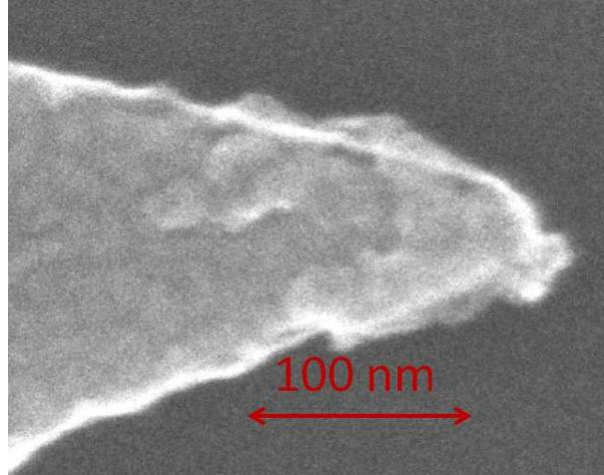


Figure 3.17: Micro-graph of a defective junction tip.

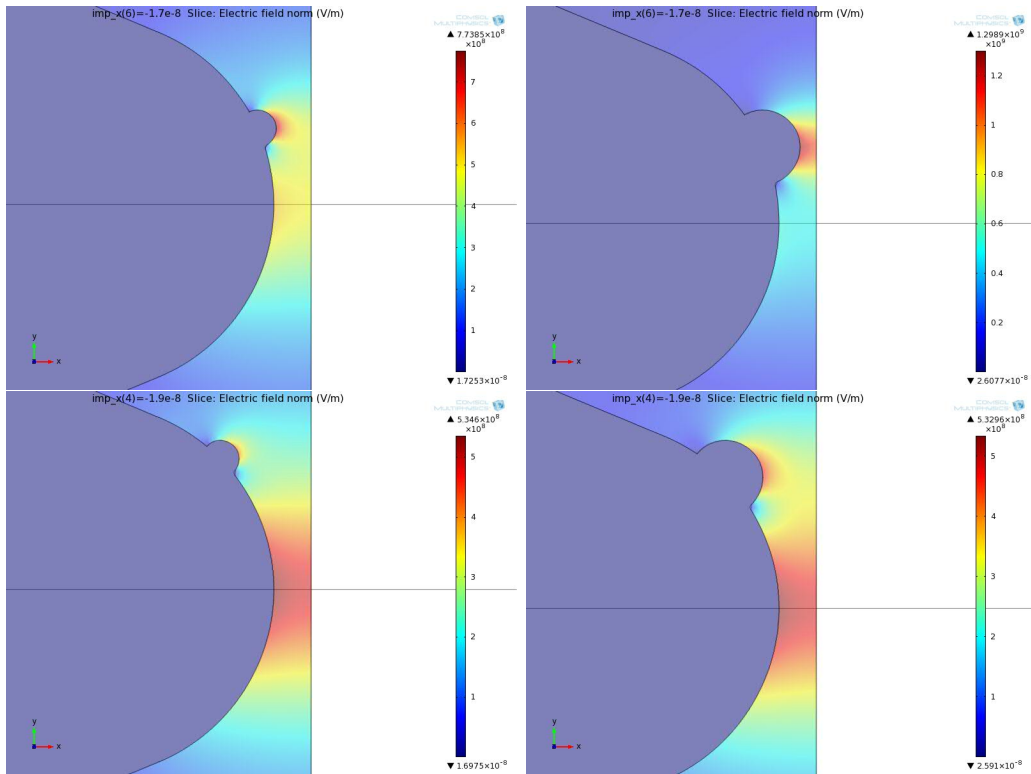


Figure 3.18: E-field norm surface plots with imperfection radius of 1 nm (left column) and 2 nm (right column) at various distances from the grounded edge.

to quantify this additional E-field enhancement, two different dimensioned imperfections are added to a particular junction geometry ($r = 10\text{ nm}$, $d = 2\text{ nm}$) and

the results are compared with the perfect tip case at certain gap widths. According to this study, an increase in the E-field magnitude at the gap is observed when the imperfection decreases the ultimate gap width ($\leq 2nm$) and the amount of enhancement is dependent on the tip radius-of-curvature, the smaller radius creating a larger E-field (see Figure 3.19).

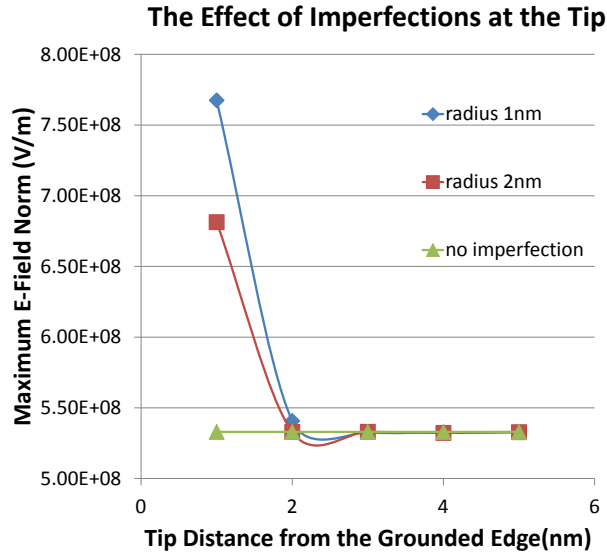


Figure 3.19: The effect of imperfections with tip radius of $1nm$ and $2nm$ on the maximum E-field norm.

3.2 Time-Dependent Simulation Results

In this section, antenna properties of the ACMIM diodes are studied. The radiation coupling of the antenna is formulated as a time-harmonic problem. For this simulation a 3-dimensional vector solution of the Maxwell equation is executed to evaluate wave propagation in different material systems for different antenna geometries. The dielectric properties of nickel at different frequencies are obtained

from Palik et al. [40]. A sphere with a Perfectly Matched Layer (PML) outer shell is used as the problem domain and simulates an infinite domain. PML layers are known as absorbing layers that are frequently used to simulate an open boundary by FEM solvers. In fact, the wave does not reflect when it goes into a PML domain when properly designed. The field coupling analysis is configured this way, because it allows for the simulation of a single antenna coupling to the radiation generated by a source at infinity without any substrate interference. In Figure 3.20, electromagnetic wave simulation domain is shown. The thickness of the PML shell is one wavelength long ($10\mu m$) and the bow-tie antenna is located at the center of a $20\mu m$ -radius air sphere.

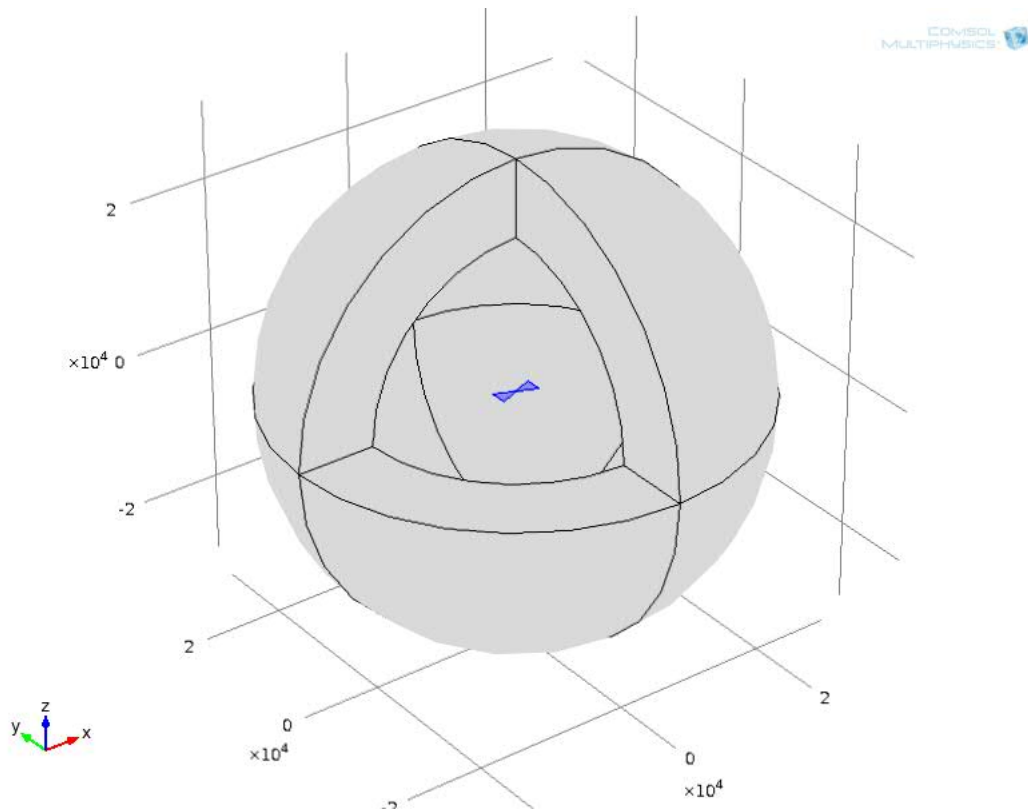


Figure 3.20: 3-D spherical simulation domain.

The results of the 3-dimensional FEM simulations strictly depend on the element size that constitutes the domain. These methods are computationally intense because they require excessive memory usage. Particularly, in the time-harmonic problems, the maximum element size has to be at least $1/5^{th}$ of the radiation wavelength to carry the radiation frequency information uniformly in the problem domain. In our simulations, maximum element size is set as $2\mu m$ ($1/5^{th}$ of $10\mu m$). However, the mesh density must be increased around the antenna boundary, particularly at the junction, to regulate a smooth mesh transition between the large air mesh elements and the small antenna features. After a careful mesh study, an adaptive gridding is developed so that the results converge with the minimum mesh element count. The mesh profile for the 3-D radiation simulations is shown in Figure 3.21.

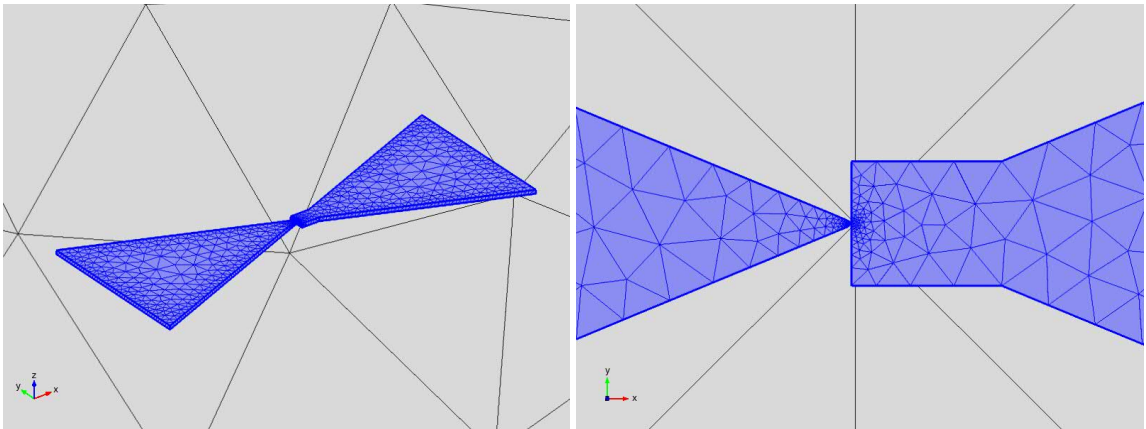


Figure 3.21: Mesh profile of the bow-tie antenna (left), focused view at the junction (right).

A plane wave of E-field magnitude of $1V/m$, $10\mu m$ wavelength, and polarized in x-direction is excited in the inner air sphere. The radiation profile is shown in

Figure 3.22. This excitation pattern in the simulation domain proves that the E-field is totally damped out in the PML layer and there is almost no distortion in the wave due to the air-PML boundary reflections.

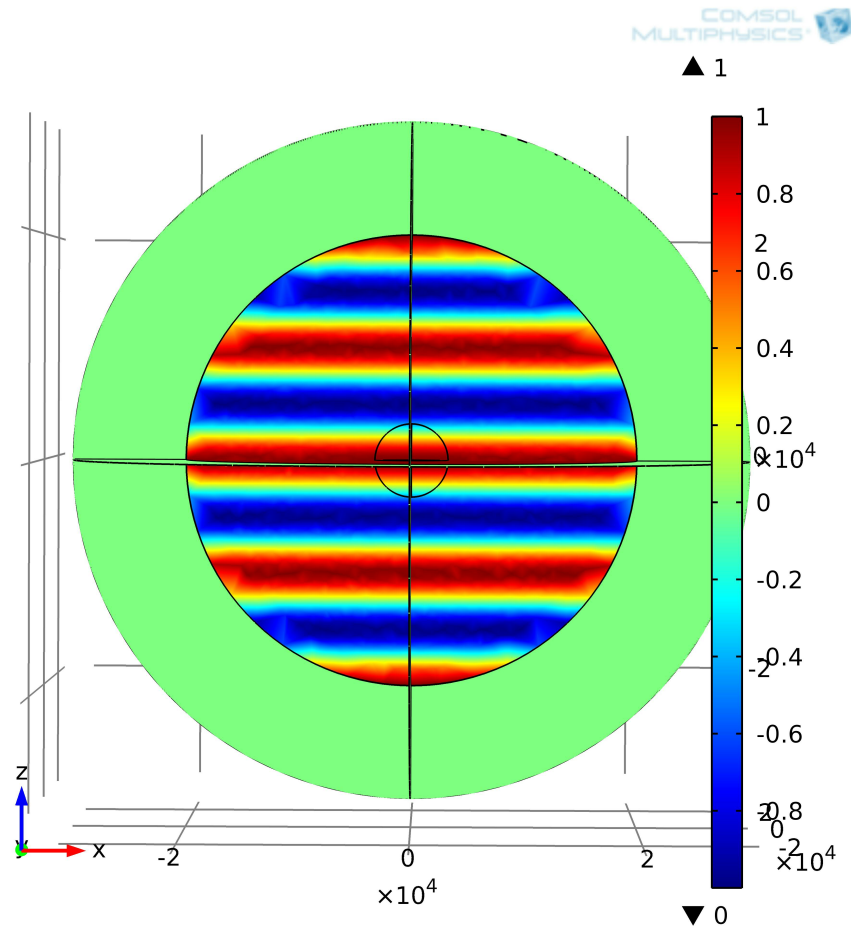


Figure 3.22: Plane wave of E-field magnitude $1V/m$ and $10\mu m$ wavelength, polarized in x-direction in the inner sphere air domain.

The antenna geometry fabricated throughout this project is simulated. With regards to the fabrication constraints, the geometry of ACMIM antennas can be approximated as follows: half antenna length $L = 2.5\mu m$, tip radius of curvature $r = 10nm$, barrier gap $g = 2nm$, flare angle $\Theta = 45^\circ$. The norm of the E-field

graph of the antenna mid-plane is shown in Figure 3.23. This computation predicts that the E-field enhances 4045 times at the tip of the junction for this particular geometry. In Figure 3.24, color scale is modified so that it scales from red (1V/m) to blue (0V/m). This new scale allows the observation of the field formation around the whole antenna geometry and the distortion created by the antenna on the whole simulation domain. In the figure, the 2-dimensional elliptical antenna radiation pattern can be observed.

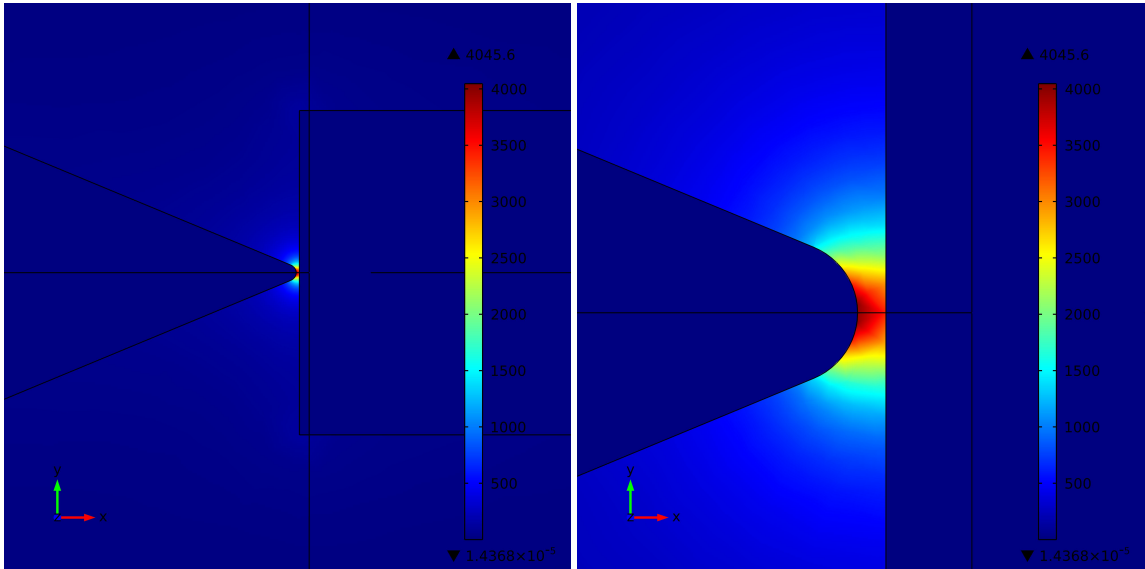


Figure 3.23: Antenna mid-plane E-field norm graph around the junction (left), focused view at the junction (right). Color scales from Red (4045V/m) to Blue (0V/m).

3.2.1 Antenna Length Optimization

In the ACMIM design, a quarter-wave bow-tie antenna is used. For a dipole antenna, the resonance length can be estimated as $\lambda/4 = 10/4 = 2.5\mu m$, which is the length used to fabricate ACMIMs in this project. To prove this concept, a

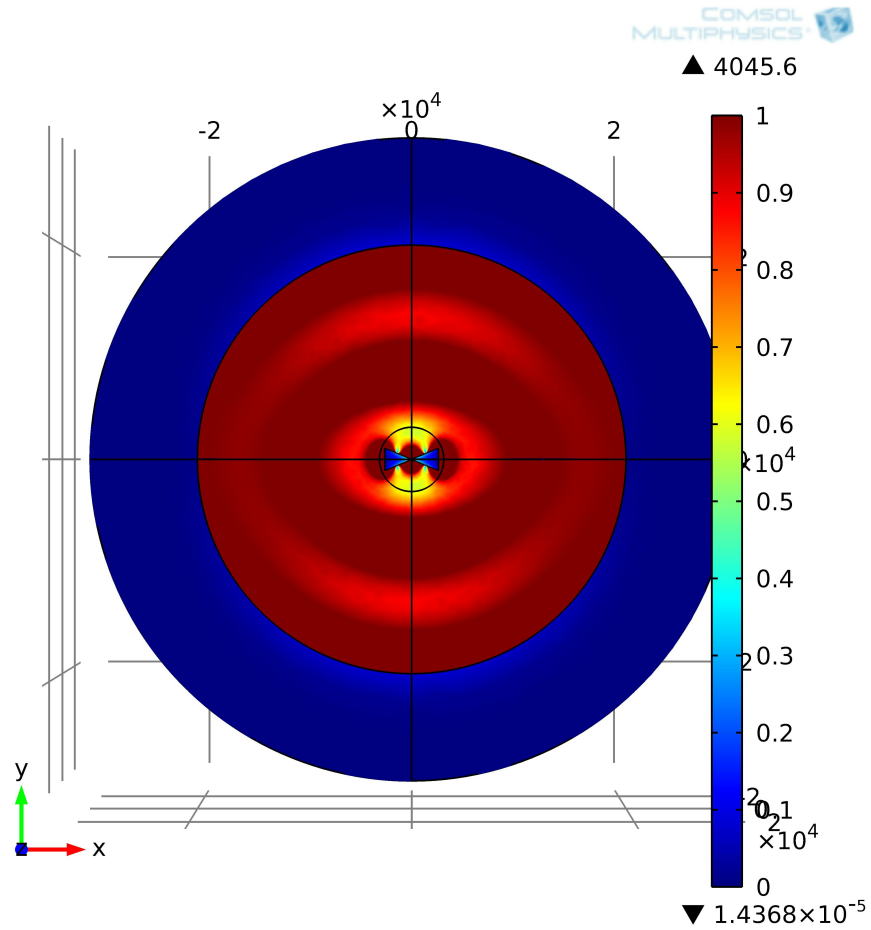


Figure 3.24: Rescaled antenna mid-plane E-field norm graph of the whole domain. Color scales from Red (1V/m) to Blue (0V/m).

parametric simulation is carried out where the antenna length is scanned from $1\mu m$ to $10\mu m$. The maximum E-field at the gap is presented as a function of the antenna length in Figure 3.25. The results report that the resonance occurs at $3\mu m$, which is $0.5\mu m$ longer than the standard dipole antenna resonance. This slight difference in the antenna length resonance is most likely due to the larger area presence in the bow-tie geometry, allowing for a higher coupling. In Figure 3.25, a second resonance can be observed around $6\mu m$.

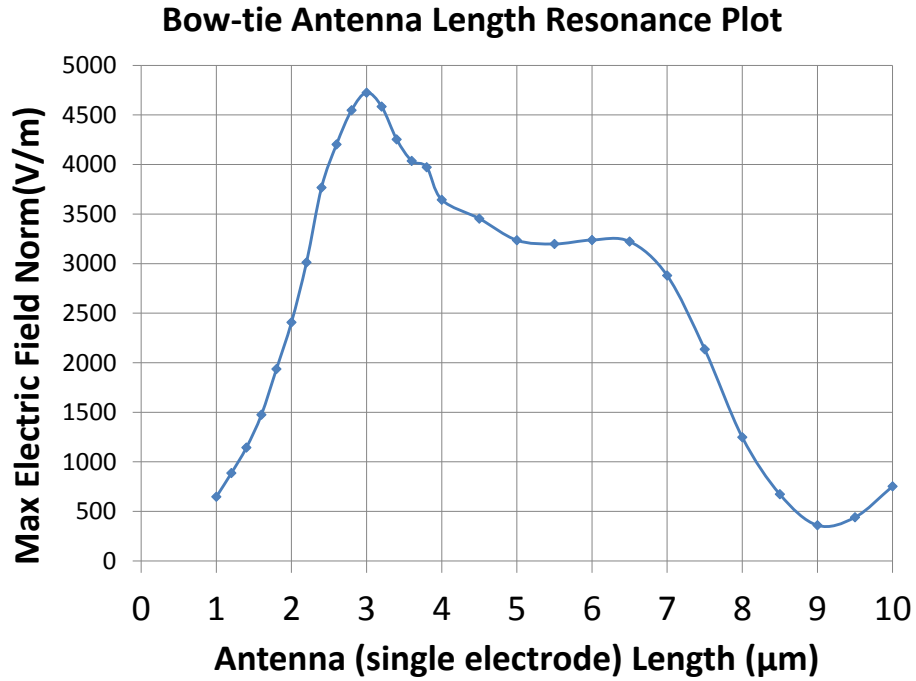


Figure 3.25: Max E-field norm as a function of antenna length.

For the $2.5\mu m$ antenna, a frequency sweep is executed from $10THz$ to $50THz$. The maximum E-field coupled is presented as a function of the radiation frequency for this constant geometry in Figure 3.26. From this plot, the Full Width Half Max (FWHM) frequency bandwidth can be deduced as $30Thz$ covering the wavelengths from $6.25\mu m$ to $16.7\mu m$. The relatively large bandwidth is a well known property of bow-tie like antennas.

3.2.2 Polarization Effects

Contrary to simple dipole antennas, bow-tie antennas do not possess a perfect sinusoidal polarization dependence function. As shown in Figure 3.27, E-field enhancement decreases below 50% of its maximum ($\leq 2000V/m$) only at a 120°

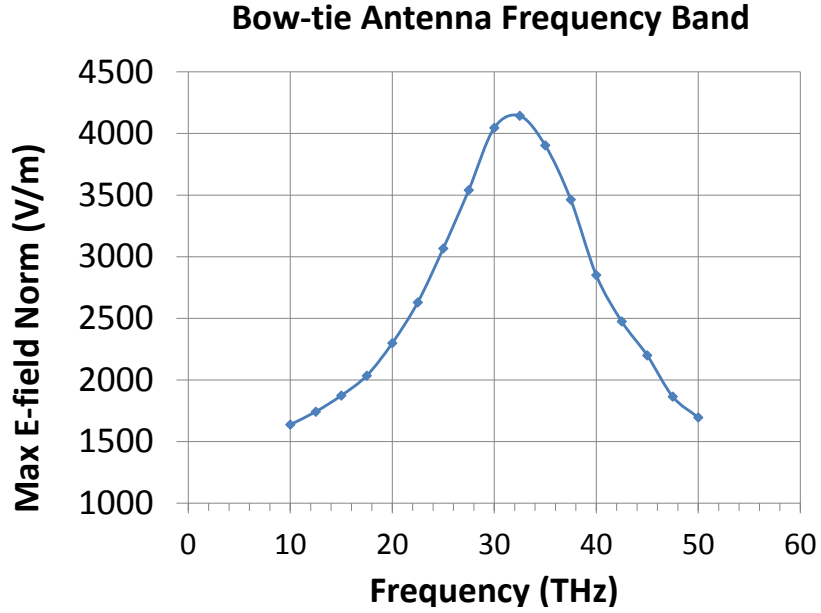


Figure 3.26: Frequency response of the $2.5\mu\text{m}$ length bow-tie antenna.

out of 360° total polarization range. The 66% of the polarization coverage (50% in simple dipole antennas) has a great significance in terms of the total coupling power when detecting/harvesting unpolarized IR radiation from the ambient. The 66% polarization coverage corresponds to a bow-tie antenna with a 45° flare angle and it may be improved by increasing the antenna flare angle.

3.2.3 Substrate and Air Coupling Comparison

The radiation coupling simulation presented so far is for the case where the antenna is surrounded by an air medium. In the real world, however, the antenna is fabricated on a SiO_2 insulating layer, which places the antenna in between two different media and disturbs the radiation pattern symmetry. In fact, the power coupling through the higher dielectric constant medium is more efficient than the air

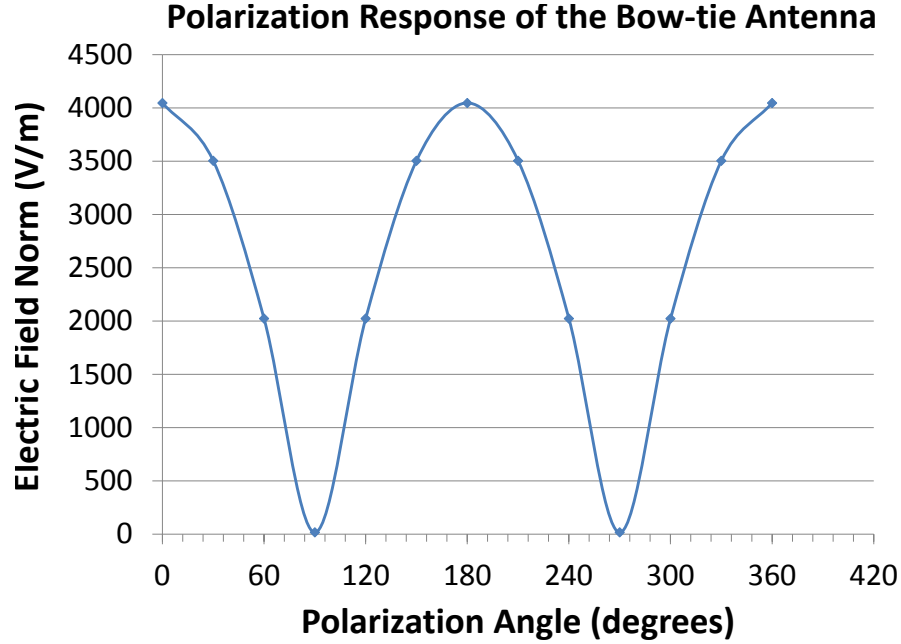


Figure 3.27: Polarization response of the bow-tie antenna.

coupling. The wave impedance in the dielectric ($Z_{SiO_2} = 190\Omega$) is smaller than the free space impedance ($Z_0 = \sqrt{\mu_0/\epsilon_0} = 377\Omega$) and this enables a better impedance matching between the radiation ambient and the antenna whose radiation resistance is $R_A = 175\Omega$ [47]

In Figure 3.28, a simulation domain where the antenna is located on a SiO_2 substrate is shown. A linearly polarized plane wave with propagation vector in either positive or negative z directions is launched. For each direction a parametric simulation is performed varying the SiO_2 thickness. Figure 3.29 shows that when substrate thickness is $3\mu m$ and antenna is excited through the substrate, field enhancement peaks at $5000V/m$, which is higher than air excitation without a substrate ($4100V/m$). On the other hand, when the excitation is through the air and

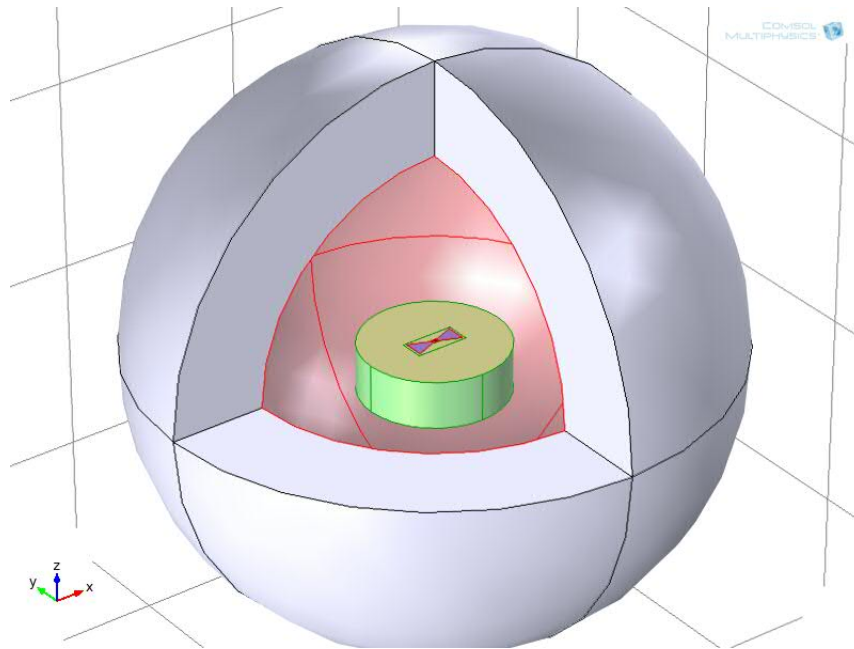


Figure 3.28: Max E-field norm as a function of antenna length.

substrate exists, field enhancement has the lowest values independent of the substrate thickness. This study suggests that it is possible to improve antenna coupling, when the excitation is sent through a properly designed (material and thickness) medium.

3.3 Summary

According to electrostatic simulation results:

- a small tip radius of curvature improves the E-field at the gap while decreasing the junction capacitance.
- a narrow gap increases both the E-field between the electrodes and the junction capacitance.

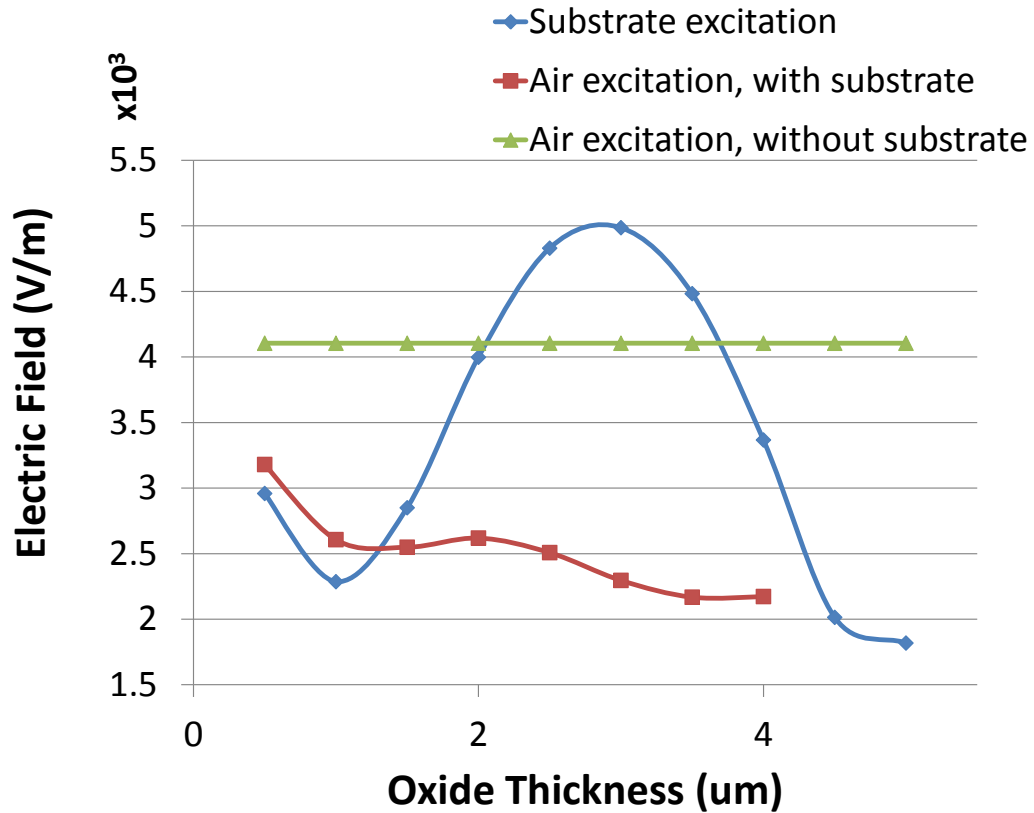


Figure 3.29: Max E-field norm as a function of antenna length.

- flare angles less than 120° does not effect the field enhancement, but the junction capacitance increases consistently as the flare angle increases.
- imperfections at the tip form hot spots and enhance the field further locally when they are close to the tip.
- E-field is not constant in the gap. It peaks at the tip and decays exponentially towards at the flat edge.

According to time-dependent harmonic simulation results:

- for $10\mu m$ wavelength radiation, antenna length resonance occurs at $3\mu m$.

- for a $L/2 = 2.5\mu m$ antenna, E-field enhances 4000 times at the gap.
- a bow-tie antenna with 45° flare angle provides minimum 2000 times E-field enhancement for 240° polarization span.
- a bow-tie antenna with 45° flare angle had FWHM frequency band of 30THz covering wavelengths from $6.25\mu m$ to $16.7\mu m$.

Chapter 4

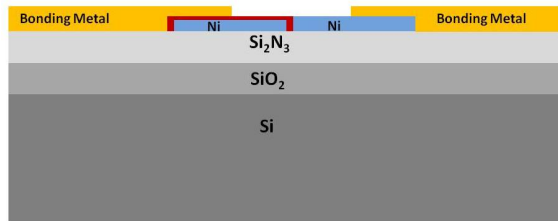
Fabrication

This chapter details the ACMIM diode process methods. The choice of substrate is discussed first. Then the main lithography method -Electron Beam Lithography (EBL)- is described along with the resolution improving EBL Proximity Effect Correction (PEC) implementation and the multi-step process alignment methods. Device material selection and fabrication methods are also explained. Finally, device packaging is described.

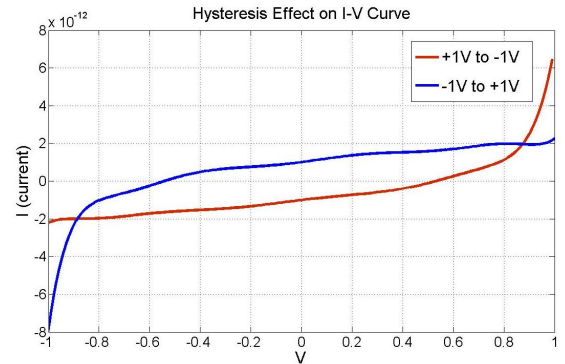
4.1 Substrate

The substrate that provides a platform for the ACMIM tunnel diodes is not only crucial for the device operation, but it also affects the design of the fabrication flow. An insulating substrate is necessary, first, to eliminate any substrate leakage so that the dominant conduction mechanism between the electrodes is solely the tunneling current. Second, the insulating layer must be thick enough to reduce capacitive coupling of the metal leads and contacts to the conductive base. On the other hand, it is challenging to perform EBL on non-conducting substrates due to the well known “charging problem”. When there is no charge bleed layer providing a discharge path for the incoming electrons, the negative charge accumulates locally creating beam deflection and pattern distortion.

Silicon substrates are used throughout this work as a device fabrication platform as they are relatively inexpensive, flat and can easily be diced into separate “chips”. Initially, a dual insulation layer ($50nm$ SiO_2 or $100nm$ Si_3N_4) is deposited over the wafer. The resulting $150nm$ insulator film is thin enough to avoid the resolution-degrading charging problems of EBL. In addition, the Si_3N_4 film promotes good Ni adhesion. However, an insulator film of $150nm$ thickness is not sufficient to eliminate capacitive coupling with the substrate. As a result, IR response was not detected by the devices fabricated on this substrate. The capacitive coupling prompted a hysteresis effect in the current-voltage relation of the devices fabricated on the substrate described above. The cross-section of the ACMIM diodes together with the contact/lead metalization and the resultant hysteresis effect are shown in Figure 4.1 (a) and (b), respectively.



(a) Cross-section of ACMIM tunnel diode and substrate



(b) Hysteresis effect on I-V curve

Figure 4.1: Capacitive coupling problem with $150nm$ thin insulation layer substrate. The difference between the I-V curves generated by sweeping the voltage from negative to positive and positive to negative is due to the transient substrate capacitance charging.

To reduce the parasitic capacitance, a thicker ($1.5\mu m$ and $5\mu m$) SiO_2 layer is grown on the Si substrate and a thin ($100nm$) Si_3N_4 layer is deposited using PECVD at $300^{\circ}C$ temperature on top as an adhesion layer. The EBL charging problem is alleviated by adding a conductive polymer (aquaSAVE[®]) to serve as a charge bleed layer over the resist, and increasing the acceleration voltage of the electron beam from $10kV$ to $30kV$ (maximum available on the EBL tool). IR detection at $10\mu m$ incident wavelength is achieved by the devices fabricated on the substrates with the thicker insulator layers.

4.2 Electron Beam Lithography (EBL)

EBL is used to pattern ACMIM tunnel diodes. The RAITH eLine direct write e-beam system at the UMD-FabLab facility provides beam accelerating voltage in the range of $10-30kV$. Depending on the resolution requirement of the pattern $10kV$ or $30kV$ accelerated beam is used. Before every lithography step the substrate is cleaned with a standard acetone-methanol-IPA cleaning sequence. For the positive resist process, PMMA A4 is spin-coated at $5krpm$ to yield a $200nm$ -thick resist. A pre-bake process is applied by keeping the substrate on a $180^{\circ}C$ hot plate for 90 seconds. After the exposure, MIBK-IPA (1:3) solution is used to develop the resist for 60s. The chemical developing process is stopped by keeping the sample in an IPA bath for 30s.

The highest lithographic resolution achievable on a routine basis is through particle beam technology. EBL tools are ubiquitous, and issues in achieving reso-

lution targets have been widely researched. The project at hand stresses two areas of this particular technology: proximity effect control and alignment. We address these issues in sequence below.

4.2.1 EBL Proximity Effect Control

Resolution is limited by a number of different physical phenomena in lithography. In optical lithography, diffraction ultimately limits resolution, whereas in EBL it is not an issue. The wavelength of the electrons shot in the beam is far smaller than target feature sizes. Indeed, EBL systems can focus electrons to spot sizes smaller than $10nm$ in diameter when incident on the patterned surface. However, as soon as the highly focused electron beam enters the resist, electron interaction in the resist and the substrate cause undesired energy to be delivered to points that are far from the incident beam point. This unwanted exposure on unintended regions of the resist is called Proximity Effect (PE) and it is the main source of resolution constrain in EBL [6]. New device applications, whose success relies on the ultra-high resolution promised by EBL, must overcome this effect to achieve nanometric dimension control.

4.2.1.1 Implementation of PEC Method on Planar ACMIM Diodes

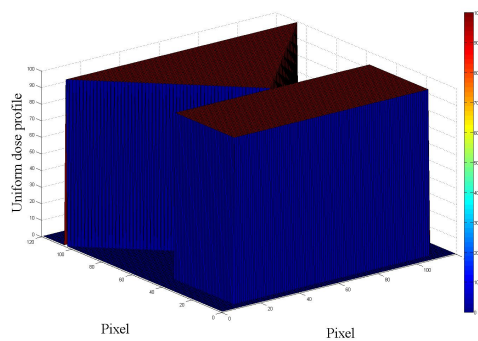
The ultra-high resolution demands created by new applications can only be sustained by the EBL that is supplemented by an aggressive PEC. For the fabrication of planar ACMIM diodes a dose modifying PEC that uses “Linear Optimization”

tools is implemented [59] and the results are presented below. (Details of the PEC method are given in Appendix B.)

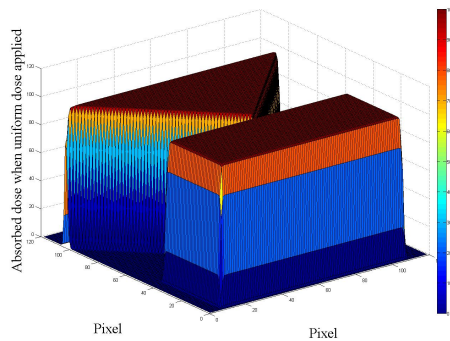
The architecture of asymmetric ACMIM diode needs high accuracy in the nano-scale. As in any antenna design, the dimensional fidelity of the asymmetric bow-tie antenna structure determines the capability of the device. Therefore, the antenna segment dimensions need to be constant while the smallest area and the narrowest gap requirement at the tunnel junction (the triangle and the rectangle patterns get closest) are satisfied. The biggest challenge is bridge forming between the rectangle and the triangle antenna parts caused by PE. PEC method that is based on dose modulation and uses the linear optimization theory is employed to prevent the bridge-forming problem.

The simulation results for the asymmetric bow-tie antenna pattern are given in Figure 4.2. Absorbed dose matrices before and after the PE correction are shown in Figures 4.2 (b) and (d) as a result of the applied dose matrices shown in 4.2 (a) and (c), respectively. It is clear in these plots that increasing the dose factors on the corner and edge pixels compensates the deficiency in PE modified cases. The PEC improves the edge slope of the absorbed dose that can be observed at the color variations at the edge pixels.

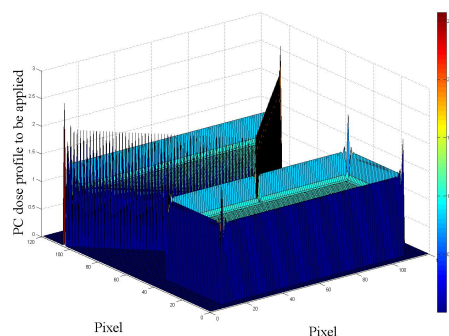
In Figures 4.3 and 4.4 the SEM images of asymmetric antenna structures fabricated with and without PEC implementation can be seen, respectively. In this particular implementation of the PEC method, the main goal is to form the minimum gap between the triangle and the rectangle antenna parts while maintaining the antenna dimensions at desired values. The structure in Figure 4.3 stands out



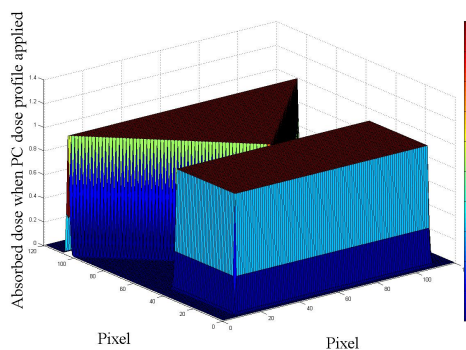
(a) Uniform Dose Profile



(b) Absorbed dose profile of uniform dose



(c) PEC modified dose profile



(d) Absorbed dose profile of PEC

Figure 4.2: Asymmetric antenna pattern applied and absorbed dose profiles with and without PEC.

due to its small gap size: $2nm$. On the other hand, in Figure 4.4 the best result achieved before the shape fidelity gets extremely distorted without PEC is given. Even though this device was fabricated with a dose factor 15% lower than the other structures, bridging persists.

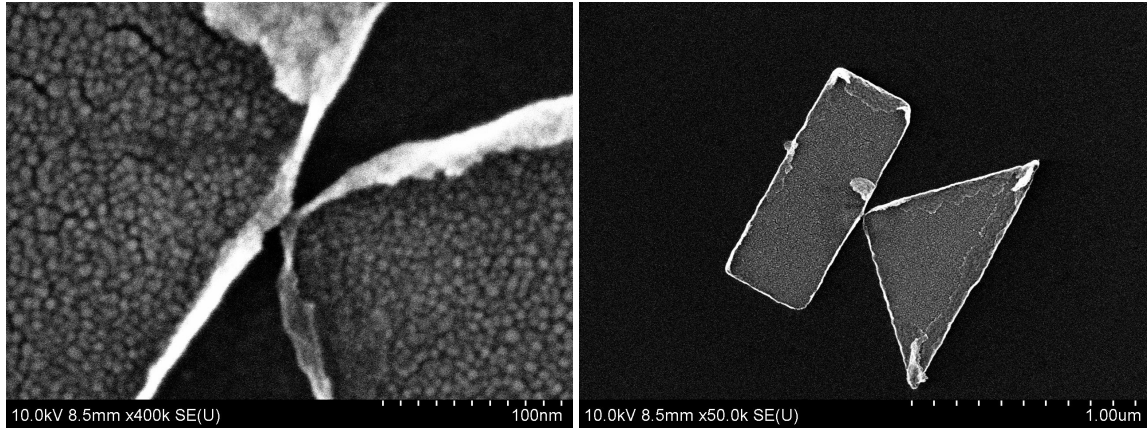


Figure 4.3: Planar MIM junction with 2nm gap achieved on the PEC applied pattern

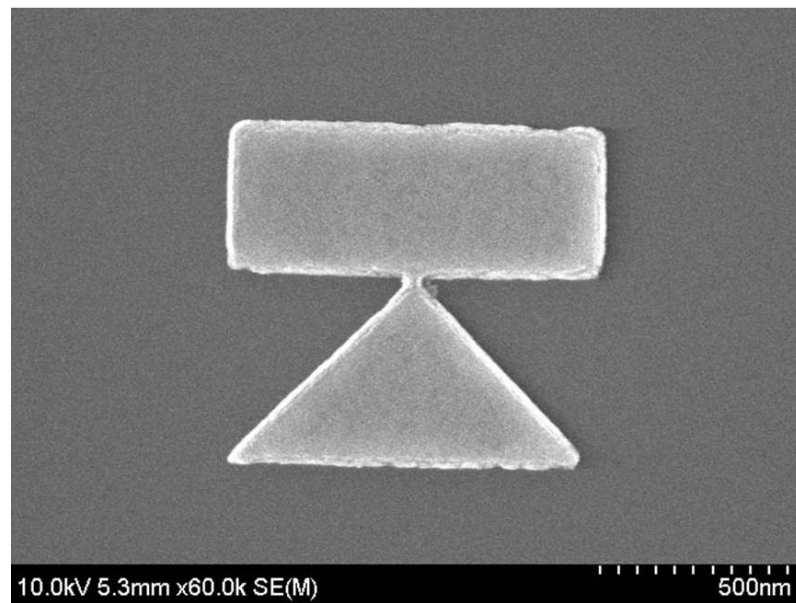


Figure 4.4: Asymmetric antenna structure fabricated without PEC

4.2.1.2 Adapting PEC to ACMIM Patterning

The success of the PEC method described above has been proven on the fabrication of asymmetric, planar MIM pattern. The dose distribution matrix of this software is used throughout this work. The direct result of this PEC software comes in an array of different dose assigned square pixels. Defining the main pattern on

the EBL mask in square pixels not only degrades the resolution- particularly on the angled tip-, but also increases the exposure time as the pattern generator has to process each pixel with a different dose scale. Therefore, it is neither necessary, nor practical to use the direct solution of the PEC software. Instead, the mask is drawn using the built-in software of the EBL tool and then the dose is scaled locally (inspired by the results of the PEC algorithm) at the critical areas, such as the narrow tip. Figure 4.5 shows three levels of dose assigned on the ACMIM pattern depending on the dimension of the feature, larger contact area (green) has the lowest and the critical tip (red) has the highest scale of dose.

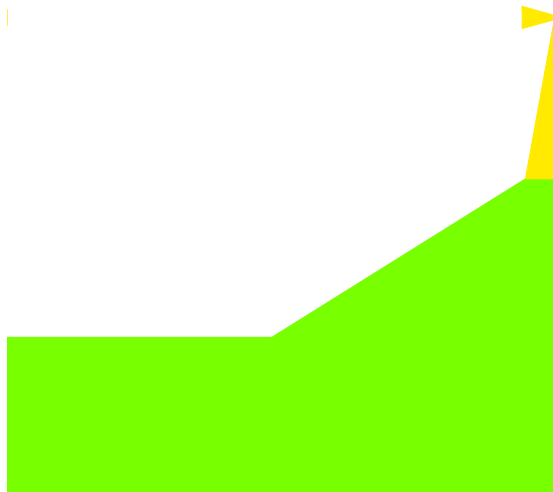


Figure 4.5: Manually implemented PEC with three dose levels green being the lowest and red highest.

4.2.2 EBL Aligning

In multi-layer EBL patterning, accurate aligning is an important key to success. Double-step EBL is frequently used in ACMIM fabrication. It offers two

advantages: eliminates the cross pattern interaction (inter-shape proximity effect) and brings flexibility in MIM junction area definition.

Most EBL tools work by deflecting an electron beam by a “Pattern Generator” that moves the beam and performs the exposure according to the designed mask. The maximum area that the beam can reach without the stage moving is called “writefield”. It is very important to align the writefield with the X-Y coordinate system of the stage to get well positioned pixels. Even with a perfect writefield-alignment Raith EBL tools are expected to have a minimum of $60nm$ placement accuracy (also called stitching error) between the write fields due to the vibration, coulomb charging and thermal drift effects. Since $60nm$ stitching error cannot be accommodated in the ACMIM fabrication, individual writefield alignment is necessary within each writefield.

A writefield of $100um$ is used in ACMIM fabrication that allows for $1.6nm$ minimum resolution. In Figure 4.6 (a), first half of the ACMIM (lead, probing pad and the align marks), which is patterned in the first step, is shown in a single writefield. The second part of the pattern, shown in figure 4.6 (b), is exposed after the beam is positioned according to the pre-patterned alignment marks during the second step of EBL. The two overlapped layers are also shown in figure 4.6 (c).

There are two important factors for a successful alignment: the align mark minimum feature size and the material that the align mark is made of. The atomic number of the material observed under SEM is important because it determines the degree of back-scattered electrons that reach the detector and form the image. In Figure 4.7, backscattering yield is given as a function of atomic number [2].

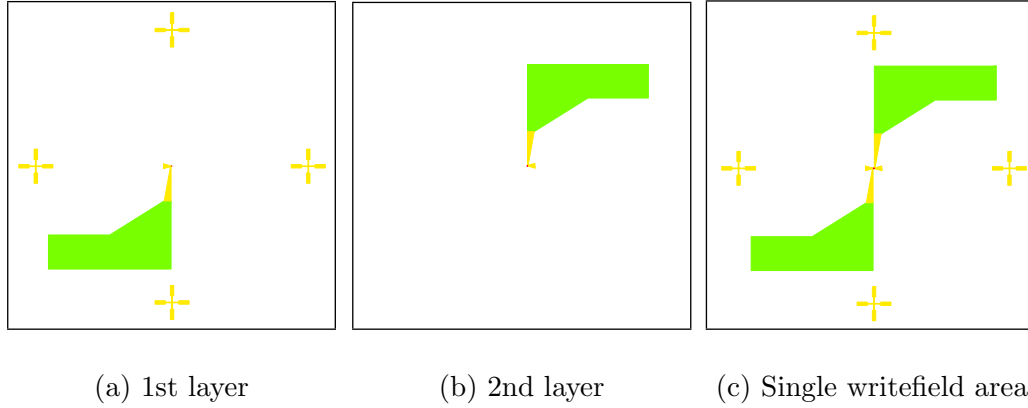


Figure 4.6: Multi-layer EBL patterning mask

Ni (atomic number 28) has a backscattering yield of 0.3 and it provides enough contrast with the substrate, which allows for an accurate alignment. In the ACMIM fabrication, align marks with minimum feature size of $200nm$ (cross) is sufficient. In Figure 4.8, two micro-graphs showing ACMIM diodes with $\leq 20nm$ error are presented and these results have been consistently reproduced.

4.3 Materials

In the design of ACMIM tunnel diodes, material selection plays an important role. Traditionally, metals such as Al, Au, Ti, Pt, W and Ni are frequently used in MIM junctions. First, highly doped polysilicon is considered as ACMIM material for this project. Si being a semiconductor allows for the control of the conductivity via the mobile carrier concentration, which determines the plasma frequency. A polysilicon ACMIM can be designed as a plasmonic rectenna where the surface plasmon resonance can occur at IR frequencies corresponding to the polysilicon plasma frequency. The polysilicon ACMIMs offer the prospect of designing tunable optical

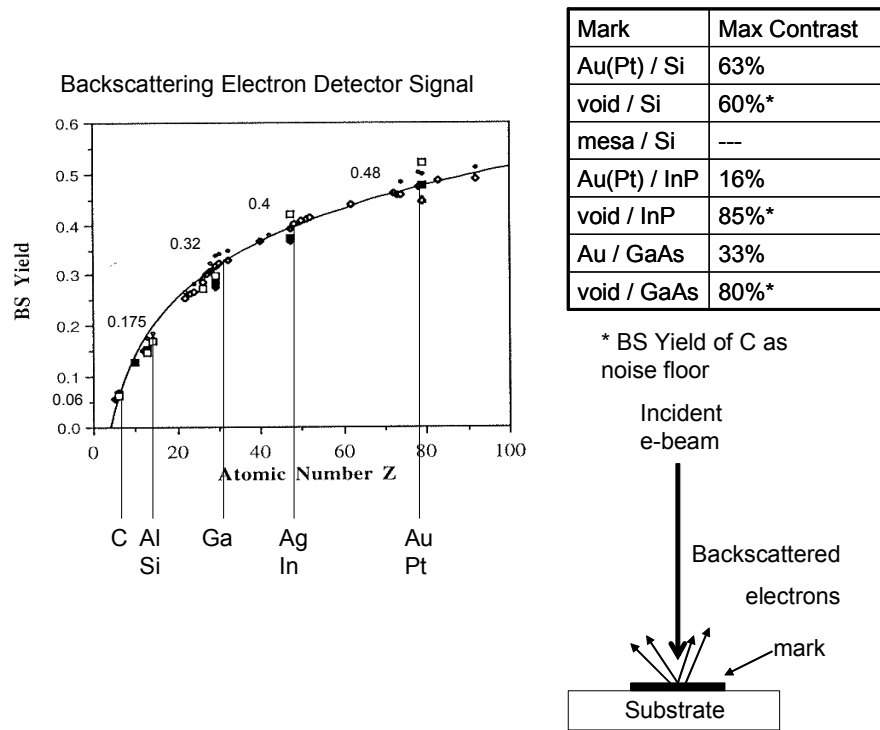


Figure 4.7: Backscattering yield as a function of atomic number Z [2]

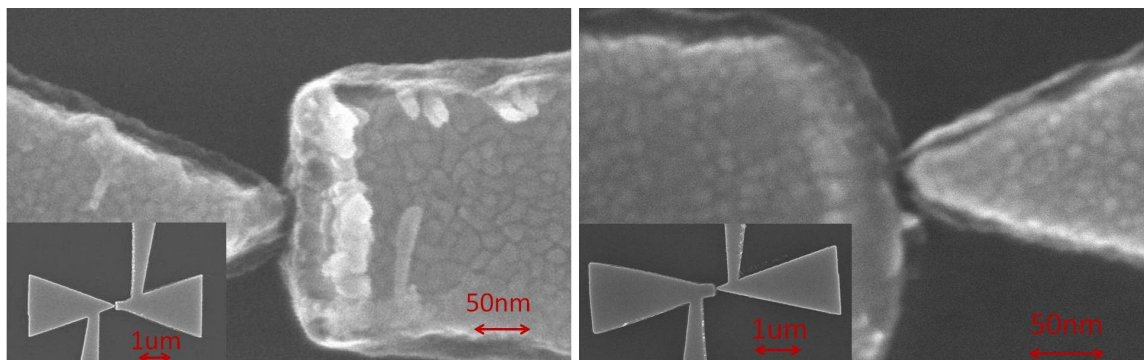


Figure 4.8: Planar ACMIM diode junctions fabricated in two EBL steps after a fine alignment.

antennas. (However, due to the fabrication challenges, the research on polysilicon ACMIMs has been ceased.) The details of the polysilicon ACMIMs will be discussed in Section 4.4.1.1.

In addition to the PolySi/SiOx/PolySi MIM junctions, PolySi/SiOx/Ti/Au,

Al/AlOx/Ni, and Ni/NiOx/Cr/Ni material combinations are also exploited in the frame of this work. However, due to the process limitations, cost effectiveness and material properties, Ni/NiOx/Ni material combination is widely studied. Ni is not only a cheap and abundant metal, but it also allows for an easy surface oxidation control in the ambient due to its slow oxidation rate [1]. In addition, Ni is one of the very few metals that have a very small band edge offset ($0.2eV$) with its native oxide [25]. This is a superior property for the MIM tunnel diodes because the turn-on voltage necessary to bring the device in the Fowler-Nordheim regime, where the efficient tunneling occurs, is very small. Lastly, as discussed before, Ni allows for the efficient scattering of electrons and provides high contrast SEM imaging, which is necessary for high precision lithographic alignment. Our best results are achieved with the Ni ACMIMs.

4.3.1 Ni Oxidation Methods

The insulating thin film barrier is a crucial component of the tunnel diode design. It is necessary to form a thin, uniform and durable oxide film that allows for efficient tunneling, while providing long-term operation. Since Ni is selected as the rectenna material, the native oxide of the metal is used to form the barrier of the tunnel diode. In Figure 4.9, Ni surface oxidation analysis is shown at room temperature and higher temperature [1]. This data reveals that the room temperature surface oxidation is negligible even after long-time O_2 -exposure, and at $550K$ one can observe several monolayers of NiOx formation. Since Ni is not an active element

and has slow oxidation cycle, it allows for the controlled oxide barrier formation in the fabrication process.

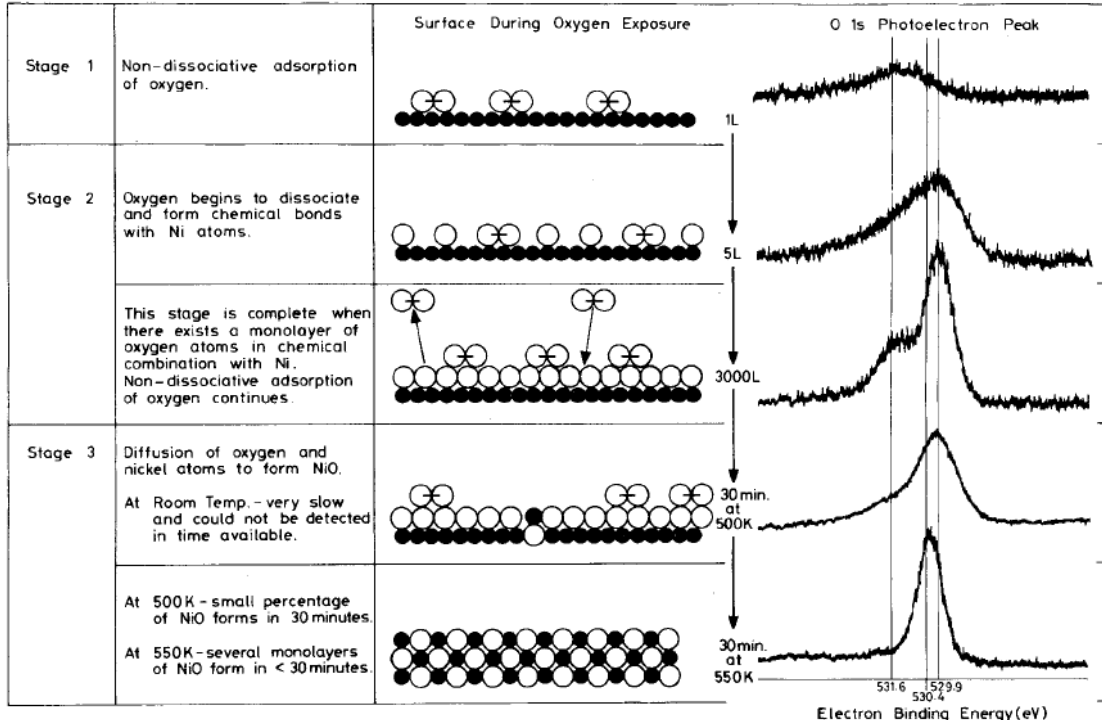


Figure 4.9: Ni surface oxidation stages[1].

Three different Ni oxidation techniques are studied to identify the optimum barrier of ACMIM tunnel diodes: O_2 plasma oxidation, DI water oxidation and saline water oxidation. DI and saline water oxidation is performed at $100^{\circ}C$. The saline water solution is prepared as $0.17M$ NaCl solution. Oxidized Ni surfaces are analyzed with Time-of-Flight Secondary Ion Mass Spectrometry (TOF-SIMS) surface analysis method, which provides the chemical component information within 1-3 monolayer depth. Summary of the results obtained from this analysis are presented in Table 4.1, where some reference numerical results are provided along with verbal description. The numbers should be used to compare the density of individ-

ual species but not between different species. According to these results, the plasma oxidation method revealed contamination, because the oxidation is performed in a multi-user plasma chamber. The saline water oxidized surface exhibited very high Nickel Hydroxychloride and *Cl* contaminants, which are common electron traps in insulating oxides.

Species	Plasma oxidation	Saline water oxidation	DI water oxidation
nickel oxides ^a	Low(15)	High(33)	High(52)
nickel hydroxychloride ^b	Low(16)	High(74)	Low(10)
unwanted elements ^c	High(98.5)	Low(1)	Low(0.5)
perchlorates ^d	High(100)	None(0)	None(0)
chlorine	High(36)	High(56)	Low(8)

Table 4.1: Summary of the TOF-SIMS surface analysis results, where: **a:** Ni_2O , $NiOH$, NiO_2H , $Ni_2O_2H_2$, $Ni_2O_3H_2$; **b:** $NiOClH$; **c:** K , Ca , F ; **d:** ClO_3 , ClO_4

4.4 Fabrication Methods

ACMIM tunnel diode fabrication can be analyzed under two major groups: single step lithography and double step lithography.

4.4.1 Single Step Lithography

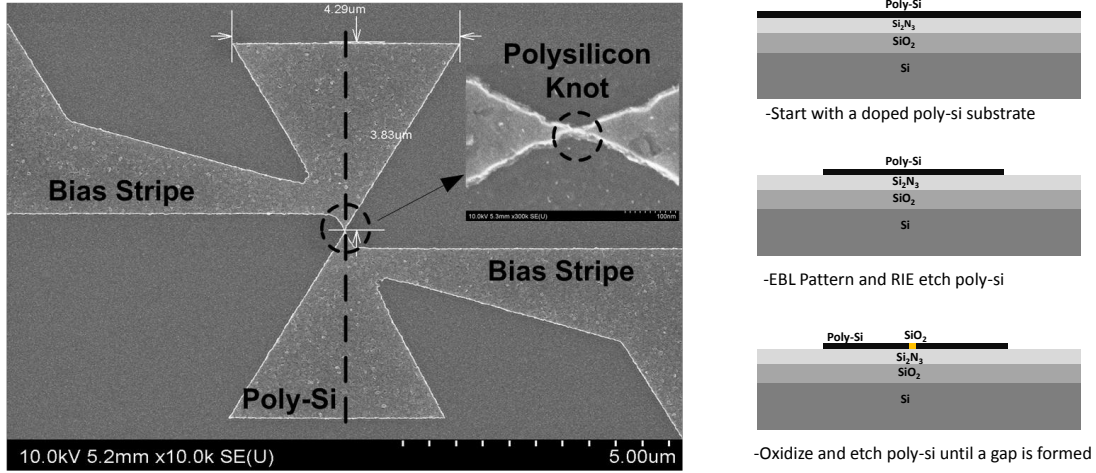
Initial attempts in process development of ACMIM tunnel junctions were in the direction of creating completely planar structures. There are three favorable outcomes of planar structures, where the tunnel barrier forms in the separation of the antenna arms. First, the tunneling occurs in the direction of the force exerted on the electrons by the coupled electric field. This enhances the rectification performance and lowers the junction resistance. Second, the junction area is extremely small, and so is the junction capacitance. Third, perfect planar structures open the path to mass-fabrication by stamping the pattern over large areas in a single lithography step.

Two major studies are carried out using different material combinations and process techniques for the fabrication of planar rectennas: Polysilicon/ SiO_2 /Polysilicon and Ni/NiO_x/Ni.

4.4.1.1 Polysilicon/ SiO_2 /Polysilicon Planar ACMIM Tunnel Diodes

The fabrication steps of Polysilicon/ SiO_2 /Polysilicon planar ACMIM tunnel diodes is shown in Figure 4.10 (b)[8]. Single step EBL with a negative resist (HSQ) is performed to pattern the device. Then, doped-polysilicon is etched through the patterned e-beam resist in a plasma dry etching chamber. Figure 4.10 (a) shows a micro-graph of Polysilicon/ SiO_2 /Polysilicon planar ACMIM tunnel diode.

In general, immediately after the process, the polysilicon devices have a thin bridge connecting the antenna arms, forming a conductive path. DI water oxidation



(a) Micro-graph

(b) Process flow

Figure 4.10: Polysilicon- SiO_2 -Polysilicon planar ACMIM tunnel diode [8]

and oxide etching in the buffered-oxide-etchant (BOE) solution is repeatedly performed until an oxide barrier at the neck of the antenna is created. In Figure 4.11, the left column illustrates the initial resistive behavior and the micro-graph of the conducting bridge. On the right column, the micro-graph after one step of oxidation and etching is shown and the non-linear I-V is presented underneath it. The oxide thickness at the shortest barrier location is estimated to be $1.38nm$ by fitting the nonlinear I-V curve to the well known tunneling equation derived by Simmons et al.[51].

Although this process created the first successful non-metal and completely planar ACMIM tunnel devices, the yield per substrate was extremely low because of the single device nature of the process. In addition, polysilicon does not provide a perfectly conductive medium and introduces various resistive loss mechanisms.

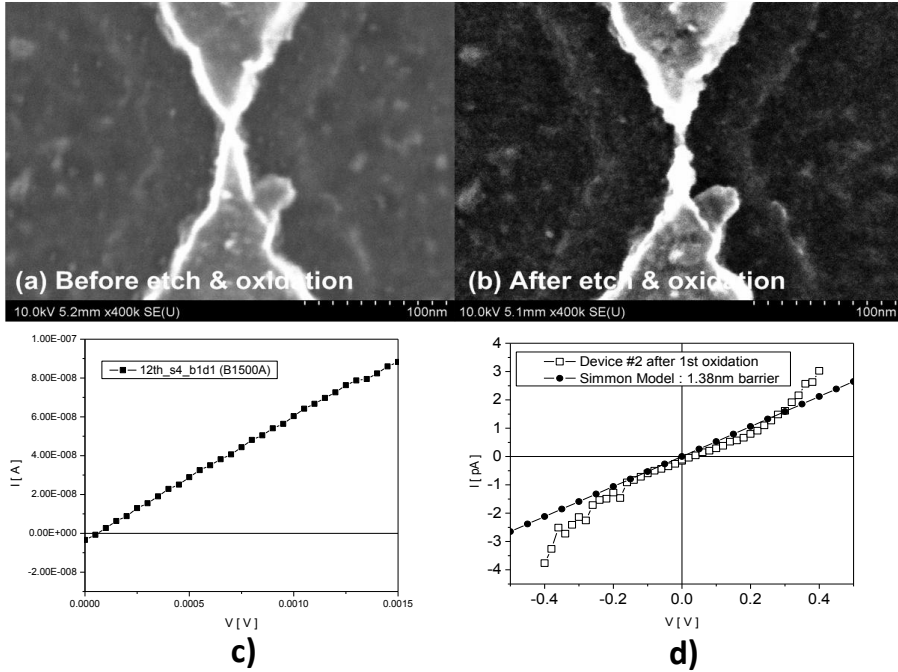


Figure 4.11: a) and b) Micro-graphs of the planar MIM before and after the oxidation/etch cycle; c) and d) resistive and nonlinear I-V curves [8].

4.4.1.2 Ni/NiO_x/Ni Planar ACMIM Tunnel Diodes

In an effort to eliminate the losses due to the relatively low conductivity of polysilicon, and to keep the advantages of planarity, Ni ACMIM tunnel diodes were produced with a process flow described in Figure 4.12. The fabrication of planar devices requires the patterning of a nano-size gap that will enable the tunneling of the electrons in between two conductor antenna parts. However, at this critical junction location, as described in Section 4.2.1, EBL proximity effect constrains nano-dimension gap accuracy.

Various methods are applied to overcome the major bridging problem. One of the best patterns generated after careful process manipulation is shown in Figure

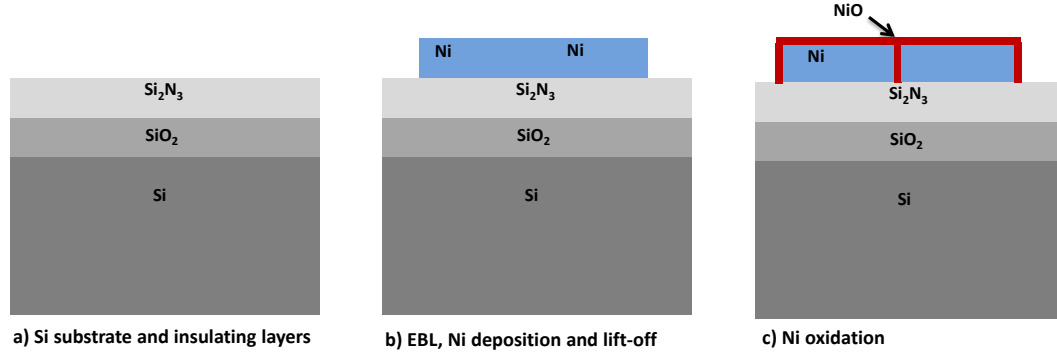


Figure 4.12: Single-step Ni-NiOx-Ni planar ACMIM tunnel diode lithography process.

4.13. Some of the customization methods can be listed as: 1) reduce the flare angle of the antenna to lower the interaction between the two patterns, 2) apply the highest available acceleration voltage ($30kV$) to decrease the short range scattering of the electrons in the resist at the expense of the long exposure time, and 3) modify the dose distribution by increasing the dose factor at the triangle tip by 1.5. These efforts can be considered manual dose modulation to eliminate proximity effects. A mild bridging still persists after dose modulation. However, the thin Ni bridge connecting the two electrodes is easily oxidized after the pattern is formed.

4.4.2 Double Step Lithography

Although the double step lithography increases the process steps, it eliminates the process challenges and allows for a well controlled lithography. In this approach, each electrode is created with independent lithography steps and the junction is formed at the overlap of two patterns. Thus, the yield is much higher than that of the planar structures. Double step lithography technique is still applicable to

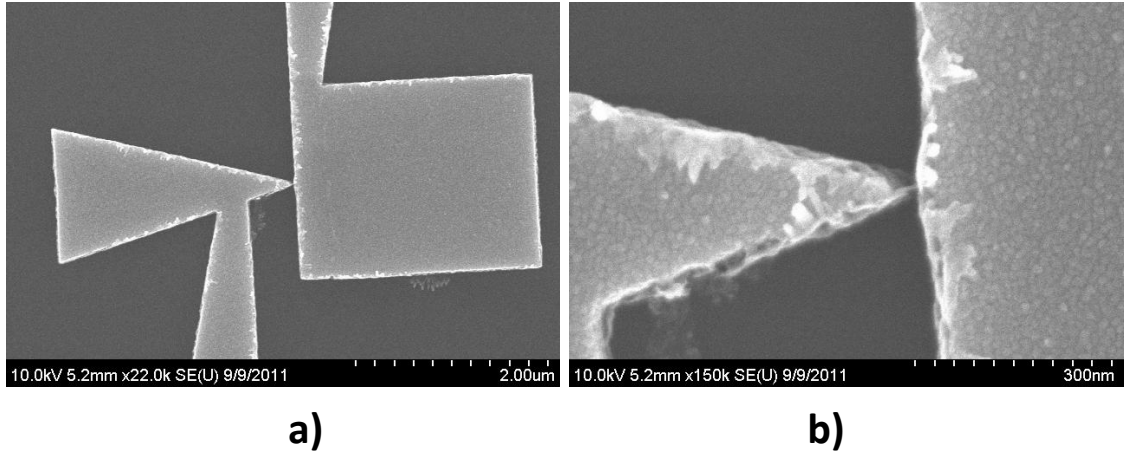


Figure 4.13: Ni/NiOx/Ni planar ACMIM tunnel diode fabricated by the single-step lithography process.

mass fabrication methods, such as nano-imprint, provided a critical alignment is performed in the second step. The design of the overlap devices allow for the lateral current flow in the direction of the coupled field, as in the planar diode case.

Since overlap ACMIM tunnel diodes are formed by double step lithography, the junction area has to be delicately controlled to minimize the parasitic capacitance. The solution methods developed to overcome this issue are discussed next.

4.4.2.1 Ni/NiOx/Ni ACMIM Tunnel Diodes

Ni/NiOx/Ni ACMIM tunnel diodes fabricated by the double step lithography process are the optimum devices developed for IR detection/harvesting purposes. This particular material and process combination produced the highest process yield, optimum electrical properties, and controllable process parameters. The details of this process are given in Figure 4.14. On the insulating substrate, the first EBL step is performed, Ni thin film is deposited and, using the standard lift-off process,

the first electrode patterning is completed. After careful alignment, the second EBL exposure is performed to pattern the second electrode. After the EBL exposure, along with the second electrode area, the tip of the first electrode is cleaned off the resist by the developer. At this point Ni is oxidized to form the insulating film of MIM junction. The second Ni film is deposited and the process is completed by removing the resist in acetone-solvent.

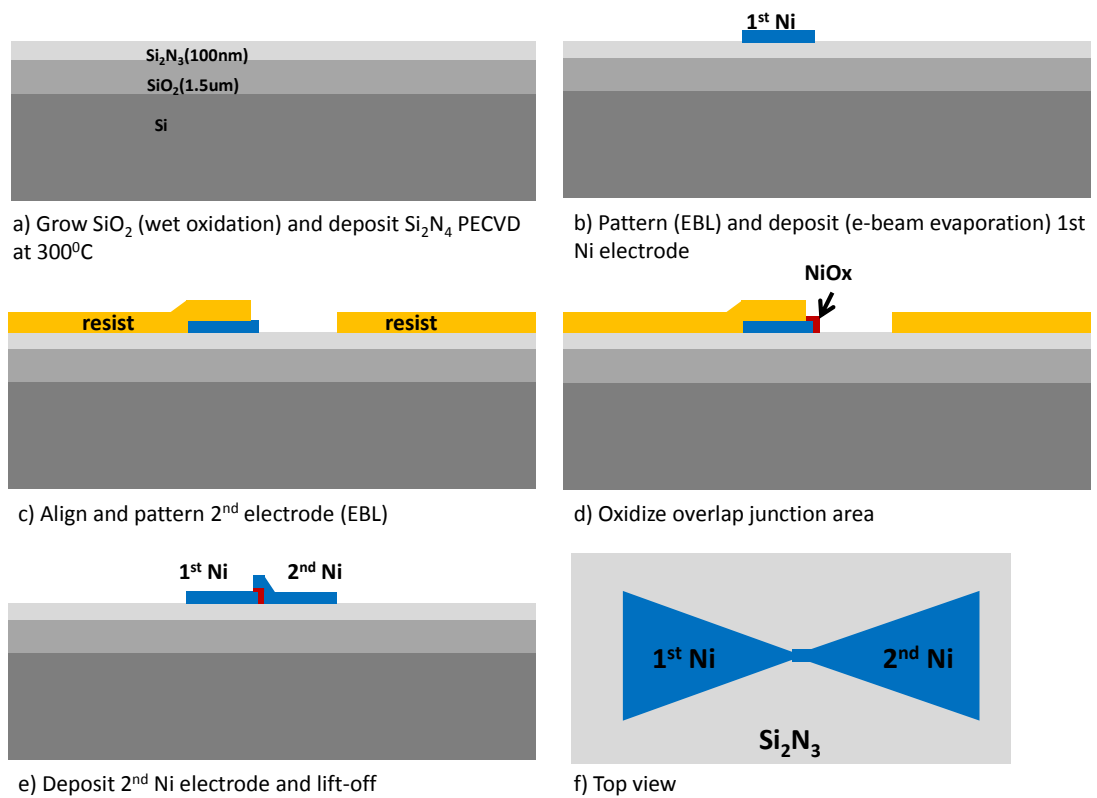


Figure 4.14: Double step lithography process steps.

In the double-step lithography process, the control of the overlap junction area is critical. As a result of the rigorous alignment methods described in Section 4.2.2 remarkably small junction areas are created, freeing the double-step lithography process from the parasitic capacitance burden. In Figures 4.15 and 4.16, micro-

graphs of some of the fabricated devices are shown. The results are given in two different geometries. In Figure 4.15, the second electrode has a rectangular end and, in Figure 4.16 the second electrode is identical to the first one, but asymmetry is still conserved because of the overlap. With this process approach, strict control over the junction area is achieved.

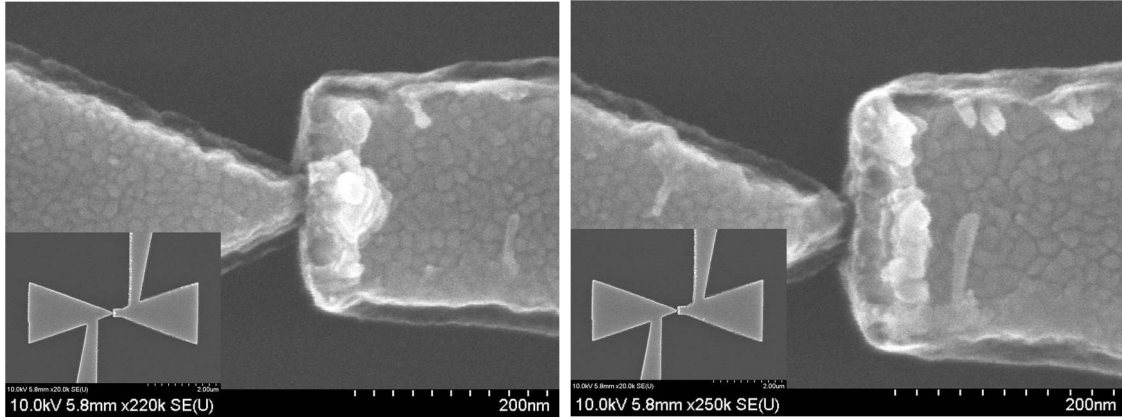


Figure 4.15: SEM micro-graphs of Ni/NiOx/Ni overlap ACMIM tunnel diode with extremely small overlap areas.

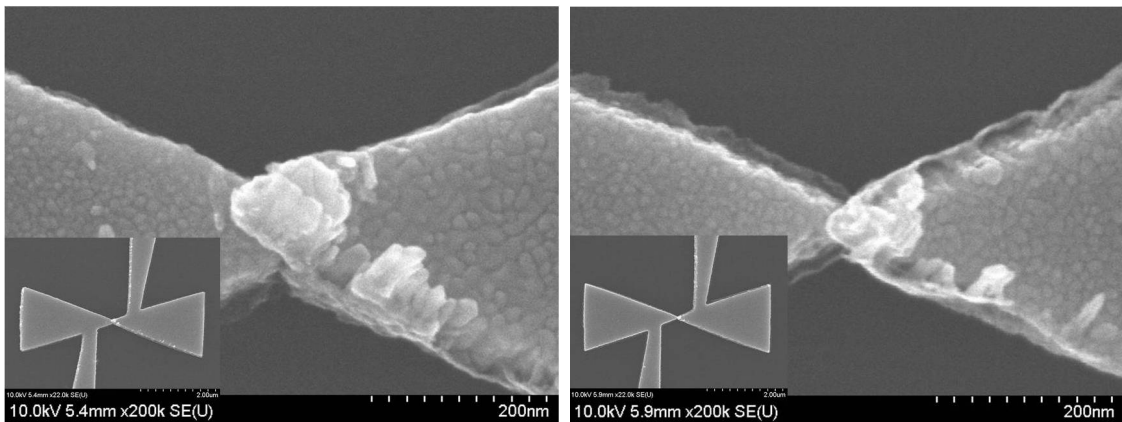


Figure 4.16: SEM micro-graphs of Ni/NiOx/Ni overlap ACMIM tunnel diode with extremely small overlap areas.

Throughout the design and fabrication development of ACMIM tunnel diodes,

major criterion is the applicability of the developed fabrication process over large areas for mass production. The parasitic capacitance problem is solved in the double-step lithography process with the help of a critical alignment process. However, subject to the mass fabrication techniques, the demand of critical alignment might not be realistic. Thus, the standard double-step lithography Ni/NiOx/Ni process is slightly modified to eliminate the meticulous alignment requirement. This adapted process is called “Strain Assisted Self Lift-off Process” and its details are given in Figure 4.17. The main aspect of this process is to introduce strain on the second electrode Ni film at the sharp step of the junction by increasing the difference in film thickness. In other words, when the metal film thickness of the first electrode is similar or higher than the second Ni electrode, the top overlap part detaches and the junction area is constrained to the side walls of the electrodes. In addition, to provoke the strain-assisted deformation and provide a better coverage at the junction side walls, the deposition of the second Ni film is done at a slight angle. Angled deposition enhances the adhesion of the second Ni on the oxidized surface of the first electrode and improves the process yield.

SEM micro-graphs of ACMIMs fabricated by the strain assisted self lift-off process are shown in Figure 4.18. In this particular device, the first and the second electrode film thicknesses are approximately $60nm$ and $40nm$, respectively. In Figure 4.18 (a) the micro-graph of the intermediate detaching phase is shown. The junction area in the device shown in Figure 4.18 b is limited by the side walls and it can be estimated as $0.004\mu m^2$ by multiplying the junction periphery ($200nm$) and the average contact height ($20nm$). This is a typical area measured in the devices created

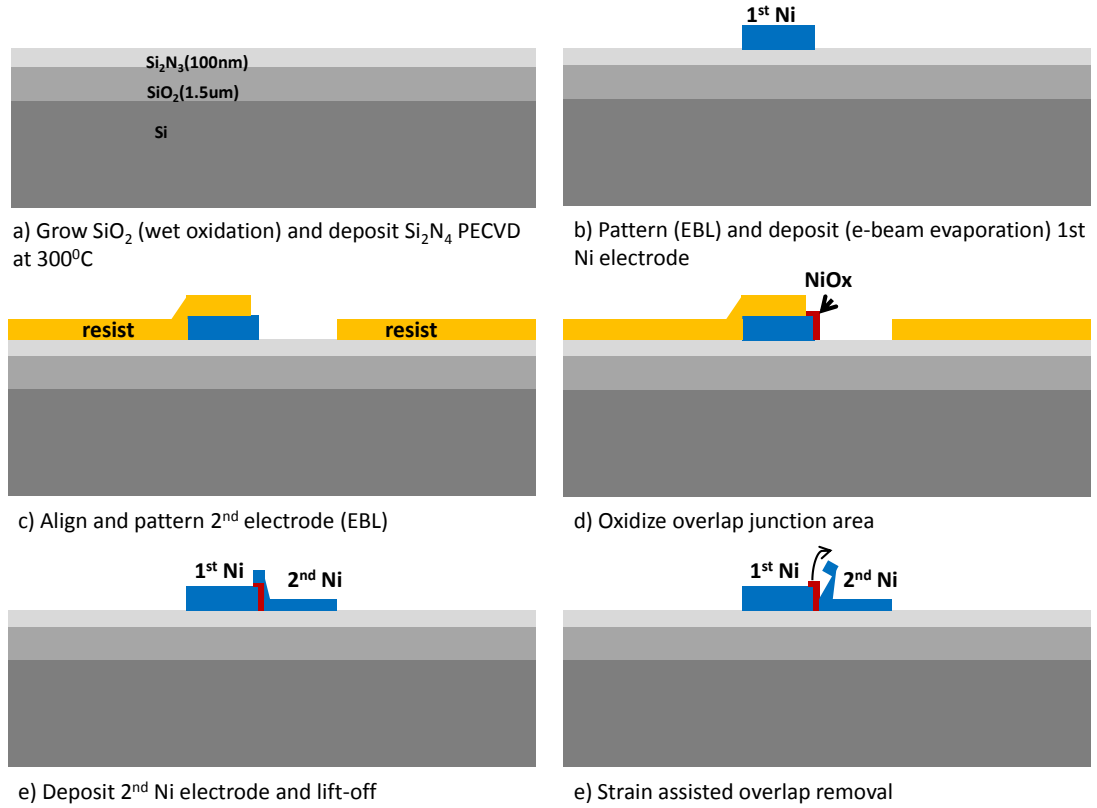


Figure 4.17: Strain assisted self lift-off process steps.

by the self lift-off process. Moreover, the junction area in the strain assisted self lift-off process can be controlled by varying the metal thickness of the electrodes. In Figure 4.19 the junction area is limited to the height of the first Ni layer (100nm), which is much higher than the second layer thickness (50nm) and the junction area can also be estimated as $0.01\mu\text{m}^2$.

4.5 Packaging

ACMIM tunnel diodes are extremely Electrostatic Discharge (ESD) and temperature sensitive, and fragile due to their ultra-thin tunnel barrier. Thus, packag-

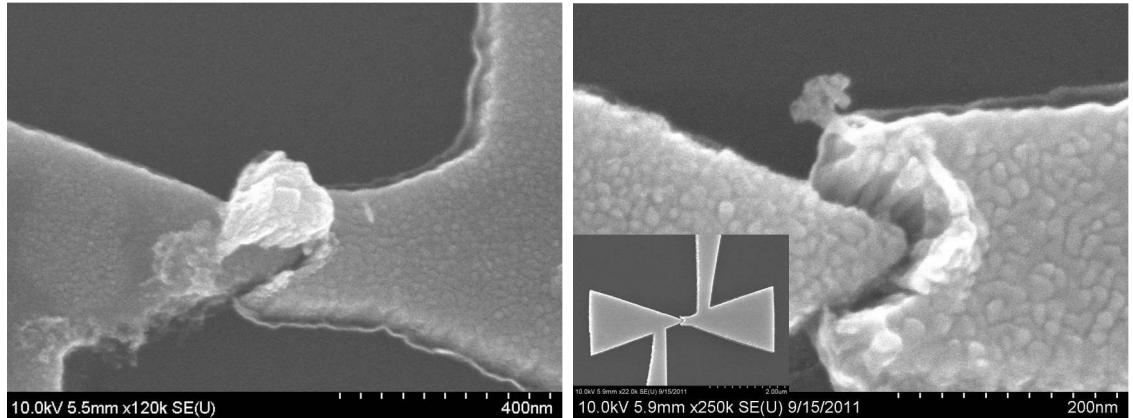


Figure 4.18: Strain assisted self lift-off planar ACMIM tunnel diode micro-graphs:
 a) intermediate detaching phase b) after the overlap piece detaches.

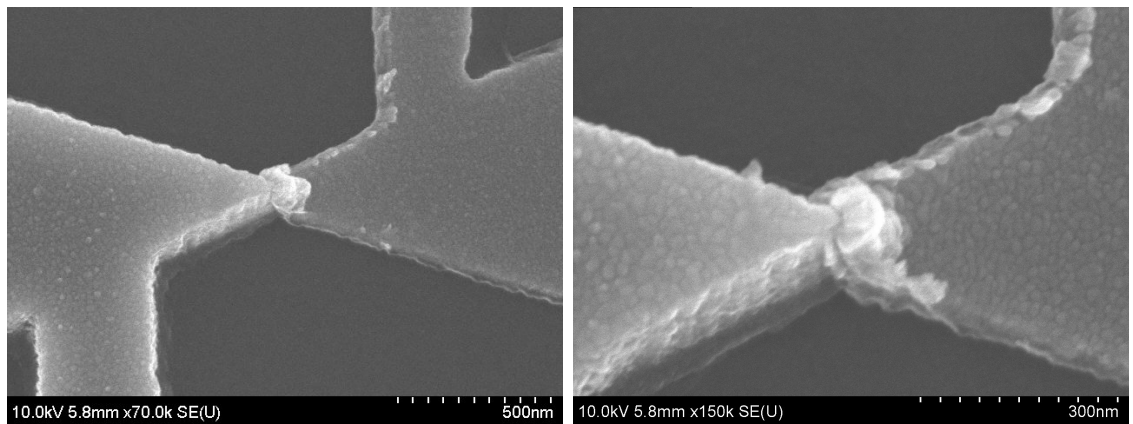


Figure 4.19: Strain assisted self lift-off planar ACMIM tunnel diode micro-graphs:
 Metal film thickness controlled junction area.

ing is the most challenging part of the fabrication. Particularly, packaging involves metal contact/lead patterning, and wire bonding.

Two different methods are developed to build the metal contacts/leads that are necessary to bring the signal from $600nm^2$ EBL patterned contacts to the 10^4um^2 wire bonding contacts. In the first method, Al is used as the metal lead/contact because it is a low-cost material and it is compatible with the standard wire bonding

process. Al is patterned and deposited (using standard lift-off process), after the ACMIM tunnel diode fabrication is completed. The Al post-processing method, summarized in Figure 4.20, provides low resistance ohmic contact. However, on average, the process yield decreases after this post-metalization process and wire bonding. In spite of very careful handling and ESD precautions taken during the photolithography and wire bonding processes, the yield problem persists. A single cell of EBL patterned ACMIM tunnel diode together with the align marks and the contact pads are shown with and without Al leads in figure 4.21 (b) and (a), respectively.

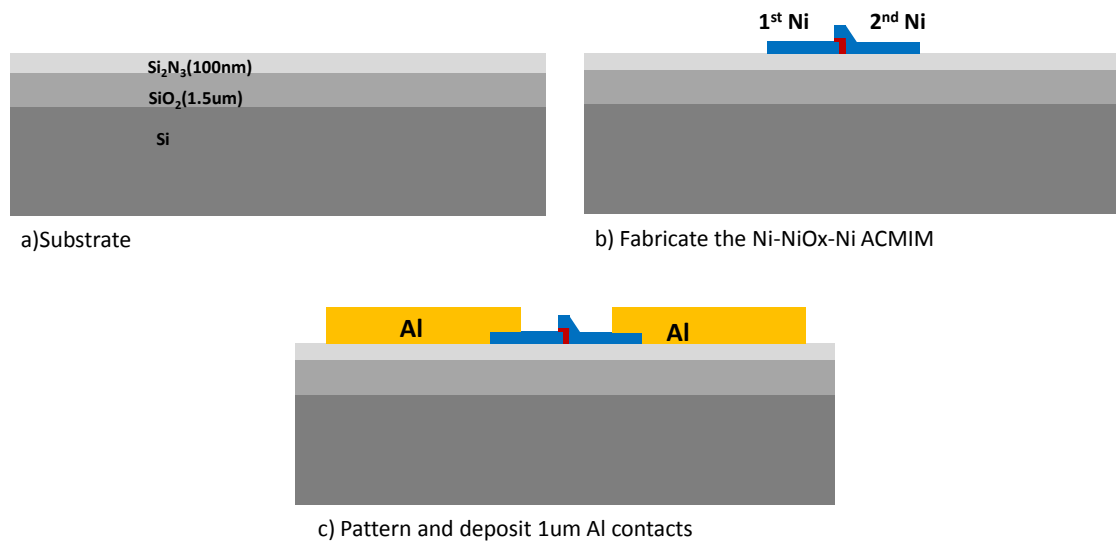


Figure 4.20: Al contact/ leads post-process patterning

The second metal contact/lead deposition process sequence developed is shown in Figure 4.22. In this process, the leads/contacts are pre-processed before the devices are fabricated. First, a thin Cr/Au (10nm/50nm) layer is deposited using a sputtering tool. Since 50nm is not sufficient for the wire bonding process, the contact

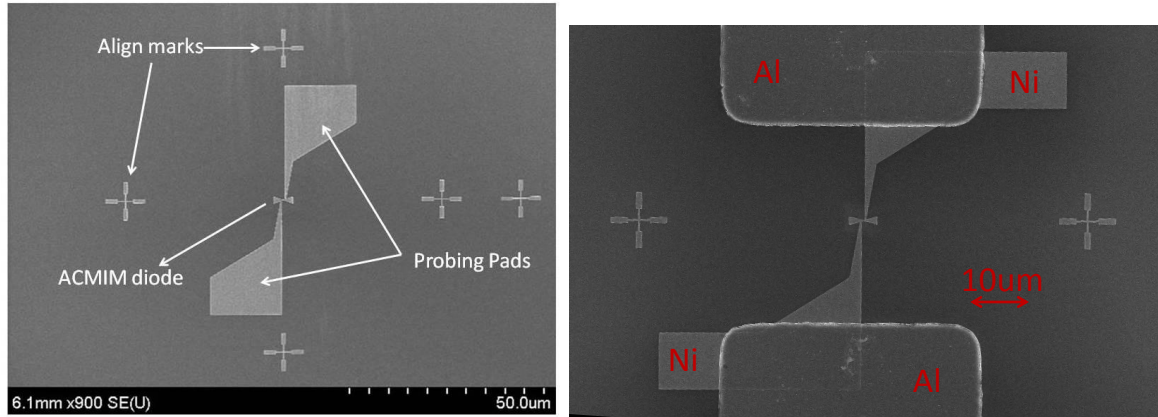


Figure 4.21: A single cell of EBL patterned ACMIM tunnel diode, align marks and contact pads without (left) and with (right) Al leads

areas are selectively thickened up to $1\mu\text{m}$ by electro-less Au plating method. It is followed by patterning the leads with photolithography and Au/Cr wet etching step. The pre-patterned contact/lead wafer is shown in Figure 4.23. This method -being a pre-patterning process- promises a higher yield as the ACMIM tunnel diodes are fabricated the last. However, due to adhesion problem between Ni and Au, this method is not applicable to our process.

Once the metal leads/contacts are processed, the sample die is mounted on a 44-pin LCC chip carrier package and the devices are wire-bonded to the pads on the carrier (see Figure 4.24). The chip carrier is then mounted in a socket that sits on a PCB board. From the PCB board connections to the measuring tools are done using SMA connectors. Also, in Figure 4.25, the SEM micro-graphs of two wire bonding types (wedge and ball) are illustrated.

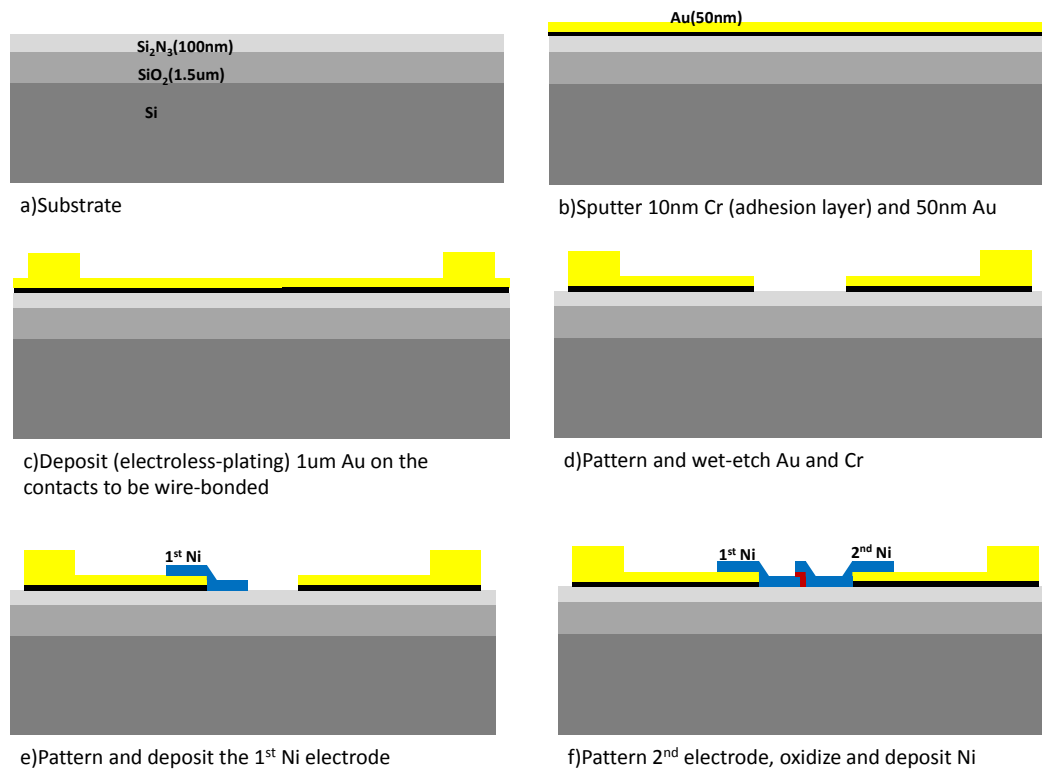
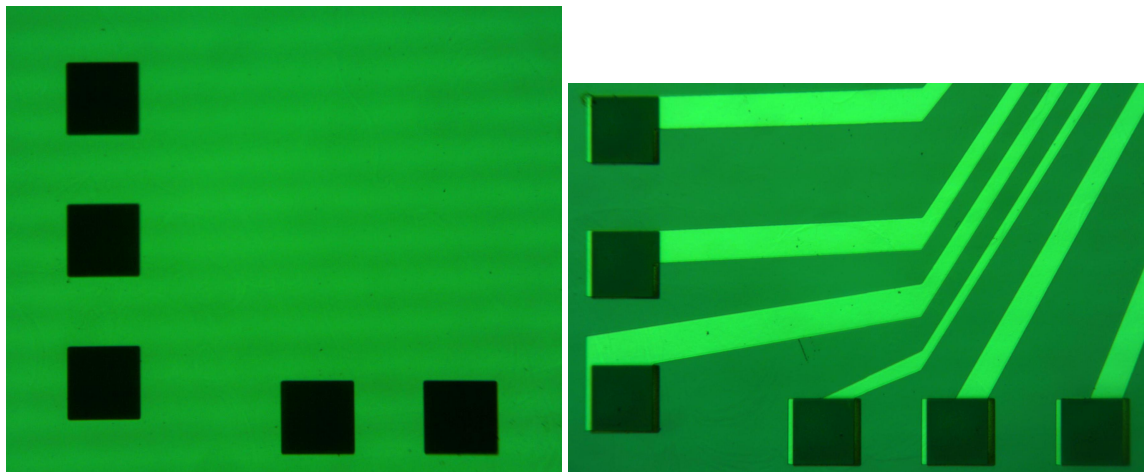


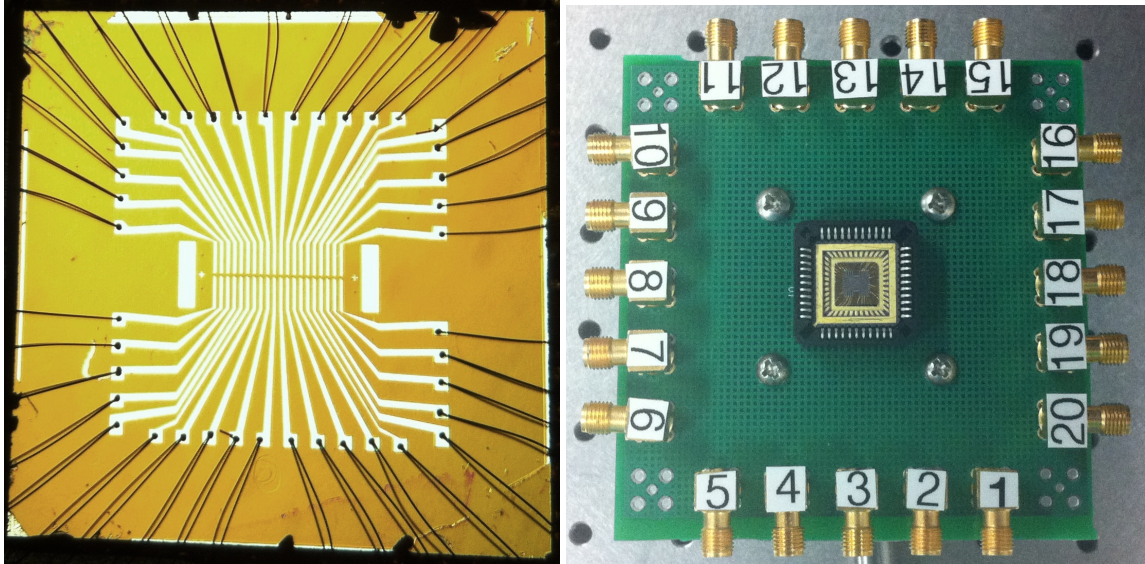
Figure 4.22: Au contact/ leads pre-patterning process



(a) After electro-less Au plating the contacts

(b) After etching Au/Cr leads

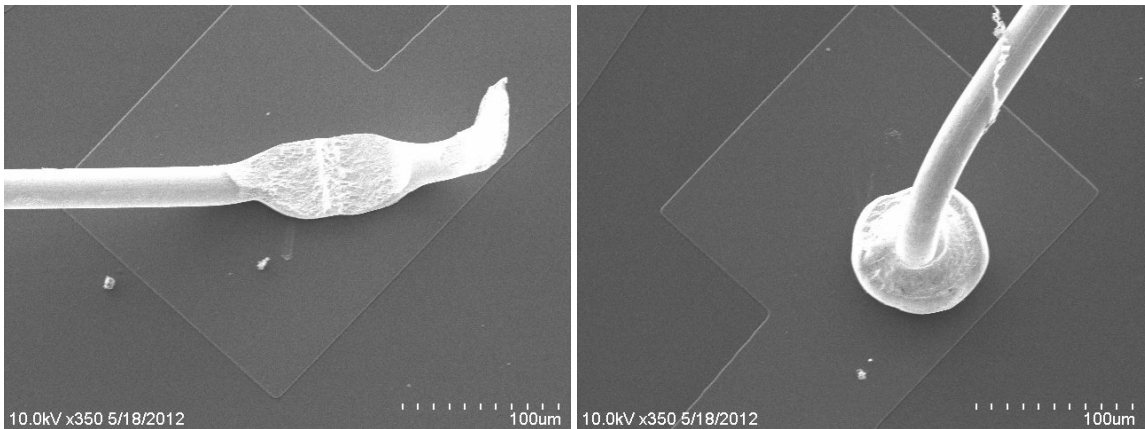
Figure 4.23: Au contact pre-patterning pictures



(a) Wire-bonded sample die

(b) Chip carrier mounted in a socket on a PCB

Figure 4.24: Packaging: wire-bonding and mounting on the PCB board.



(a) Wedge bond

(b) Ball bond

Figure 4.25: Wire-bonding types used in packaging.

4.6 Summary

- The optimum substrate ($\text{Si} + \text{SiO}_2(1.5\mu\text{m}) + \text{Si}_3\text{N}_4(100\text{nm})$) is designed considering the device operation needs and fabrication challenges.

- Details of the EBL are listed.
- EBL-PEC implementation results on the planar ACMIM diodes are presented.
- PEC adapted dose modulation method and alignment techniques are explained.
- Material selection for ACMIM diodes is reasoned and the methods used to form NiOx are described.
- Both the single-step and double-step fabrication methods are detailed.
- Packaging methods are specified.

Chapter 5

Experimental Results

In this chapter ACMIM diodes are characterized by time-independent electrical measurements and time-dependent radiation response measurements. The DC electrical parameters that qualify the IR detection performance are evaluated for a single device and for large groups to achieve a statistical data base. We used this approach to compare different fabrication methods. Yield graphics of different fabrication methods will be compared. Lastly, the effect of voltage bias, incident power, and polarization dependence on the IR response will be presented.

5.1 DC Current-Voltage Analysis

Once ACMIM tunnel diode fabrication is completed, devices are electrically characterized based on their current-voltage (I-V) relation. A parameter analyzer (HP 4156B) is used for the I-V measurements by applying a voltage sweep across the terminals of the device via tungsten needles of a probe station. Proper handling of the wafer is extremely important at this stage in order to avoid ESD damage. The voltage sweep is run typically between $-200mV$ and $200mV$. Characteristic MIM nonlinear I-V curves are obtained on a standard basis (see a sample MIM I-V in Figure 5.1). A device is considered to have “failed” when a linear I-V relation with a very low resistance ($\leq 100\Omega$) is obtained; or when very low noise-level (femto-amp)

current with drastically high resistance ($\geq 1 \times 10^9 \Omega$) is obtained in the bias range of interest. The MIM junctions fail if the barrier breaks down and exhibits pure ohmic conductivity. Furthermore, if the barrier is too wide and the turn-on voltage is too high ($\geq 0.5V$) this is counted as a failure. The voltage sweep is repeated at least three times and the DUT is considered “successful” only if the same I-V curve is consistently observed. This approach tests the device-strength. Device failure is rarely observed during measurements. Figure 5.2 shows an I-V curve where current jumps from $0.01mA$ to $0.11mA$ at $65mV$ bias point and loses its nonlinearity. This can be explained by the breakdown of the insulating layer and the junction starting to conduct resistively through its weakest point.

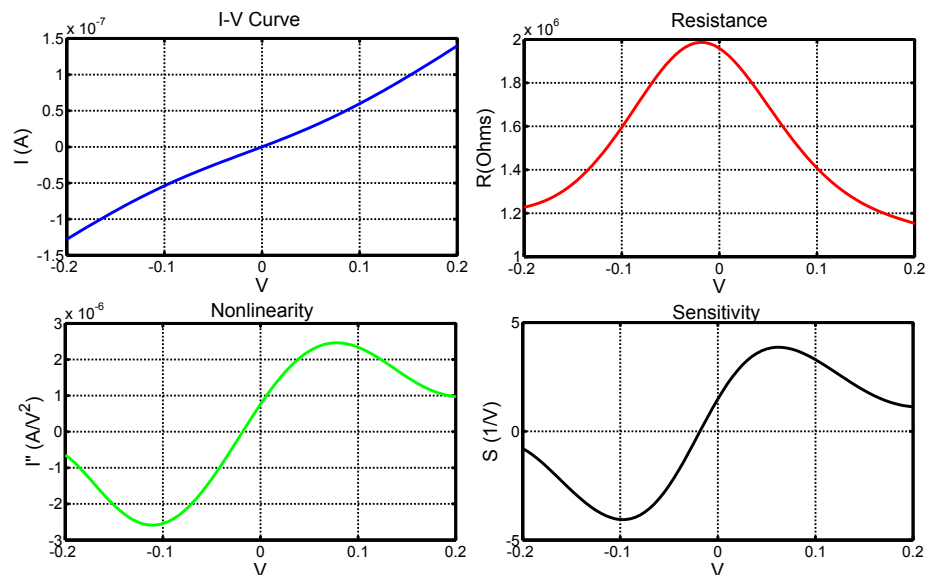


Figure 5.1: Current-Voltage curve analysis. I-V curve (Top-Left). Differential resistance (R-V) curve (Top-Right). Nonlinearity (I'' -V) curve (Bottom-Left). Sensitivity ($R \cdot I''$) curve (Bottom-Right).

Figure 5.1 shows a typical DC analysis performed on the I-V data. Based on

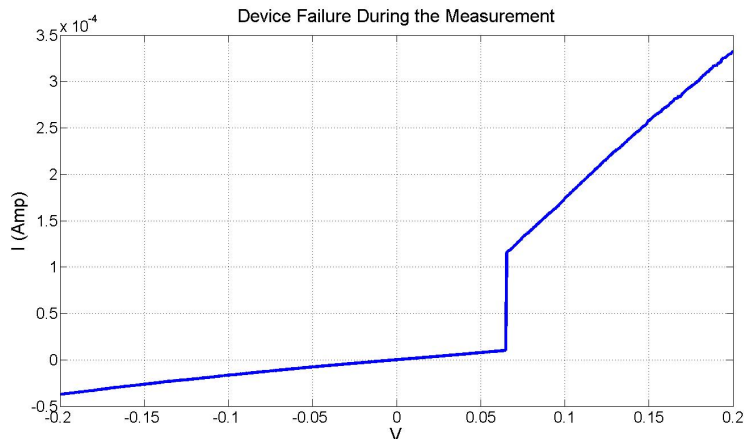


Figure 5.2: Device failure during the DC characterization.

the concept that the ability of an ACMIM tunnel diode to act as a detector depends on (i) small signal resistance, (ii) I-V nonlinearity, and (iii) sensitivity. We work to “tweak” these three parameters individually. The measured I-V data is fitted to high degree polynomials and then the zero-bias resistance ($R_0 = \frac{1}{dI_{DC}/dV_{DC}}$ at $V_{DC} = 0$), nonlinearity ($I'' = d^2I_{DC}/dV_{DC}^2$) and the sensitivity ($S = \frac{d^2I_{DC}/dV_{DC}^2}{dI_{DC}/dV_{DC}}$) are evaluated. The device considered in Figure 5.1 has zero-bias resistance of $R_0 = 200k\Omega$, zero-bias nonlinearity of $I''_0 = 8 \times 10^{-7}A/V^2$, maximum nonlinearity of $I''_{max} = 2.5 \times 10^{-6}A/V^2$, zero-bias sensitivity of $S_0 = 1.5V^{-1}$, and maximum sensitivity of $S_{max} = 4V^{-1}$.

Device characterization is performed at three stages: 1) after the ACMIM diode is fabricated, 2) after the metal leads/contacts are patterned, and 3) after the wire-bonding and packaging is completed. Unless otherwise mentioned, all the DC I-V analysis is from the first characterization step. This allows for device evaluation, before any other process intervenes. Of course, all the IR radiation tests are done at the third stage after the packaging because of optical measurement requirements.

In the text below, I present data on two categories of ACMIM diodes: those fabricated either using single or two step lithography process. The fabrication details of these processes were given in Chapter 4. Next, I-V characterization results are discussed.

5.1.1 Single-Step Lithography ACMIM Diodes

The single-step lithography processes can be further divided into subgroups: PolySi-SiOx-PolySi and Ni-NiOx-Ni. The single-step lithography method will be evaluated only for a single definitive device from each group because it is not possible to produce planar devices with a high process yield. In Table 5.1, the device parameters of each method are listed. The PolySi-SiOx-PolySi devices show very high sensitivities both at the zero bias and the maximum sensitivity point, but their resistances are extremely high. Therefore, they are not good candidates for IR detection. On the other hand, Ni-NiOx-Ni devices have relatively low resistances ($\sim 200k\Omega$) and higher curvature at the zero bias compared to the polysilicon junctions. Although they offer an extremely small junction area, planar ACMIMs cannot be mass produced for IR detection/harvesting purposes, due to the nature of the single-step lithography method. A characteristic nonlinear and asymmetric I-V curve of a Ni/NiOx/Ni planar ACMIM tunnel diode is shown in Figure 5.3.

	Material Combination	R_0	I''_0	S_0	S_{max}
		Ω	A/V^2	$1/V$	$1/V$
Planar	PolySi-SiOx-PolySi [8]	$8 * 10^{10}$	$1.5 * 10^{-10}$	12.4	31
	Ni-NiOx-Ni	$2 * 10^5$	$1 * 10^{-5}$	2	2.9

Table 5.1: Planar (single-step lithography) devices parameter summary.

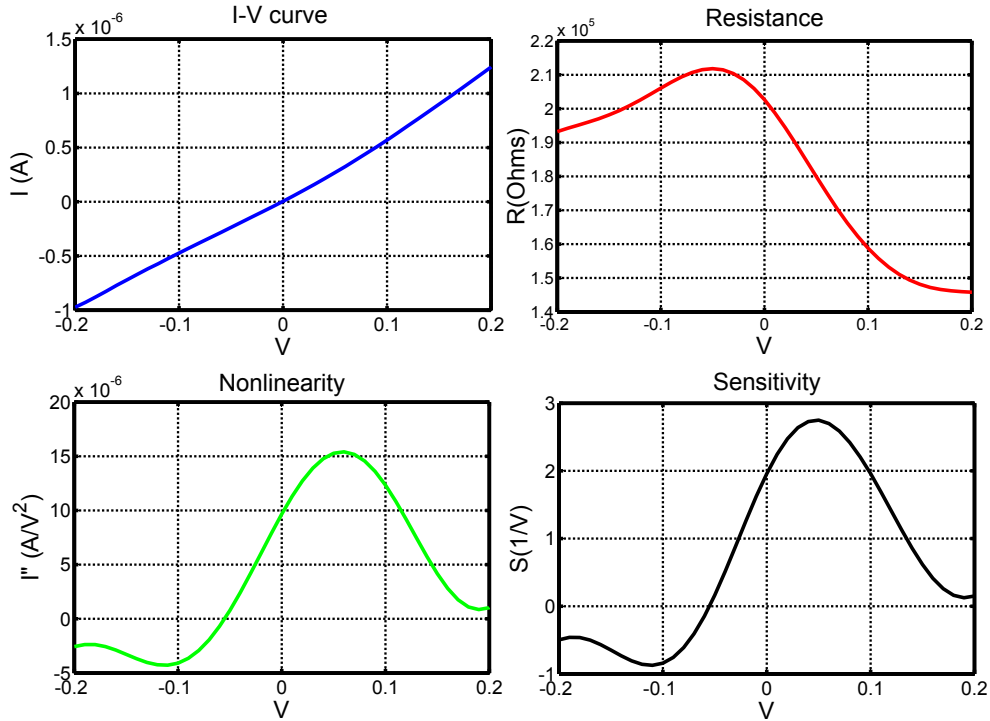


Figure 5.3: DC characteristics of Ni/NiOx/Ni planar ACMIM tunnel diode

5.1.2 Statistical Analysis on Double-Step Lithography Ni/NiOx/Ni ACMIM Diodes

The double-step lithography improves the process yield considerably, and it allows for a through statistical analysis to characterize different geometries and pro-

cess methods. Throughout the statistical analysis, the average values are calculated using the geometric averaging technique.

5.1.2.1 Junction Area Effects

Minimization of the junction area to decrease the parasitic capacitance has been one of the fundamental goals of this work. The small junction area requirement introduced the challenges of nano-fabrication to the ACMIM fabrication process, even though the minimum feature size of the whole pattern is not smaller than $200nm$ (the width of the antenna lead connecting to the antenna). In this section, the junction area effects on the junction resistance are explored.

Three different area groups with five devices in each group are fabricated on the same substrate to study the effects of area on the conductance in the MIM diodes. It is important to compare devices on the same die in order to minimize other experimental variations. In Figure 5.5, SEM micro-graphs of two MIM junctions from each group are presented. Each group is fabricated with $0.019\mu m^2$, $0.013\mu m^2$, $0.008\mu m^2$ nominal overlap areas. The average area of the fabricated devices are measured as $0.012\mu m^2$, $0.004\mu m^2$, $0.0004\mu m^2$, respectively. The differences are due to the process and alignment interference. The oxide barrier is formed here by two minute saline water oxidation at $100^{\circ}C$. The zero bias resistance (R_0) of each device together with group's geometric average (line) is shown in Figure 5.4. This particular analysis brings about two important facts about the MIM junctions: 1) MIM conductance is weakly area dependent, as the group averages scale up with

the area, 2) There are factors, other than area, that determine the conductance in the junction. For instance, in Figure 5.5, the junction shown in (e) with a sizable overlapping area has higher resistance ($30M\Omega$) than the junction in (f) ($200k\Omega$) whose conductance is limited to only the sidewall. This reverse analogy uncovers secondary dominant factors on the conductance of the MIM that may originate from the non-uniform insulating barrier, the nano-size apexes that locally enhance the field, the radius-of-curvature of the tip, and the metal film roughness.

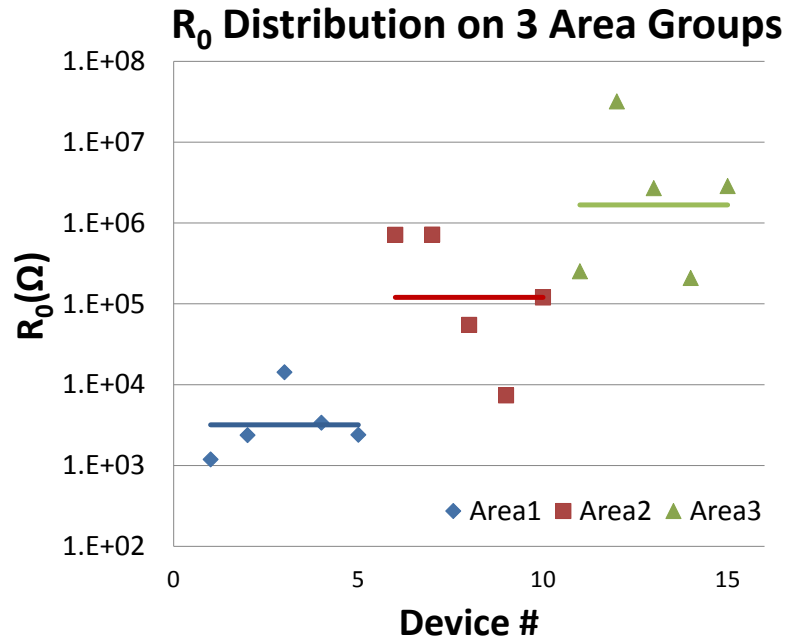
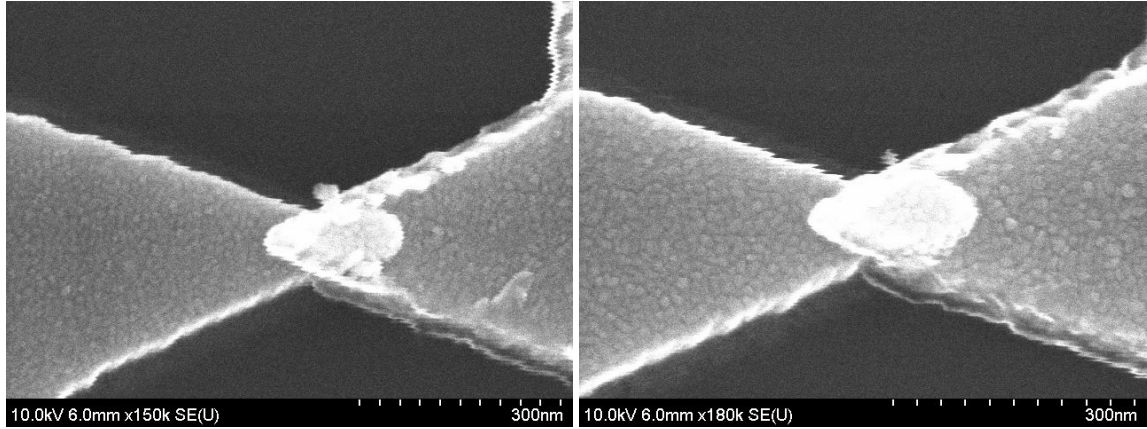


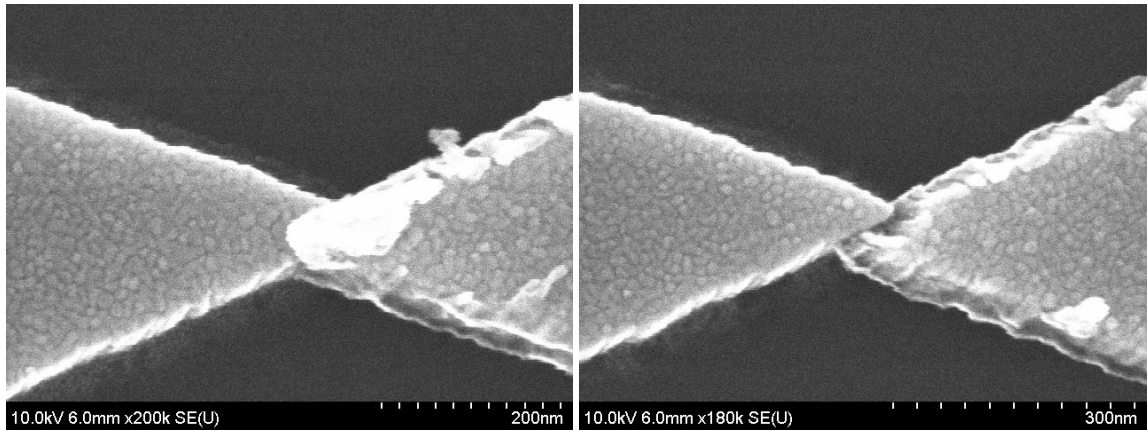
Figure 5.4: R_0 distribution of each area group. Lines represent the geometric average of R_0 in each group.

A new parameter called effective resistance, R^* is defined as in Equation 5.1. R^* allows for the performance comparison of MIM junctions by eliminating the junction area effect.



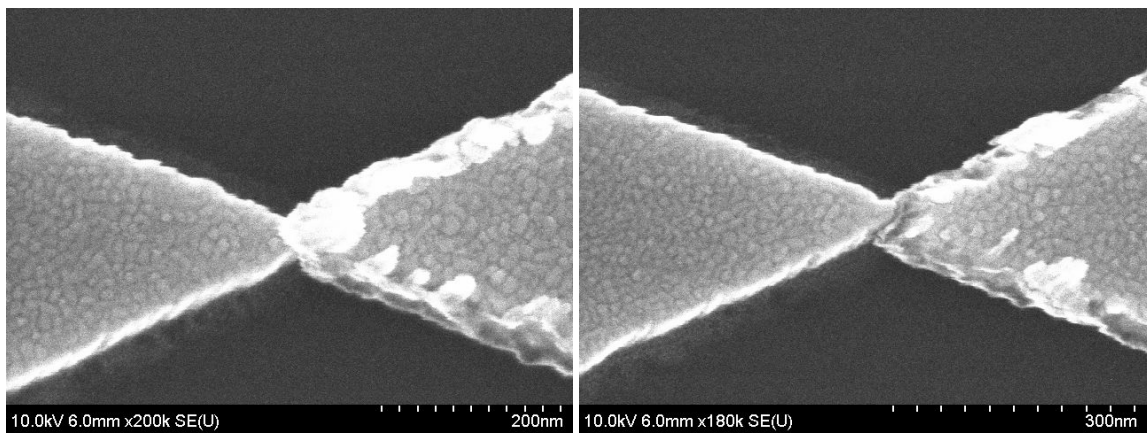
(a) Area1, $R_0 = 2.4k\Omega$

(b) Area1, $R_0 = 15k\Omega$



(c) Area2, $R_0 = 7.5k\Omega$

(d) Area2, $R_0 = 120k\Omega$



(e) Area3, $R_0 = 30M\Omega$

(f) Area3, $R_0 = 200k\Omega$

Figure 5.5: Micro-graphs of two devices from three area groups. Average Area1= $0.012\mu m^2$, Area2= $0.004\mu m^2$, and Area3= $0.0004\mu m^2$

$$R = \frac{dV}{dI} = \frac{dV}{d(A * J)} = \frac{dV}{A * dJ} \Rightarrow R^* = R * A = \frac{dV}{dJ} \quad (5.1)$$

A strong relation between the radius-of-curvature of the tip and the E-field enhancement is illustrated in Section 3. To understand the effects of geometry on the conduction performance of the MIM junctions, four different geometries are studied (see Figure 5.6): A) a single first electrode tip is covered by a second electrode, B) double first electrode tips are covered by a second electrode, C) a large rectangular first electrode is partially covered by a smaller second electrode, and D) a small rectangular first electrode is totally covered by a larger second electrode. The measured resistance of each device is multiplied by its junction area to eliminate the area effects and the geometric average of R^* parameter is calculated for 5 devices in each group. Ideally, the parameter R^* is expected to be similar in each group as the material and the oxidation method (1 minute saline water oxidation at $100^{\circ}C$) are the same. However, as shown in Figure 5.6, the average effective resistances of each group are very different from each other. The R^* value of the geometry B (with double tip) is 40% less than that of geometry A (with single tip). This proves the significance of the field-enhancing tip on the MIM conduction. Moreover, the only difference between the geometries C and D is that in D the smaller rectangle is covered by the large rectangle allowing the two corners to contribute to the conduction, whereas in C, the small rectangle is on the top with no tips or corners contributing to the conduction. As a result, the conduction in the geometry C is much less effective than the geometry D, with R^* 13 times larger. This study experimentally shows the

importance of the MIM junction geometry (especially the field-enhancing sharp tips and corners). This supports the claim that the MIM junction conduction cannot be evaluated only by its area, and that the junction resistance can be decoupled from its capacitance by introducing area independent resistance improvement methods.

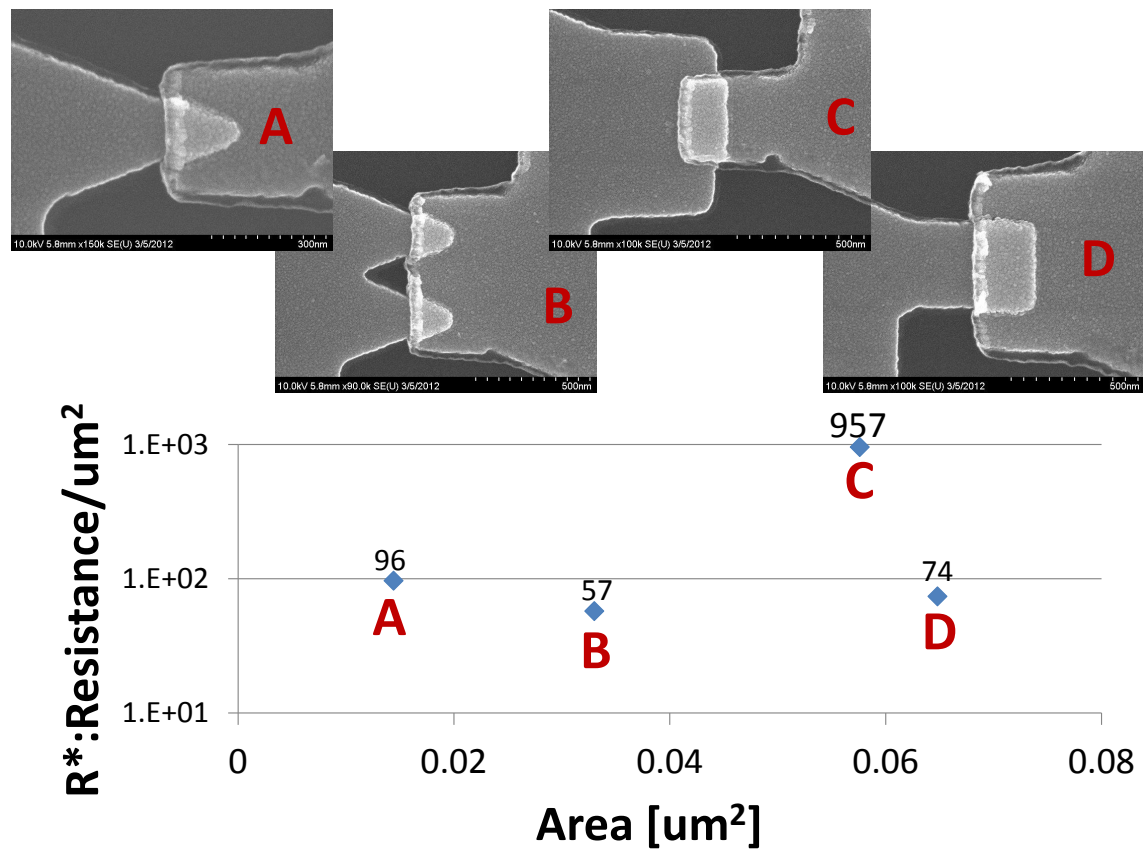


Figure 5.6: The micro-graphs of four different geometry MIM junctions. And the average R^* vs. area plot of each group

5.1.2.2 Oxidation Method Selection

The insulation layer between the metal antenna parts is the vital component that dominates the performance of the device. However, it is also the most intricate

to analyze. Three major oxidation methods are applied to create the NiOx barrier: 1) Saline water oxidation, 2) DI water oxidation, and 3) O_2 plasma oxidation. The goal is to form the thinnest (for low junction resistance) and the most rigid (for high device yield and stability) barrier. To characterize the NiOx barrier, process yield and the device parameters are evaluated for each of the oxidation methods. On average, twenty devices on a sample are inspected for each oxidation time.

The process yield within each oxidation method is analyzed with different oxidation times. The first and the second yield data are evaluated at the first measurement step after the ACMIM diode is fabricated (first yield) and the second measurement step after the patterning the metal leads/contacts (second yield), respectively.

In Figure 5.7, saline water oxidation yield results are presented. The first yield gradually increases with the oxidation time and it stabilizes around 90% for oxidation time ≥ 2 mins. However, these devices usually do not survive the metal lead/contact patterning process and the second yield profile is much worse than the first. Even at longer oxidation times (10 min), which creates a thicker oxide, the second yield does not increase above 40%. It was not possible to oxidize the Ni devices in saline water for longer times, because damage is observed on the Ni patterns after 10 mins of oxidation.

Similarly, the DI water oxidation data shown in Figure 5.8, exhibits an initial yield increasing with the oxidation time. In this experiment a prolonged oxidation of one hour is performed to create the thickest oxide possible so that the devices remain stable for the second measurement step. In an hour long oxidation, a decrease in

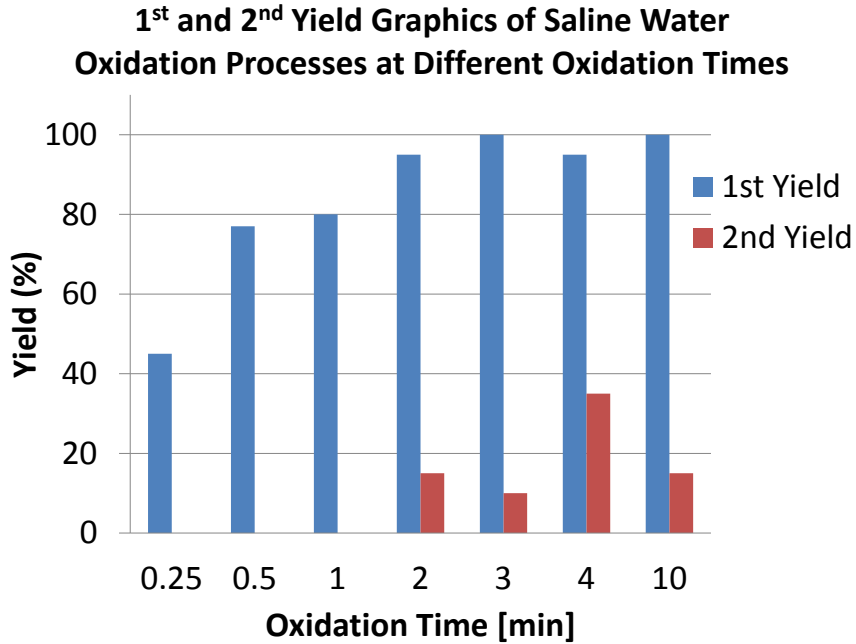


Figure 5.7: 1st and 2nd yield graphics of saline water oxidation process at different oxidation times.

the first yield is observed because DI water oxidation is performed at 100⁰C and the fluidic forces damage the nano-size Ni devices in the long term. However, a relatively high yield (60%) is obtained at the second step with one hour long DI water oxidation. The first measurement step indicated a high process yield (~ 90%) using wet oxidation methods (saline or DI water), the second process yield is not sufficient to package the samples and test for IR response for shorter oxidation times (≤ 10 mins). On the other hand, if oxidation time is extended to create thicker and more stable oxides, the fluidic forces in the boiling water appears to damage the devices, creating adhesion problems and decrease the yield.

Lastly, the O₂ plasma oxidation method is utilized to control the oxide layer without suffering the consequences of the fluidic damages. In this experiment, the

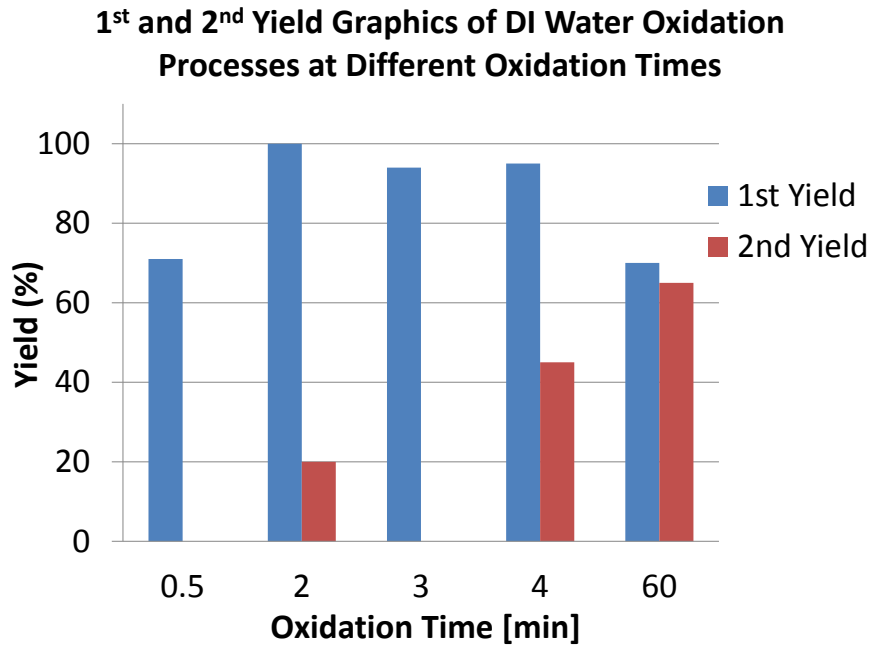


Figure 5.8: 1st and 2nd yield graphics of DI water oxidation process at different oxidation times.

oxidation time and the plasma power effects are examined and the results are presented in Figure 5.9. Initially, very high (100W) plasma power is applied at very short oxidation times (15s and 30s). The first yield results were very low ($\leq 40\%$) as a result of the very thick oxide, which pushed the device resistances to extremely high values ($\sim G\Omega$). The oxidation is also repeated at low plasma power (12W and 20W). The low-power plasma oxidation provides high yield in the first and second measurement steps. With this analysis, O_2 oxidation is determined to be optimum for our purposes.

In addition to the yield analysis, the oxidation methods are evaluated from the device parameter standpoint. The average device parameters of four individual samples with twenty identical devices on each are presented under the three men-

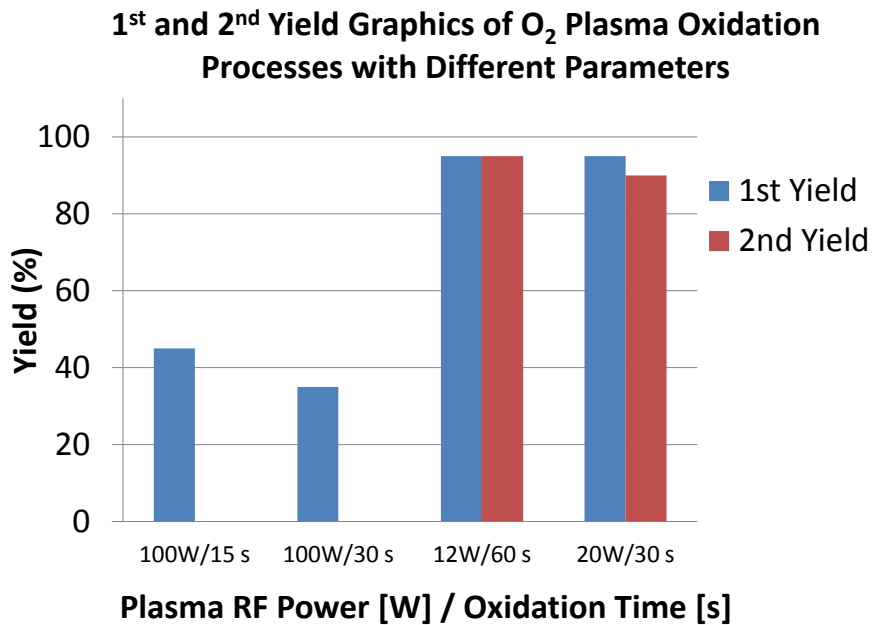


Figure 5.9: 1st and 2nd yield graphics of O₂ plasma oxidation process with different parameters.

tioned oxidation methods in Table 5.2. The principal quantity that dominates the device performance is the resistance at zero-bias (R_0). The data summarized in the table shows that the desired low R_0 values ($k\Omega$ range) are possible with wet-oxidation methods at short oxidation times. However, the insulation layer is not stable enough, these devices have very low yield and cannot be considered as good candidates for mass production. On the other hand, the extended wet oxidation times not only caused damage and reduced the yield, but also their R_0 is too high to satisfy the IR detection requirement. Among the oxidation methods considered, the plasma oxidation method at lower plasma power resulted in the optimum process yield and the device parameters. With this method, not only the R_0 is kept within the suitable range ($k\Omega$), but also durable devices are created.

Oxidation		R_0	I''_{max}	S_{max}	I''_0	S_0
Method		$k\Omega$	$[A/V^2]$	$[1/V]$	$[A/V^2]$	$[1/V]$
Saline Water Oxidation	0.5 min	9.7	7.2×10^{-4}	3.8	1.7×10^{-5}	0.17
	2 min	9.6	5.6×10^{-4}	3.4	2×10^{-5}	0.19
	4 min	30	2×10^{-4}	3.8	5.9×10^{-6}	0.18
	10 min	858	1.3×10^{-5}	5	3×10^{-7}	0.26
DI Water Oxidation	0.5 min	23	4.8×10^{-4}	5.9	1.6×10^{-5}	0.37
	2 min	500	2.2×10^{-5}	4.7	5.8×10^{-7}	0.29
	4 min	97	7.5×10^{-5}	3.7	5.4×10^{-6}	0.39
	60 min	22×10^3	1.4×10^{-6}	7	2×10^{-8}	0.44
O_2 Plasma Oxidation	100W/ 0.25 min	164×10^3	7.2×10^{-8}	5.7	3.9×10^{-9}	0.64
	100W/ 0.5 min	91×10^3	1×10^{-7}	6	8.4×10^{-9}	0.76
	20W/ 0.5 min	93	8×10^{-5}	3.9	7×10^{-6}	0.53
	12.5W/ 1 min	116	5.5×10^{-5}	3.2	4.7×10^{-6}	0.55

Table 5.2: Average device parameter summary of the three oxidation methods.

In Figure 5.10, the maximum nonlinearity (I''_{max}), which is a measure of the rectification performance, is plotted as a function of R_0 . An inverse linear relationship exists between the R_0 and I''_{max} . This is expected because R_0 increases as the oxide barrier thickness increases and thicker barrier does not respond to the applied bias as much as a thinner barrier. In other words, when the tunneling barrier is thin even a small change in the bias changes the tunneling probability and the tunneling current leading to high nonlinearity. The optimum devices locate themselves on the top-left corner of the I''_{max} vs R_0 plot. However, as discussed above, these devices are not robust and have low process yield. As a result, the plasma oxidation results that have $k\Omega$ -range resistance and high yield are concluded to be ideal for the project goals.

5.1.2.3 Asymmetry Analysis

It is possible to encounter both very asymmetric (see Figure 5.11) and highly symmetric (see Figure 5.12) I-V curves. Also, from the zero-bias parameters such as zero-bias sensitivity (S_0) and nonlinearity (I''_0), which are summarized in Table 5.2, the asymmetry factor can be observed. However, due to the randomness in the asymmetry, no conclusive result has been reached.

5.1.2.4 Process Variation Analysis

The ACMIM diodes, although fabricated identically, do not consistently operate similarly. In Figure 5.13, the parameter R_0 of each device on two samples

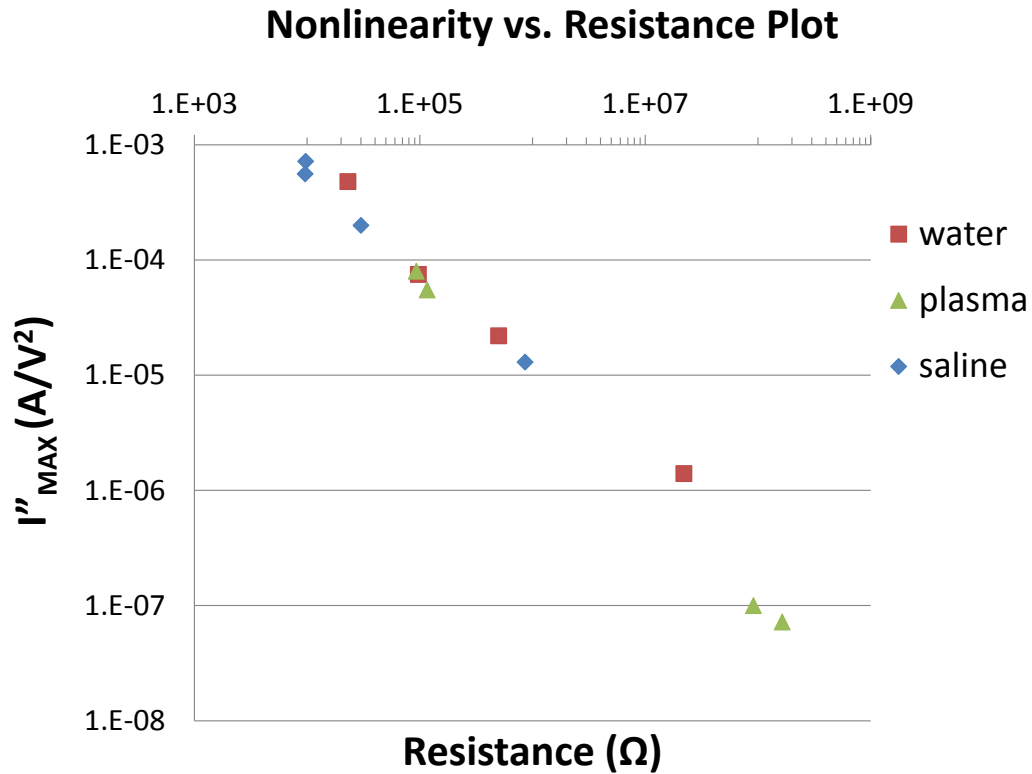


Figure 5.10: Nonlinearity as a function of the R_0 for different oxidation techniques.

(plasma oxidized for 1min and 30sec) are plotted before and after the lead/contact metalization step to emphasize the parameter variation. This parameter distribution plot shows that the 80% of the devices vary between 1×10^5 and $1 \times 10^6 \Omega$ range. Although the R_0 parameter consistently increases at different rates between the first and second measurements, the second yield is similar to the first yield.

To understand the parameter fluctuations and the randomness in the asymmetry better, an inspection of the junction is necessary. Hence, AFM surface analysis is performed on the oxidized Ni surface and the results are shown in Figure 5.14. Statistical RMS (root mean square) and average roughness parameters are mea-

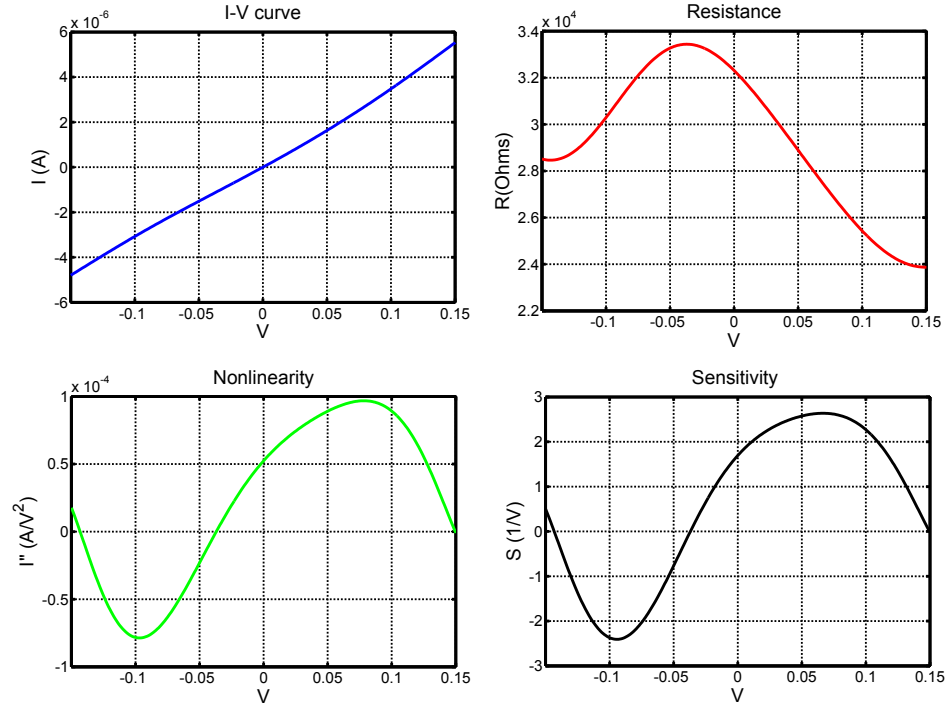


Figure 5.11: An example of an asymmetric I-V across zero-bias.

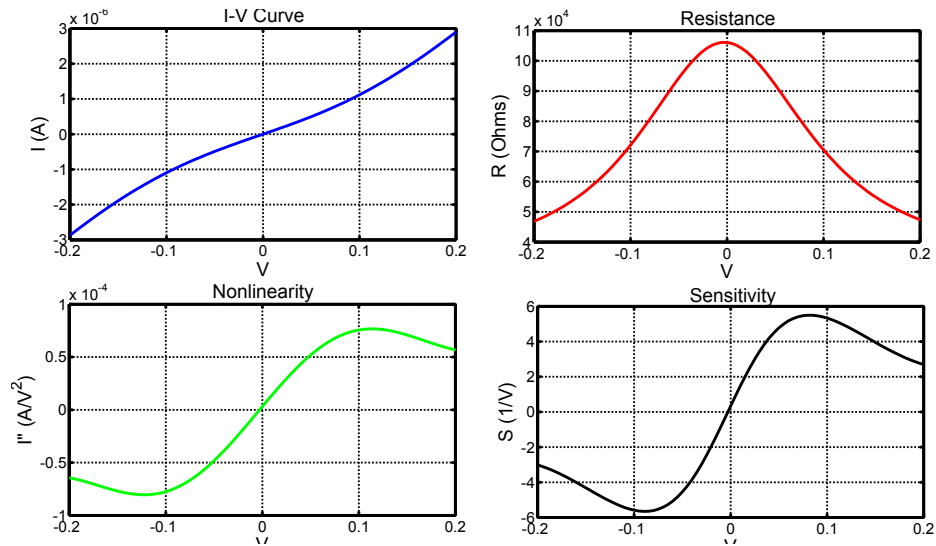


Figure 5.12: An example of a symmetric I-V across zero-bias.

sured as 1.071nm and 0.844nm , respectively. From both the 3-dimensional (left) and 2-dimensional (right) surface characteristics plots, spikes of nano-scale can be observed. These extremely sharp tips can further enhance the E-field and dominate

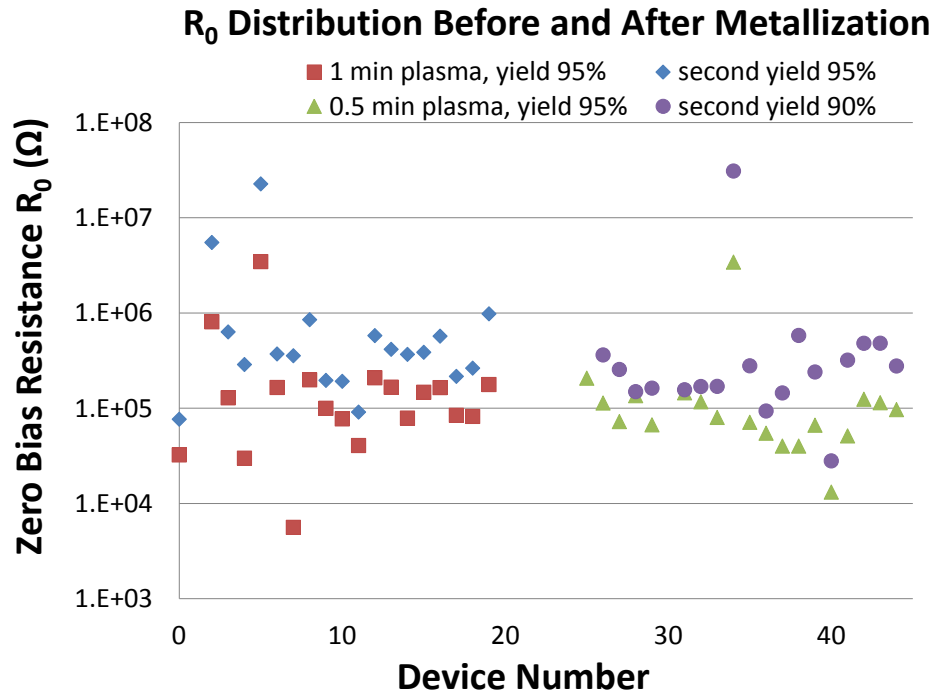


Figure 5.13: R_0 comparison of individual devices before and after metallization. The R_0 parameters belong to two different plasma oxidation processes.

the conduction at local regions. This can explain the parameter variations among the devices processed identically.

The inconsistent asymmetry occurrence can also be explained by the surface roughness. The local field enhancements created by the spikes can overshadow the geometric asymmetry. In Figure 5.15, the grain boundaries of the Ni film revealing the surface roughness can be observed. Thus, the parameter variation can be related to the secondary surface properties.

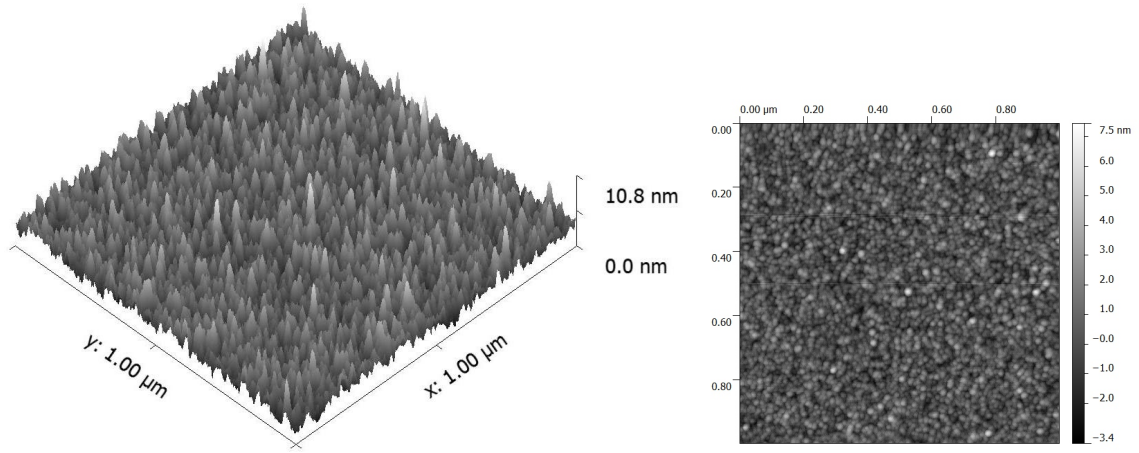


Figure 5.14: AFM surface analysis of an oxidized Ni thin film. A 3-D (left) and a 2-D (right) pictures.

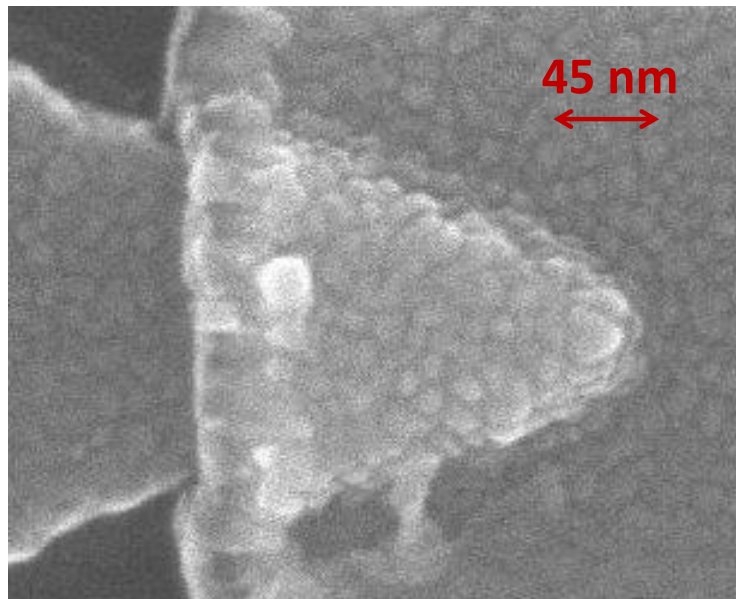


Figure 5.15: Higher resolution SEM micro-graph of the junction revealing the surface roughness effects.

5.1.2.5 Time Variation Analysis

After the first step device characterization, the process flow is followed by packaging to prepare the devices for IR testing. To investigate the shelf-life and the

device stability over time, samples are kept in the ambient and the I-V measurements are repeated on the first, third and sixth days after the fabrication. In figure 5.16, the zero-bias resistance parameter variation in time is illustrated. The average R_0 increases by 2.6 times between the first and the third days and only 1.2 times between the third and the sixth days but none of the devices are damaged in this period. This shows that after the fabrication is complete, variation in the oxide layer thickness continues. The increase in the resistance, which corresponds to the broadening of the barrier, is initially fast but decreases gradually.

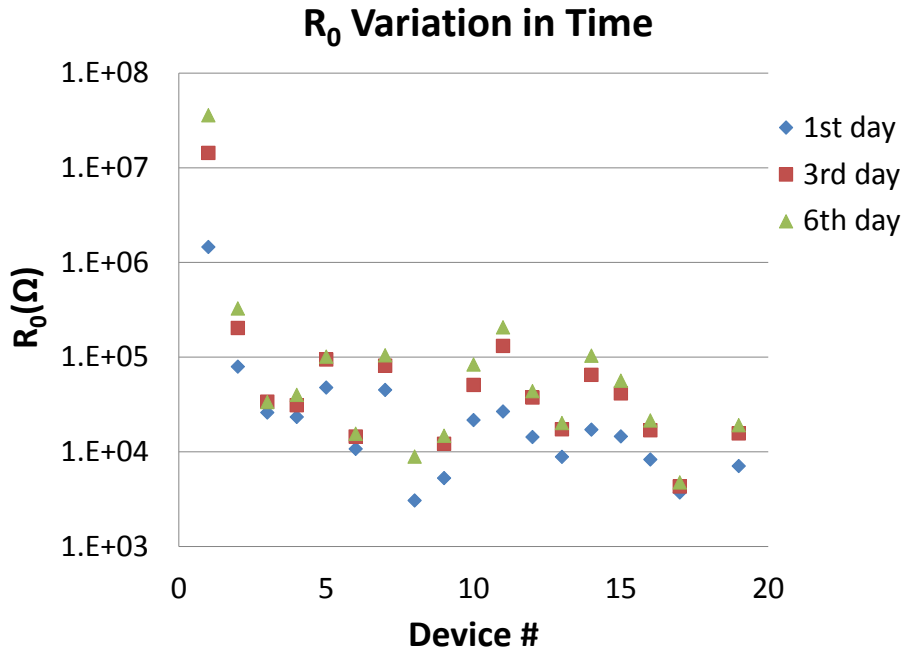


Figure 5.16: R_0 variation in time for each device on a sample.

5.2 RF Response

Initial radiation tests are performed at RF frequencies to characterize the rectification performance of the MIM diodes. Although the antenna part of the ACMIM

diode is not designed for RF frequencies, the incident RF is partially coupled across the MIM diode through the metal leads and probes. Rectification by the MIM tunnel diode at RF frequencies is shown with this experiment. In Figures 5.17 and 5.18, detection of 6 GHz and 20 GHz radiation as a function of applied voltage bias is presented, respectively. On these same plots, the rectified current is compared to the nonlinearity (I'') and, as expected, strong correspondence is observed.

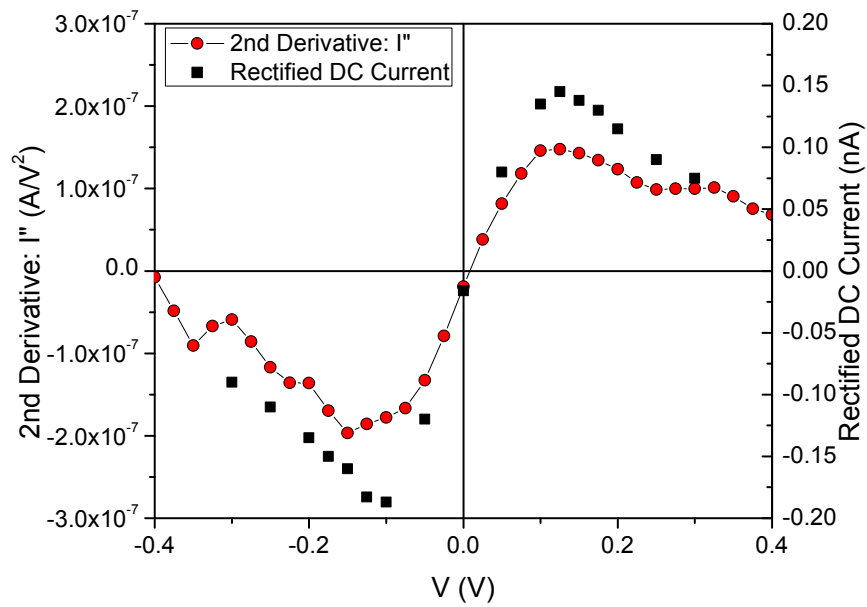


Figure 5.17: Applied bias vs. rectified current and nonlinearity curve at 6 GHz [9].

5.3 IR Response

The ACMIM tunnel diodes are tested and their response is characterized at 30THz IR radiation.

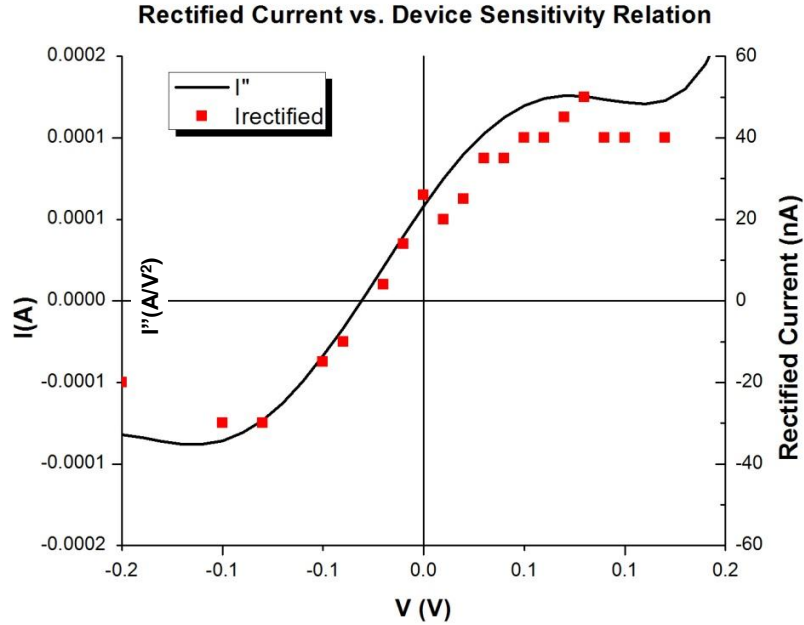


Figure 5.18: Applied bias vs. rectified current and nonlinearity curve at 20GHz [60].

5.3.1 IR Test Set-up

An IR test set-up is built in collaboration with CoolCad Electronics LLC to characterize the Terahertz response of the ACMIM diodes. The layout of this set-up is shown in Figure 5.19. A Synrad 48 series, 10 Watts maximum output-power, air-cooled, continuous-wave CO_2 laser is used as the Terahertz source. The output wavelength is specified to be between 10.2 and $10.8\mu m$ (some possible mode changes are expected to create a distribution of output wavelengths during operation) and it is linearly polarized. Since the laser's output power is too high, to safely shine on the diode surface, 8% of the beam is split by a beam splitter and the rest 92% is discarded by beam attenuators. Then, half of the beam is split again by a second beam splitter, so that 4% of the beam is directed to a power meter that provides

continuous power intensity data to the computer. A red laser is attached to the second beam splitter. Since this visible laser is coupled to the IR beam, it allows for the alignment of the invisible IR so that the peak of the Gaussian shaped, 3.5mm-diameter beam hits the device during the testing. After the second beam splitter, 4% of the total CO_2 laser output irradiation is modulated by a mechanical chopper (commonly at 400Hz frequency) and incident on the ACMIM tunnel diodes.

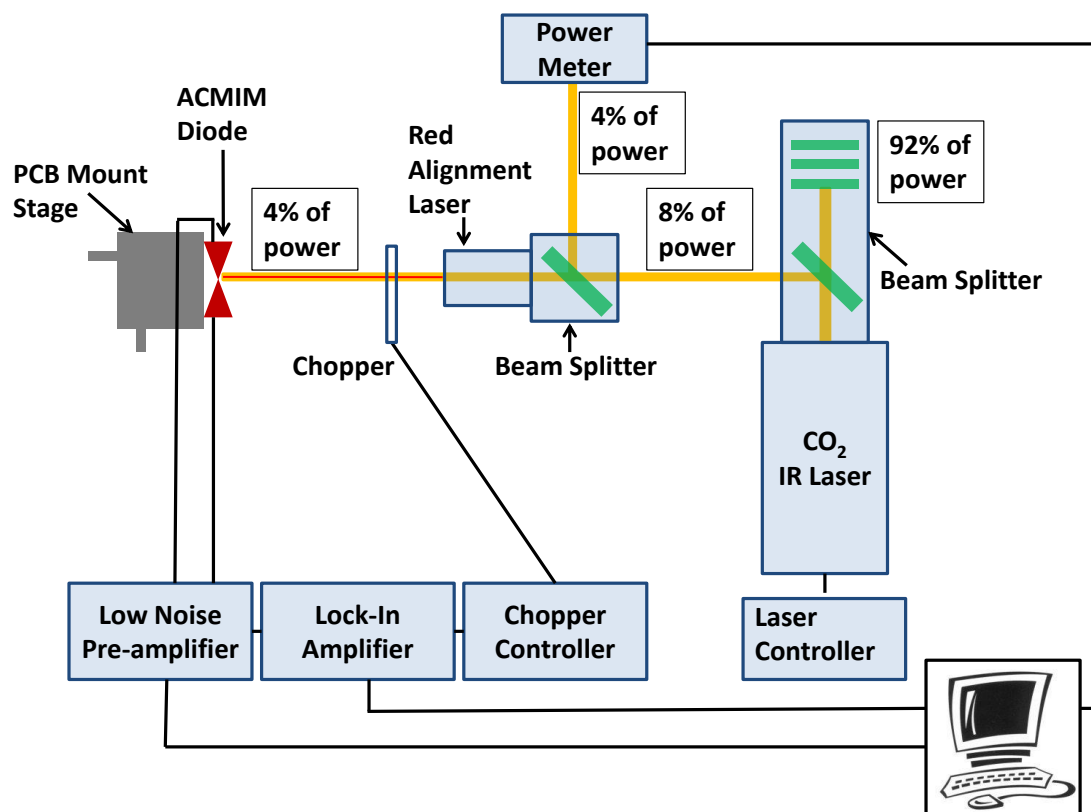


Figure 5.19: IR test set-up.

A low-noise pre-amplifier and a lock-in amplifier are used to detect electrical signal generated in response to IR irradiation on the ACMIM diodes. Conventionally, when the signal to be detected is very small and shadowed by the noise, a lock-in amplifier is used for detection. The lock-in amplifier generates a signal at the ref-

erence frequency (chopper frequency in our case) that corresponds to the frequency of the detected signal with a phase difference. The input signal is multiplied by the internally generated lock-in signal and the resultant product signal is filtered by a low pass filter to remove the high frequency components. When the input signal's frequency matches the reference frequency, a DC output that is proportional to the amplitude of the signal of interest is measured. Lock-in amplifiers not only amplify and detect the signal, but they also filter the noise at frequencies other than the reference frequency. The base noise in this measurement depends on the bandwidth of the low-pass filter. In fact, the bandwidth of the low-pass filter is 0.33 Hz, which is the reciprocal of the time constant (3 sec) set during our measurements.

5.3.2 IR Detection Results

In this section, the responses of the ACMIM diodes are measured for the perpendicular incidence of $10\mu\text{m}$ wavelength CO_2 laser radiation. IR detection characteristics of the ACMIM tunnel diodes are examined and the experimental results are compared with the theoretically derived parameters. Ideally, to obtain a pure IR response, measurements must be performed at cryogenically low temperatures. Since our current test set-up does not support low temperature experiments, the results presented here are obtained at room temperature. The IR data presented in this section was collected by Dr. Siddharth Potbhare at CoolCAD Electronics LLC.

Although IR detection has been tested on several devices, only a few of them will be discussed here. Figure 5.20 shows the bias voltage dependence of the IR

detected current on two different devices. The phase angle profiles at which the lock-in amplifier locks show the reliability of the detection. The phase stays constant as long as there is an input at the reference frequency, and it changes polarization when the detected signal changes sign. The IR data is collected at $1.3W/cm^2$ irradiance over the devices whose junction resistances are $10M\Omega$ (Figure 5.20, left) and $220k\Omega$ (Figure 5.20, right). At the maximum sensitivity points, the detected IR currents are expected to scale with the calculated nonlinearities (which is a junction property) as the incident IR power and the total coupled AC power (which is an antenna property) must be identical on these two ACMIM diodes. The calculated ratio of the maximum nonlinearities is $I''(right)/I''(left) = 7 \times 10^{-8} / 2.5 \times 10^{-9} = 28$ and the ratio of the detected IR current is $I_{IR}(right)/I_{IR}(left) = 100 \times 10^{-12} / 3 \times 10^{-12} = 33$. Therefore, the similarity between these ratios ($33 \sim 28$) proves the correspondence of the experimental to the theoretical results.

Also, the detected IR current, together with the nonlinearity (I'') derived from the I-V curve of the same device (from Figure 5.20 left), are shown in Figure 5.21. As expected, the detected current scales with I'' according to the expression: $I_{IR} = V_{ac}^2 * I'' / 4$. Therefore, from the ratio of I_{IR} to I'' , the magnitude of the coupled AC signal across the MIM junction can be derived as $V_{ac} = 80mV$.

On a different device, with $R_0 = 200k\Omega$, sensitivity calculated from the DC I-V data ($S = \frac{d^2 I_{DC} / dV_{DC}^2}{dI_{DC} / dV_{DC}}$) and measured sensitivity ($S = I_{IR} / P_{inc}$) are presented in Figure 5.22 as a function of bias voltage. The results are compared with the literature [25] (see Figure 5.22, right), where the IR data is obtained from a $R_0 = 400\Omega$ device with an input power of $27 \times 10^{-6}W$ at $1.6\mu m$ wavelength radiation. Since

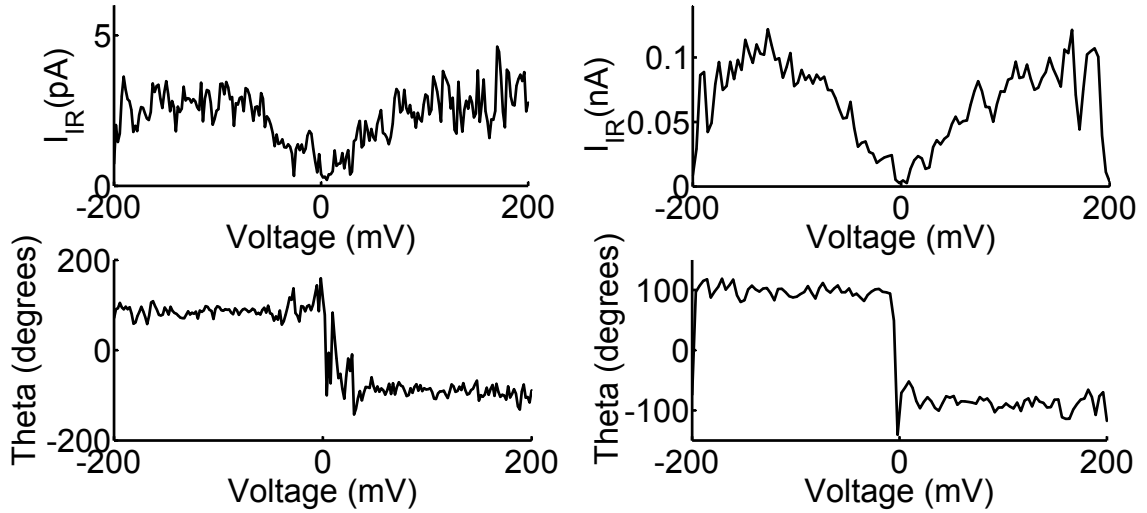


Figure 5.20: IR detected current (top) and lock-in phase data (bottom) as a function of the applied bias voltage at $1.3W/cm^2$ irradiance measured over a $R_0 = 10M\Omega$ device (left) and $R_0 = 220k\Omega$ device(right).

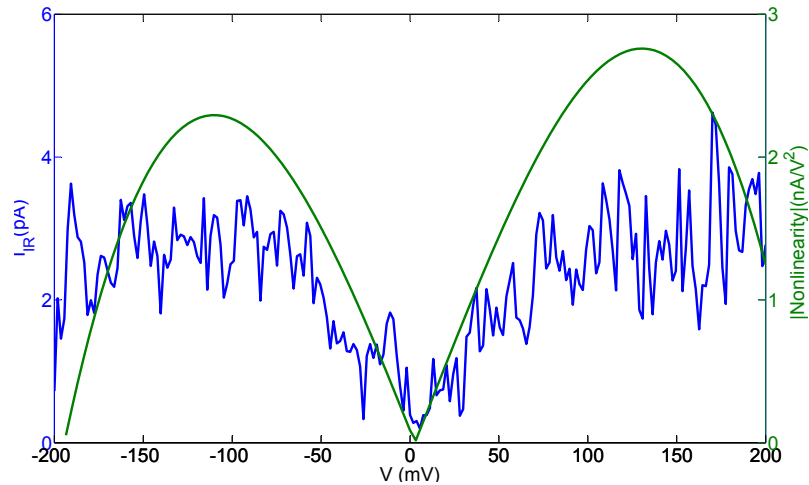


Figure 5.21: Measured IR current and nonlinearity calculated using DC I-V data as a function of applied bias.

these devices were tested at different frequencies, have different DC parameters, and their radiation coupling mechanisms are different (in the named reference, the power is carried to the antenna via a waveguide), the comparison is of a qualitative nature.

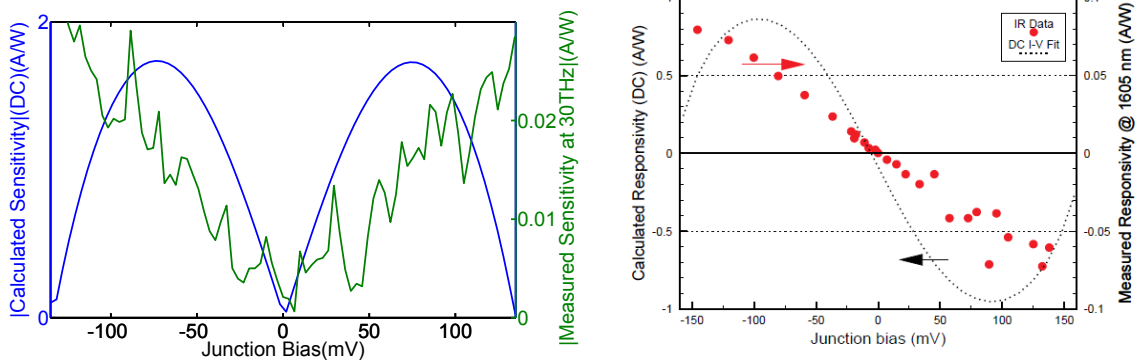


Figure 5.22: Left: sensitivity calculated using DC I-V data and IR measured sensitivity at $1.3W/cm^2$ irradiation of $10\mu m$ light for $200k\Omega$ device as a function of voltage bias. Right: Similar data from Hobbs et. al [25] is shown for further proof of principle. In this reference, sensitivity is obtained over a 400Ω junction with an incident power of $27 \times 10^{-6}W$ at $1.6\mu m$ light.

Both results show that the responsivity scales with the applied bias.

Power dependence of the detected current is investigated on the same device discussed above. Figure 5.23 shows the IR current response when the bias voltage is swept from $-200mV$ to $200mV$ at different irradiance of IR excitation. The power values from $1.75W$ to $0.23W$ represent the power incident on a $1cm^2$ area. The detected power scales down as the incident power decreases. The minimum detectable power is $200mW/cm^2$ for this experiment. The detectable signal is limited by the base noise level, which is set by the bandwidth of the low-pass filter of the lock-in amplifier. The base noise level in our measurements is in the pA range when the filter bandwidth is set to $0.33Hz$. In the Figure 5.23, the phase data at which the amplifier is locked is presented at the bottom. Also, the maximum detected current vs the IR irradiance is shown in Figure 5.24.

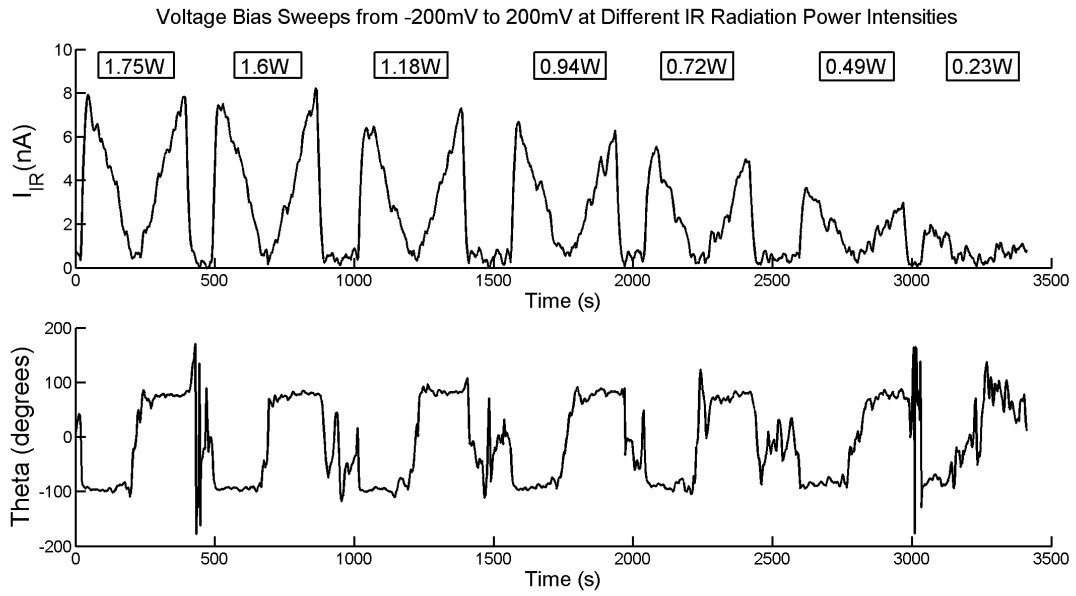


Figure 5.23: IR detected current variation as a function of applied bias between $-200mV$ to $200mV$ at different incident power intensities measured over a device of $R_0 = 200k\Omega$.

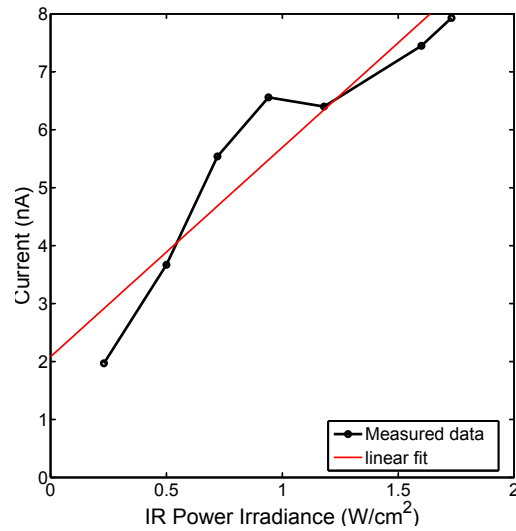


Figure 5.24: IR detected current vs. the irradiance.

In Figure 5.25, initial attempts to demonstrate polarization dependence of the IR detection are presented. Unfortunately, the detected signal rose above the upper detection limit of the lock-in for angles above 67.5° and in the second attempt the device was damaged, therefore the complete polarization dependence has not been shown. Further experiments are necessary to analyze the device response to the incident wave polarization.

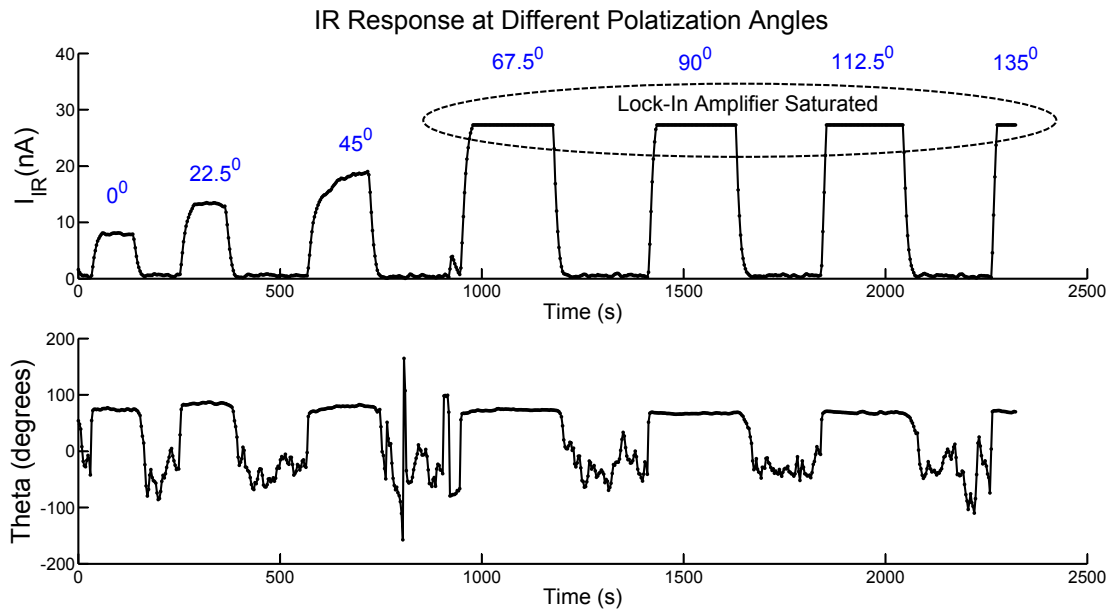


Figure 5.25: IR detected current at $200mV$ bias and $1.8W/cm^2$ irradiance measured at different angles (top) and the phase data (bottom).

Both for the IR detection and the harvesting purposes, the array configuration of the ACMIM diodes is necessary. In Figure 5.26, devices that sit close to each other are parallel connected to demonstrate their bundle operation at $100mV$ bias and $1.8W/cm^2$ irradiation. First, IR generated current of three individual devices (#17, #18, and #19) are measured as $20nA$, $30nA$, and $45nA$, respectively. Then

devices #17+#18 and #18+#19 are connected in parallel and the total IR current of $50nA$ and $75nA$ are measured, respectively. And finally when three of them are connected in parallel approximately $95nA$ is measured. This result, to the best of our knowledge, is the first to show parallel operation of ACMIM diodes. Therefore, when dense array structures of ACMIM diodes are formed, the detected current can be combined leading to higher detected power per area.

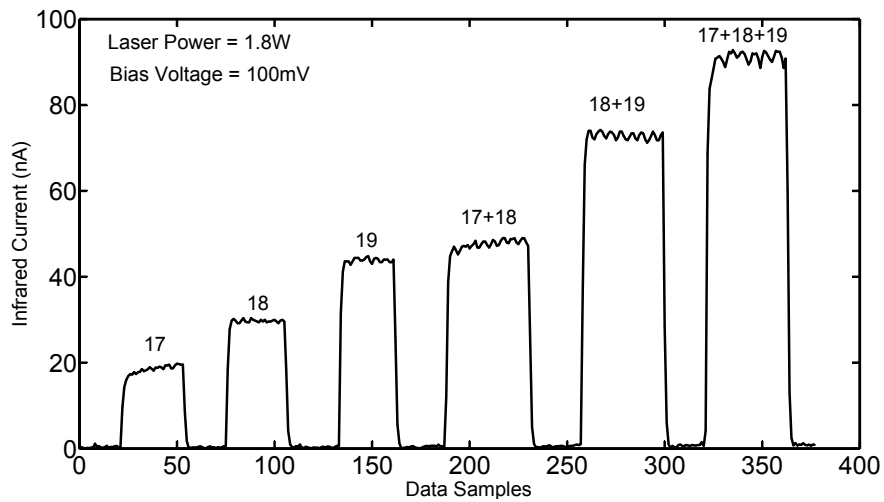


Figure 5.26: IR response obtained from single, double, and triple parallel connected ACMIM diodes.

Figure 5.27 is obtained by scanning the laser beam through three parallel-connected ACMIM diodes introduced above (#17+#18+#19). The IR generated current is recorded when the devices are biased at $100mV$ with $1.8W/cm^2$ incident radiation. Since the laser beam power intensity has a Gaussian shape, the radiation power that reaches the devices first increases as the beam center moves closer and then decreases creating a Gaussian-like shape. In Figure 5.27 (bottom), the data is regenerated incorporating the scan location at the x-axis. This is the first IR image

taken by an IR wave detector in history.

5.4 IR Detector Performance: Figures of Merit

The performance of the ACMIM tunnel diodes can be described using standard figure of merits that are commonly used to evaluate optical detector operation. As each figure of merit provides information on a particular aspect of the detection, judgments that are made considering single figure of merit may be misleading.

5.4.1 Responsivity

Responsivity (or sensitivity) is one of the most important parameters used to qualify detectors. It simply measures the detector output per unit of input power. The input for IR detector is the radiant power and the output is the measurable signal, which can either be current or voltage. Thus, the unit for the responsivity can either be ampere/watt or volt/watt. When the detector is tested under monochromatic radiation, responsivity also provides spectral information and it is called spectral responsivity $R(\lambda)$. If the source provides broadband radiation, the responsivity is called blackbody responsivity and it does not carry any spectral information. Our ACMIM diodes will be evaluated with the output signal of current defined in Equation 5.2. In the equation, I_{IR} is the DC current signal measured when the a radiation of intensity $E_e[watts/cm^2]$ is incident on the detector of area A_{eff} . The total radiant power that the detector interacts can also be stated as the

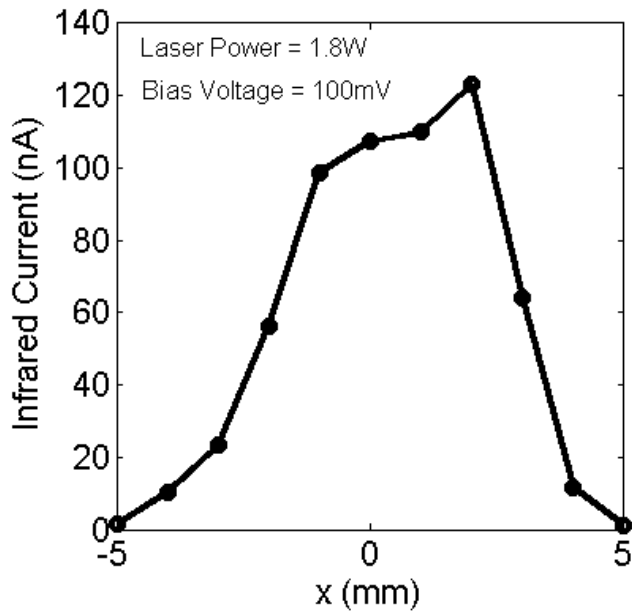
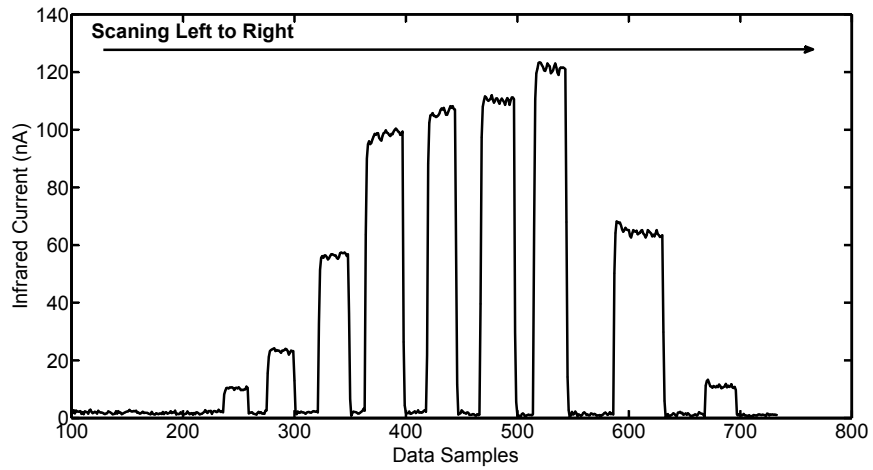


Figure 5.27: Image of the Gaussian IR laser beam profile.

total incident power $P_{inc}[W]$ [38].

$$R_i = \frac{I_{IR}}{E_e * A_{eff}} = \frac{I_{IR}}{P_{inc}} \quad (5.2)$$

5.4.2 Signal-to-Noise Ratio

When single detector elements are considered, small signal detection in a background of noise becomes difficult. Signal-to-noise ratio (SNR) compares the detected signal to the background noise (also stated in Equation 5.3). As a figure of merit, SNR represents the minimum radiant power that can be converted into a functional signal. In fact, SNR should be presented together with the radiant power to provide coherence [38].

$$SNR = \frac{S}{N} = \frac{I_{IR}}{I_N} \quad (5.3)$$

5.4.3 Noise Equivalent Power

Noise-equivalent power (NEP) corresponds to the part of the radiant input power that generates additional output noise at a certain bandwidth. It has the unit of watts as stated in equation 5.4:

$$NEP = \frac{P_{inc}}{I_{IR}/I_N} = \frac{P_{inc}}{SNR} = \frac{I_N}{R_i} \quad (5.4)$$

This figure of merit is highly dependent on the detector area, and measurement bandwidth, because the output noise decreases with the bandwidth. The measurement tools such as lock-in-amplifiers are capable of filtering the measured signal around the chopping frequency through a very narrow bandwidth filters. Consequently, NEP is highly dependent on bandwidth, chopping frequency, bias conditions, and

other environmental factors. It does not convey conclusive information itself and needs to be presented along with the other measurement parameters [38].

5.4.4 Detectivity

Detectivity (D^*) is the only standard figure of merit that eliminates the bandwidth and detector area dependence by normalizing the NEP to a 1cm^2 area and 1 Hz bandwidth. D^* is a common base to compare different detectors. It is essentially the measure of how well the detector can sense the weak (low power) incident radiation, so a larger D^* implies a better detector performance. D^* can be expressed as in Equation 5.5 in terms of different parameters, among which Δf is the bandwidth of the measurement tool (lock-in amplifier in our case). The unit of D^* is $\text{cm} * \sqrt{\text{Hz}}/\text{W}$ [38].

$$D^* = \frac{\sqrt{A_{eff}\Delta f}}{NEP} = \frac{SNR * \sqrt{\Delta f}}{E_e * \sqrt{A_{eff}}} \quad (5.5)$$

Table 5.3 shows the figures of merit of the ACMIM tunnel diode on which we obtained the best IR result so far. In the computations, the effective detector area, noise current and bandwidth are taken as: $A_{eff} = 13 \times 10^{-8}\text{cm}^2$, $I_N = 1 \times 10^{-12}\text{A}$, and $\Delta f = 0.33\text{Hz}$. Our best D^* is calculated as $4 \times 10^7 \text{cm} * \sqrt{\text{Hz}}/\text{W}$

Irradiance [W/cm^2]	I_{IR} [A]	P_{inc} [W]	R_i [A/W]	SNR	NEP [W]	D^* [$\text{cm} * \sqrt{\text{Hz}}/\text{W}$]
1.8	45×10^{-9}	2.34×10^{-7}	1.92×10^{-1}	4.5×10^4	5.2×10^{-12}	4×10^7

Table 5.3: Figures of merit of our best ACMIM diode.

Table 5.4 compares the ACMIM tunnel diodes with the other state-of-the-art LWIR detector technologies in terms of operation temperature, response time and D^* . The data presented in the table reveals that although the ACMIM diode LWIR wave detector technology is orders of magnitude behind the photodetectors in terms of detectivity, it offers the fastest response time and a room temperature operation capability. Moreover, ACMIM diodes have the smallest “pixel” size among the competing devices. Thus, the ACMIM diodes are the most appropriate candidates for the fast, high resolution, room temperature operating, and low cost IR night cameras. On the other hand, there is a lot of room in the design of the ACMIM diodes to improve the detectivity. First of all, the ambient radiation coupling is not the most efficient method, so a proper IR transparent antireflection coating would improve it. Also, the substrate can be designed in such a way that it traps the incident light like a waveguide and allows for the multiple interaction of the wave with the antenna. Different lens structures can also be incorporated to increase D^* .

In the last two rows of Table 5.4, the ACMIM diode wave detector with the best D^* reported in the literature at $10\mu m$ wavelength [5] and our device are compared. The main distinction between the two wave detectors are in the material selection and the process technology. In the named reference a very demanding shadow evaporation method along with a rare and expensive metal (platinum) are used. Thus, unlike our ACMIM diodes, these wave detectors do not allow for low cost, mass process techniques. Moreover, our detectors have higher D^* value than any IR wave detector reported in the literature.

Detector Type	Operation Temperature [K]	Response Time [s]	D* [$cm * \sqrt{Hz}/W$]
Photodetectors (HgCdTe)[46]	77	10^{-6}	2×10^{12}
Photodetectors (HgCdTe)	300	10^{-9}	2×10^8
QWIP (AlGaAs/GaAs)[46]	77	10^{-11}	2×10^{10}
Thermal Detectors	300	10^{-3}	1×10^8
Shadow-evaporation ACMOMD[5] Al/AlO _x /Pt	300	10^{-13}	9.65×10^6
ACMIM Diodes Ni/NiO _x /Ni	300	10^{-13}	4×10^7

Table 5.4: State-of-the-art LWIR detectors and their characteristics.

5.5 Summary

- Planar single-step lithography ACMIM diodes made of PolySi/SiO_x/PolySi and Ni/NiO_x/Ni are compared in terms of their DC I-V parameters. Ni/NiO_x/Ni diodes are shown to be superior due to their lower R_0 .
- Double-step lithography ACMIM diodes are characterized based on DC measurements in a statistical manner.
- It is shown that the junction resistance has a weak junction area dependence.
- The field enhancing tip and edge geometries are shown to improve MIM junction conductance.
- Three oxidation methods used to create NiO_x are compared in terms of yield

and DC parameters. O_2 plasma oxidation at low power setting (20W) produced optimum (thin and rigid) oxide layer for ACMIM diode applications.

- Parameter variation in device groups fabricated identically is explained by the nickel surface roughness after AFM surface analysis.
- ACMIM performance variation over time is measured and gradually decreasing rise in the junction resistance is observed with time.
- RF frequency (6GHz and 20GHz) detection is achieved with ACMIM diodes.
- IR ($10\mu m$) detection is achieved with ACMIM diodes with a detectivity of $4 \times 10^7 \text{ cm} * \sqrt{\text{Hz}}/W$. This is the best performance parameter ever reported for IR wave detectors. Power intensity and bias voltage effects on IR detection is shown.
- It is shown that, when ACMIM diodes are parallel connected, the total IR generated current is equal to the sum of individual ACMIM diode currents.
- The image of the laser beam is taken by scanning the beam through the device, which represents the first IR image created by the IR wave detectors in the history.

Chapter 6

Conclusions and Suggestions for Further Work

In this dissertation, we have demonstrated $10\mu m$ wavelength IR radiation detection by Ni/NiOx/Ni ACMIM tunnel diodes. In the design and fabrication of ACMIM diodes, our priority was to lower the processing costs and enable the use of large area lithography technologies, such as nano-imprint. The resulting ACMIM diodes can be used for both thermal imaging and energy harvesting applications. For the first time we have shown that output power from multiple ACMIM diodes can be added in parallel an important consideration for an energy harvester. Also, we have shown that these diodes can create useful infrared images.

We have used a finite-element multi-physics simulation tool (COMSOL) to optimize the device geometry for $10\mu m$ wavelength radiation coupling. In the electrostatic analysis, we have studied the effect of the tip radius-of-curvature, gap width between the antenna parts, bow-tie flare angle, and pattern imperfections on the E-field enhancement and MIM junction capacitance. The simulation results showed that the sharp tip dominantly enhances the E-field while decreasing the capacitance between the electrodes. These results theoretically prove that MIM junction resistance and capacitance can be decoupled when a sharp tip cathode is used.

In addition, for antenna radiation coupling characterization, we have used AC time-harmonic computations in the three-dimensional vector domain. Bow-tie

antennas, known to offer broadband frequency and large polarization span coupling, are simulated. In an air ambient, $3\mu m$ antenna half-length is observed to generate the highest E-field enhancement when $10\mu m$ wavelength radiation is incident. The simulation results showed that our bow-tie antennas have 30 THz FWHM frequency bandwidth, between $6.25\mu m$ and $16.7\mu m$ wavelengths. Also, we have shown that at least 50% of the maximum E-field enhancement is sustained for 240° polarization angle span. Moreover, it is observed that the coupling efficiency can be enhanced when the antenna is excited through a properly designed dielectric material.

We have successfully integrated the geometric field enhancement that leads to lower forward resistance, and decoupled the junction resistance from the capacitance. The effect of E-field enhancing geometries, such as tips and edges, on the MIM performance is experimentally shown. Based on the statistically collected data, we have observed that the junction resistance has weak area dependence, and that the tip and edges dominate the conduction in MIM junctions. The control of the parasitic resistance and capacitance enabled Terahertz detection with the MIM diode.

We have devised and characterized a processing method centering around advanced lithography procedures to create the ACMIM tunnel diodes with the highest rectification capabilities. We used EBL together with resolution enhancing proximity effect correction and aligning methods to create a very sharp tip at the MIM junction. We created tips with radius-of-curvature $\leq 10nm$. In our processes, the sharpness of the tip is limited by the material grain boundaries, not by the lithographic resolution.

We have invented a novel fabrication technique called “strain assisted self lift-off process”. The major contribution of this process is the elimination of parasitic capacitance without relying on extreme-high resolution lithography technologies. Removing the overlapping part of the junction, this process limits the conduction to the electrode edges where the E-field concentrates and the charge transport eminently occurs.

Future Work. One of the next steps to advance ACMIM diode technology is to improve the antenna radiation coupling. Instead of relying on the direct air coupling, an anti reflective coating on the device plane should be included in future designs. In addition, the back side of the chip should be metal coated to redirect the radiation back onto the antenna-forming a kind of resonant cavity. This way, multiple excitation would be possible and the antenna coupling efficiency can be increased.

The yield of a process and the stability of devices mostly depend on the robustness of the insulating layer of the MIM diode. Devices fail when this film is too thick or too thin. After considering various oxidation methods, we have observed that O_2 plasma oxidation of Ni at low RF power creates stable and sensitive MIM junctions. However, process variation and performance change over time persist as major issues. The research on optimizing the insulating film growth should continue in the future. We have observed inhomogeneities in the plasma that forms in the RF chamber. Thus, other plasma generating equipments should be explored. To control the process variation further, electrochemical surface polishing and anodic oxidation methods should be investigated.

We further propose nanoimprint lithography for future large area implementation of the ACMIM tunnel diodes. Nanoimprint technology is an active research field that provides high-throughput, low-cost process [10] and it offers sub- $10nm$ resolution [11]. It is shortly summarized in Fig. 6.1.

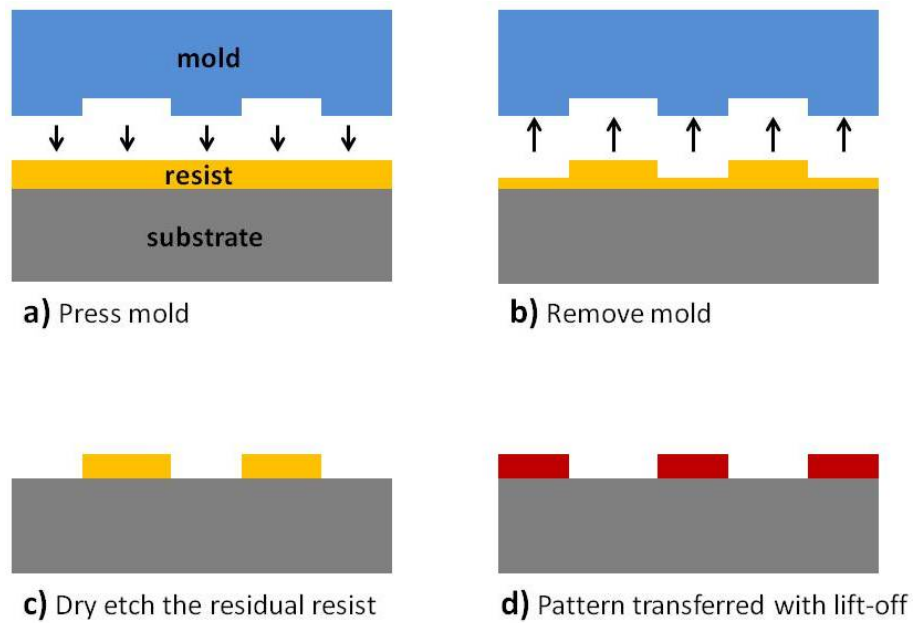


Figure 6.1: Nano-imprint process steps.

Appendix A

MIM Conduction Mechanisms

A.1 Field-Assisted Tunneling Current

The field-assisted tunneling (or Fowler-Nordheim tunneling) current J through an insulator film of a MIM junction of similar electrodes is formulated as in Equation A.1 [51]:

$$J = J_0 \left\{ \bar{\varphi} \exp\left(-A_{tun} \bar{\varphi}^{\frac{1}{2}}\right) - (\bar{\varphi} + eV) \exp\left[-A_{tun} (\bar{\varphi} + eV)^{\frac{1}{2}}\right] \right\}, \quad (\text{A.1})$$

where the proportionality constant J_0 is given by:

$$J_0 = \frac{e}{2\pi h (\beta \Delta s)^2}, \quad (\text{A.2})$$

and A_{tun} is given by:

$$A_{tun} = (4\pi\beta\Delta s/h)(2m^*)^{\frac{1}{2}}, \quad (\text{A.3})$$

and the mean barrier height $\bar{\varphi}$ is:

$$\bar{\varphi} = \frac{1}{\Delta s} \int_{s_1}^{s_2} \varphi dx. \quad (\text{A.4})$$

In Equation A.2, e is the electron charge, h is the Plank's constant, and β is the correction factor that scales the effective barrier height considering the image potential. In Equation A.3, m^* is the effective electron mass, s_1 and s_2 are the metal barrier boundaries. Finally $\Delta s = s_2 - s_1$ is the total barrier width in Equation A.4.

This expression can be analyzed in two parts. When applied potential is much less than the mean barrier height (around zero bias), current density is linearly proportional to the applied bias. Therefore junction is ohmic and the general tunneling equation can be reevaluated as follows:

$$J = \left[(2m^*)^{\frac{1}{2}} / \Delta s \right] (e/h)^2 \bar{\varphi}^{\frac{1}{2}} V \exp(-A\bar{\varphi}^{\frac{1}{2}}) \quad (\text{A.5})$$

In the high voltage range (when the voltage exceeds the barrier height), mean barrier height is constant and equal to half the equilibrium barrier height ($\bar{\varphi} = \Phi_0/2$), but the barrier width scales down as the applied bias increases ($\Delta s = \Delta s_0 \Phi_0 / eV$). As a result, current is exponentially bias dependent in this range.

A.2 Thermionic Emission Current

Thermionic emission from metal into vacuum can be stated by the famous Richardson-Dushman equation as in equation A.6:

$$J = AT^2 \exp \frac{-\phi}{k_B T}, \quad (\text{A.6})$$

where T is the temperature, ϕ is the metal work-function, k_B is the Boltzmann's constant, and

$$A = \frac{4\pi m e k_B^2}{h^3}, \quad (\text{A.7})$$

where m is the electron mass and h is Plank's constant.

If we want to apply this to a two electrode MIM system, the emission from both electrodes should be considered and the thermionic current takes the following

form [52]:

$$J = AT^2 \left(\exp \frac{-\phi'_1}{k_B T} - \exp \frac{-\phi'_2}{k_B T} \right), \quad (\text{A.8})$$

where ϕ'_1 and ϕ'_2 are the maximum barrier heights at the terminals above the Fermi level. When a positive bias V is applied to second electrode ($\phi'_2 = \phi'_1 + eV$), the net thermionic emission current can be stated as:

$$J = AT^2 \exp \frac{-\phi'_1}{k_B T} \left(1 - \exp \frac{-eV}{k_B T} \right). \quad (\text{A.9})$$

As stated in Equation A.9, thermal current is strongly barrier height dependent. For low barrier height MIM junctions, the thermal current effects must be considered.

A.3 Poole-Frenkel Effect

Poole-Frenkel effect can be observed in the MIM junctions as a bulk conduction mechanism where electrons tunnel into the trap states in the insulator instead of directly reaching to the interface states of the opposite electrode. It generates a bulk controlled conduction unlike the interface controlled conduction in the field or thermal assisted current types. However, it can be driven by either the thermal or the E-field energy present at the junction. Unless the insulator is grown using atomic layer deposition tools to produce perfect insulator crystal, the traps in the metal-oxide insulation layer will be abundant. Hence, it is expected to encounter trap assisted tunneling phenomena in the MIM junctions due to the defective insulation layer.

The Poole-Frenkel current may contribute to the total tunneling current by providing midway electron traps in the existence of high E-field across the insulator film. Racko et al. theoretically analyzed the effects of traps on the total tunneling current [45]. According to this work, the direct tunneling dominates in the low barrier height MIM junctions, whereas the trap assisted tunneling is more significant in the tall barrier junctions. Therefore, the Poole-Frenkel effect is not the dominant conduction mechanism in Ni/NiOx/Ni MIM junctions with low barrier heights.

Appendix B

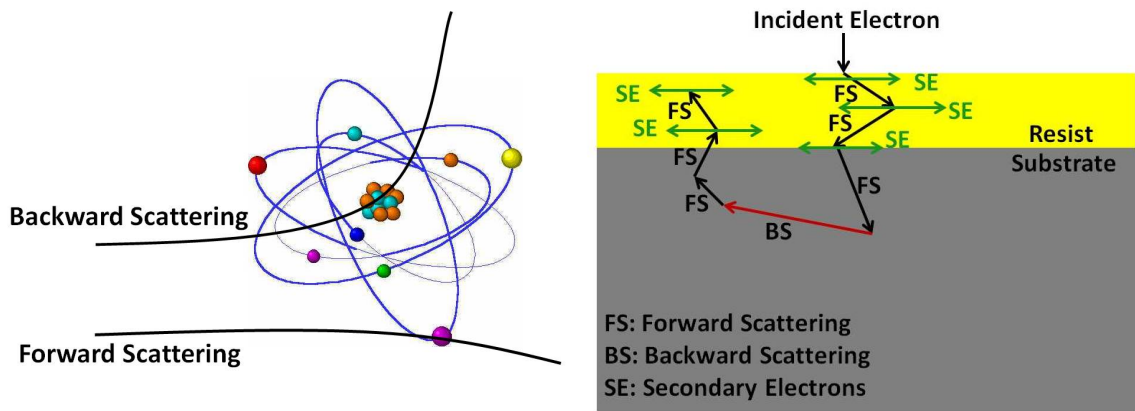
Proximity Effect Correction using Linear Programming Methods

B.1 Electron Solid Interactions

Detailed characterization of electron behavior in the resist is crucial in EBL for almost ideal patterning. The most important electron solid interaction that fundamentally causes the proximity effect is scattering. Today's EBL machines supply electrons that are in the energy range of 10-100 keV. Thus, electrons are sufficiently energetic as to penetrate through the resist and reach the substrate. Two fundamental types of scattering occur during the electrons travel in the solid: forward scattering and back scattering.

Forward scattering is created by the collisions of incident electrons with electrons resident in the scattering atoms that belong to resist or substrate molecules. It is a common inelastic scattering process that causes a slight change in the trajectory of the electron as can be seen in Figure B.1 (a). Forward scattering contributes to broadening in the incident beam by either changing the trajectory of the incident electron or creating secondary electrons with a few eV of energy in the material. On the other hand, backward scattering occurs occasionally when a primary electron hits the nucleus of the native atoms that belong to resist or substrate molecules. It is an elastic scattering where the electron keeps its high energy but changes its direction as shown in Figure B.1 (b). Since the electrons continue to move with a

high energy in different directions, they transfer energy into the unintended areas in the resist, considerably broadening the beam. Since the resist exposure happens when a chemical change occurs in the resist molecule chain, low energy secondary electrons created by the forward scattering are the main source of exposure in the resist.



(a) Forward and backward scattering (b) Scattering in resist and substrate

Figure B.1: Resist Exposure

B.2 Mathematical Modeling of Electron Beam

Resolution improvement in EBL strongly depends on an understanding of the proximity effect in all its manifestations. In fact, computer simulations are proven to be the most accurate method of demonstrating proximity effect. Mathematical modeling of the e-beam in the solid can be stated as the first step of carrying this physical phenomenon into the computer environment. Energy density profile in the resist introduced by a point source of incident electrons is often called Point

Spread Function (PSF) and can be determined either by analytical or experimental methods. Mathematically, the simplest way of modeling PSF is by superimposing two Gaussian distributions with different standard deviations, each representing the backward and forward scattered electrons as in equation 1 [6].

$$f(r) = \frac{1}{\pi(1 + \eta)} \left[\frac{\exp(-\frac{r^2}{\alpha^2})}{\alpha^2} + \eta \frac{\exp(-\frac{r^2}{\beta^2})}{\beta^2} \right] \quad (\text{B.1})$$

The variables in the equation are as follows:

r -radial distance from the point of incidence

λ -half width of the electron distribution due to forward scattering

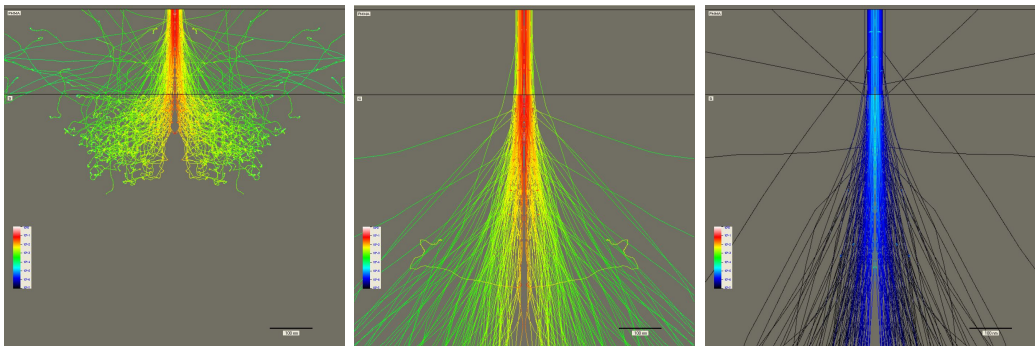
β -half width of the electron distribution due to backward scattering

η -ratio of backward to forward scattered electron distribution

B.3 Physical Factors Affecting the PSF

Both experimental and analytical results show that many factors contribute to proximity effect such as beam energy, substrate type, resist type, thickness, and development conditions. Beam energy is the most significant of these factors. As the energy of the incident beam increases, the speed of the electrons traveling in the resist increase, while energy deposition per unit path length decrease. Thus, electrons in a low energy beam dissipate their energies in a very short vertical range ($1.5\mu m$) and provoke a lateral spread of the energy due to secondary electron generation. On the other hand, electrons in high-energy beam reach the substrate without generating enough secondary electrons during their travel in the resist. Moreover, these high-energy electrons experience large amounts of backscattering in

the substrate and give rise to an excessive lateral broadening. As a result, forward scattering dominates in the low energy beams, defining a very short ($\leq 2\mu\text{m}$) forward scattering range; on the other hand, backward scattering dominates in high energy beams, resulting in a large lateral scattering range ($\geq 2\mu\text{m}$). Below, in Figure B.2 this phenomenon is demonstrated on the images generated by Monte Carlo simulation [61].



(a) $5kV$ Beam

(b) $30kV$ Beam

(c) $50kV$ Beam

Figure B.2: Electron energy distribution in the resist (above the line) and the substrate (below the line with 5, 30 and $50kV$ acceleration voltage)

As a result of the electron scattering, two main types of proximity effects are commonly observed in implementation: (1) Inter-shape proximity effects (2) Intra-shape proximity effects [42], [41](see figure B.3). Inter-shape proximity effects are introduced by the long-range backward scattering of the electrons. Backscattered electrons cause exposures away from the incident beam and contribute to the overexposure of the adjacent patterns. On the other hand, intra-shape proximity effects are introduced by the short-range forward scattering of the electrons. Due to the accumulation of the forward scattered electrons non-uniformity occurs inside

the pattern element. This phenomenon has two types of outcomes: pattern size dependent exposure and deterioration in shape fidelity.

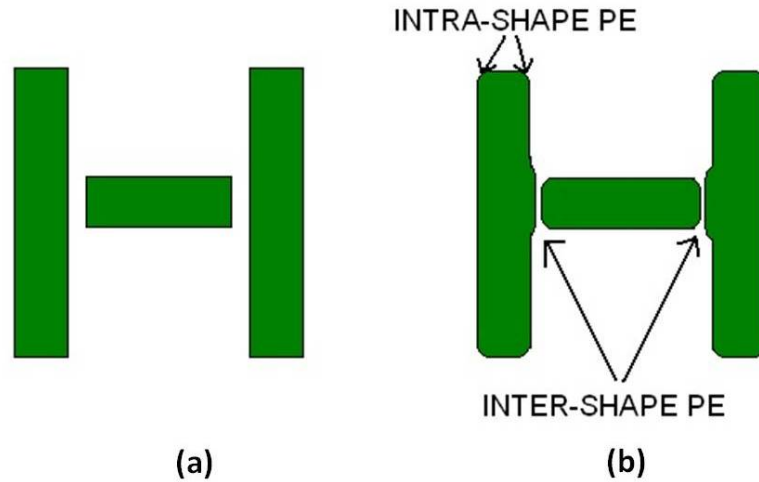


Figure B.3: Inter and Intra proximity effects in implementation: (a) Target pattern
(b) Pattern after exposure

B.4 A Mathematical Formal Statement of Proximity Effect Problem

Mathematical modeling of the PE plays a vital role in the development of correction algorithms. We start with a dose-deposition model summing the entire energy incident in a pixel from its various sources. Below is the terminology to be used in modeling.

- $G(x, y)$: Point Spread function (described in the text).
- $M(i, j)$: Interaction matrix. This function captures the degree to which energy deposited in the i^{th} pixel contributes to energy absorbed in the j^{th} pixel. It is derived from the point spread function.
- $P(x, y)$: Target pattern dose distribution function (desired dose distribution).
- d_p : Target pattern dose distribution vector. A 1-dimensional vector whose entries can be viewed as a discretization and “unstringing” of the target pattern function.
- $D_I(x, y)$: Incident dose function. This gives the amount of energy directly deposited by the beam in a given pixel, indexed (i,j).
- d_I : Incident dose vector. A 1-dimensional vector whose entries can be viewed as a discretization and “unstringing” of the incident dose function.
- $D_A(x, y)$: Absorbed dose function. This gives the total energy actually absorbed by a given pixel, indexed (i,j).
- d_A : Absorbed dose vector. A 1-dimensional vector whose entries can be viewed as a discretization and “unstringing” of the absorbed dose function.
- (i, j) : Discretized pixel address.

Note that all of the continuous two dimensional distribution functions can be discretized by replacing the (x, y) by the index (i, j) . The continuous and the discrete absorbed energy profile can best be approximated by the convolution of the point spread function and the applied dose matrix as in equations B.2 and B.3,

respectively.

$$D_A(x, y) = G(x, y) \otimes D_I(x, y) \quad (\text{B.2})$$

$$D_A(i, j) = \sum_{k=-\infty}^{+\infty} \sum_{l=-\infty}^{+\infty} G(i, j) D_I(i - k, j - l) \quad (\text{B.3})$$

“Ideal exposure” happens when D_A is equal to P , also defined as below:

if $P(x, y) = 1$, then $D_A(x, y) = 1$;

or if $P(x, y) = 0$, then $D_A(x, y) = 0$

In a mathematical sense, proximity effect arises simply because the ideal exposure defined above is not possible by applying a uniform dose to the target pattern. That is, the difference between $D_A(x,y)$ and $P(x,y)$ increases as $G(x,y)$ degrades from being a delta function to a Gaussian distribution.

Various proximity effect correction (PEC) methods have been developed until today and they fundamentally aim to meet the ideal exposure condition. The first group of PEC basically intends to modify the point spread function (G) (physical modification techniques) so that it converges to a delta function. The second group deals with the incident dose function (D_I) modification either by altering the pattern matrix but keeping the dose same everywhere (shape modulation techniques) or by varying the dose per each pixel in the pattern matrix (dose modulation techniques).

Improvement in EBL resolution is indispensable to overcome the challenges in the fabrication of the ACMIMs. A PEC technique that relies on linear programming methods is used. This technique fundamentally modifies the target pattern by assigning different dose values at each pixel. A dose compensated array is created by

the software and used as the EBL mask instead of a uniform dose assigned pattern. The details of this PEC method will be presented below.

B.5 Mathematical Redefinition of the PE as a Linear Optimization Problem

Proximity effects can be best modeled by computing the total accumulated dose in each pixel. In equation B.4, the convolution is performed by simple vector multiplication. The matrix M is called the interaction matrix and it is obtained from the PSF.

$$\mathbf{M} * \mathbf{d}_I = \mathbf{d}_A \tag{B.4}$$

Early linear approaches attempted to achieve ($D_A = P$). This led to mathematical inconsistencies (negative dose requests). The mathematical model used for the linear optimization approach is relatively different compared to earlier approaches [43],[44]. First of all, it recognizes that the $D_A = P$ requirement is unrealistic and practically “infeasible”. Second, it does not demand a single dose in the exposed field and zero dose in the unexposed field. But rather, the demand is for the exposed pixels to achieve a dose greater than resist exposure threshold and the dose to the unexposed field should be less than a tolerable level.

Linear Optimization (LO) Approach:

$$f = \|\mathbf{M} * \mathbf{d}_I - \mathbf{d}_p\| \rightarrow \textit{minimum} \tag{B.5}$$

Other Approaches:

$$f = \|\mathbf{M} * \mathbf{d}_I - \mathbf{d}_p\| = 0 \tag{B.6}$$

The LO approach aims to find the extrema of a given function under certain limitations. The approach develops physics-based optimization criteria and expresses these as a cost function. One such cost function is minimizing the total dose applied, as expressed in equation B.7.

$$c(d_I) = \mathbf{d}_p^T * \mathbf{d}_I \quad (\text{B.7})$$

The constraints to be satisfied by the variable of the cost function are listed below:

$$\mathbf{d}_{Ae} \geq \mathbf{b}_1 \quad (\text{B.8})$$

$$\mathbf{d}_{Au} \leq \mathbf{b}_2 \quad (\text{B.9})$$

$$\mathbf{d}_I \geq \mathbf{0} \quad (\text{B.10})$$

where d_{Ae} and d_{Au} are the total dose accumulated at an exposed pixel and unexposed pixel, respectively.

The mathematical model stated by the equations B.8-B.10 above is solvable for the entries of the vector d_I , using linear optimization methods such as simplex or interior point methods. Indeed, the basic mechanism used by these methods can be summarized like this. The constraint equations form planes in the n-dimensional space where n is the number of pixels in our case. And these planes intersect with each other forming a geometrical structure called simplex. Another plane in the same space represents the cost function. In order to find the minimum of this function, the cost function plane is lowered until it intersects with only a single point of the simplex. It is mathematically proven that if a solution exists for a particular

problem, it has to be on one of the vertex points of the simplex. As a result, the coordinates of the vertex point where the cost function plane touches the simplex gives the solution (the incident dose matrix in our case).

The first constraint in equation B.8 is defined for the feature pixels so that total dose they obtain is over a certain threshold, b_1 . This threshold is a property of the resist system (type, thickness of the resist) being used and can be stated as the minimum dose to expose one pixel completely. The second condition expressed in equation B.9 is for the off-feature pixels, where no direct exposure is sent. These pixels are required to have a total dose below a certain threshold, b_2 so that they are not exposed. The third constraint in equation B.10 is a natural outcome of using linear optimization theory to solve this problem, because it requires all optimized variables to be positive. This is a great advantage of this technique because negative dose values will never be part of a feasible solution. It is important to mention that the mathematical model introduced above takes the real world resist parameters into consideration. The fundamental objective of PEC is to solve this mathematical system so that the edge contrast defined is maximum, but nature might not always permit the solution of this system with the desired thresholds. This information is precious because it designates the limits of the EBL for a distinct pattern. When this technique tells us that solution is not feasible, one has to relax the thresholds by sacrificing the high contrast. Despite the fact that this will induce incrementally more proximity effect, one can still get satisfactory results.

Bibliography

- [1] Geoffrey C. Allen, Philip M. Tucker, and Robert K. Wild. Surface oxidation of nickel metal as studied by x-ray photoelectron spectroscopy. *Oxidation of Metals*, 13:223–236, 1979. 10.1007/BF00603667.
- [2] Ivan Alvarado-Rodriguez. Ebl calibration notes,ucla nanoelectronics research facility.
- [3] Carter M. Armstrong. The truth about terahertz. *IEEE Spectrum*, 49(9), September 2012.
- [4] Berland B., Simpson L., Nuebel G., Collins T., and Lanning B.. Optical rectenna for direct conversion of sunlight to electricity. *In National Center for Photovoltaics Program Review Meeting.*, pages 323–324, 2001.
- [5] J.A. Bean, A. Weeks, and G.D. Boreman. Performance optimization of antenna-coupled al- alo- pt tunnel diode infrared detectors. *Quantum Electronics, IEEE Journal of*, 47(1):126 –135, jan. 2011.
- [6] T. H. P. Chang. Proximity effect in electron-beam lithography. *Journal of Vacuum Science and Technology*, 12(6):1271–1275, 1975.
- [7] Kwangsik Choi, Geunmin Ryu, Filiz Yesilkoy, Athanasios Chryssis, Neil Goldman, Mario Dagenais, and Martin Peckerar. Geometry enhanced asymmetric rectifying tunneling diodes. volume 28, pages C6O50–C6O55. AVS, 2010.
- [8] Kwangsik Choi, F. Yesilkoy, A. Chryssis, M. Dagenais, and M. Peckerar. New process development for planar-type cic tunneling diodes. *Electron Device Letters, IEEE*, 31(8):809 –811, aug. 2010.
- [9] Kwangsik Choi, F. Yesilkoy, Geunmin Ryu, Si Hyung Cho, N. Goldman, M. Dagenais, and M. Peckerar. A focused asymmetric metal-insulator-metal tunneling diode: Fabrication, dc characteristics and rf rectification analysis. *Electron Devices, IEEE Transactions on*, 58(10):3519 –3528, oct. 2011.
- [10] Stephen Y. Chou, Peter R. Krauss, and Preston J. Renstrom. Nanoimprint lithography. volume 14, pages 4129–4133. AVS, 1996.
- [11] Stephen Y. Chou, Peter R. Krauss, Wei Zhang, Lingjie Guo, and Lei Zhuang. Sub-10 nm imprint lithography and applications. *Journal of Vacuum Science Technology B: Microelectronics and Nanometer Structures*, 15(6):2897 –2904, nov 1997.
- [12] J. W. Dees. Detection and harmonic generation in the submillimeter wavelength region. *Microwave Journal*, 9:48–55, 1966.

- [13] G. M. Elchinger, A. Sanchez, C. F. Davis, and A. Javan. Mechanism of detection of radiation in a high speed metal metal oxide metal junction in the visible region and at longer wavelengths. *Journal of Applied Physics*, 47(2):591–594, feb 1976.
- [14] K. M. Evenson, J. S. Wells, L. M. Matarrese, and L. B. Elwell. Absolute frequency measurements of the 28 and 78 μ m cw water vapor laser lines. *Applied Physics Letters*, 16(4):159–162, feb 1970.
- [15] S. Faris, T. Gustafson, and J. Wiesner. Detection of optical and infrared radiation with dc-biased electron-tunneling metal-barrier-metal diodes. *Quantum Electronics, IEEE Journal of*, 9(7):737–745, Jul 1973.
- [16] R. H. Fowler and L. Nordheim. Electron Emission in Intense Electric Fields. *Royal Society of London Proceedings Series A*, 119:173–181, May 1928.
- [17] Christophe Fumeaux, Glenn D. Boreman, Werner Herrmann, Fritz Kurt Kneubühl, and Hugo Rothuizen. Spatial impulse response of lithographic infrared antennas. *Appl. Opt.*, 38(1):37–46, Jan 1999.
- [18] Samuel I. Green. Point contact mom tunneling detector analysis. *Journal of Applied Physics*, 42(3):1166–1169, mar 1971.
- [19] Samuel I. Green. Point contact mom tunneling detector analysis. *Journal of Applied Physics*, 42(3):1166–1169, 1971.
- [20] S. Grover and G. Moddel. Applicability of metal/insulator/metal (mim) diodes to solar rectennas. *Photovoltaics, IEEE Journal of*, 1(1):78–83, july 2011.
- [21] R. Gupta and B. G. Willis. Nanometer spaced electrodes using selective area atomic layer deposition. *Applied Physics Letters*, 90(25):253102, 2007.
- [22] T. K. Gustafson, R. V. Schmidt, and J. R. Perucca. Optical detection in thin-film metal-oxide-metal diodes. *Applied Physics Letters*, 24(12):620–622, 1974.
- [23] Thomas E. Hartman. Tunneling of a wave packet. *Journal of Applied Physics*, 33(12):3427–3433, 1962.
- [24] M. Heiblum, Shihyuan Wang, J. Whinnery, and T. Gustafson. Characteristics of integrated mom junctions at dc and at optical frequencies. *Quantum Electronics, IEEE Journal of*, 14(3):159–169, Mar 1978.
- [25] Philip C. D. Hobbs, Robert B. Laibowitz, Frank R. Libsch, Nancy C. LaBianca, and Punit P. Chiniwalla. Efficient waveguide-integrated tunnel junction detectors at 1.6 μ m. *Opt. Express*, 15(25):16376–16389, Dec 2007.
- [26] L. O. Hocker, D. R. Sokoloff, V. Daneu, A. Szoke, and A. Javan. Frequency mixing in the infrared and far infrared using a metal to metal point contact diode. *Applied Physics Letters*, 12(12):401–402, jun 1968.

- [27] A. Rogalski J. Piotrowski. Uncooled long wavelength infrared photon detectors. *Quantum Sensing and Nanophotonic Devices*, 5359, 2004.
- [28] B.M. Kale. Electron tunneling devices in optics. *Opt. Eng.*, 24:267 – 274, 1985.
- [29] D. K. Kotter, S. D. Novack, W. D. Slafer, and P. J. Pinhero. Theory and manufacturing processes of solar nanoantenna electromagnetic collectors. *Journal of Solar Energy Engineering*, 132(1):011014, 2010.
- [30] Bailey R. L. A proposed new concept for a solar- energy converter. *Journal of Engineering for Power*, 73, April, 1972.
- [31] A. Mayer, M. S. Chung, P. B. Lerner, B. L. Weiss, N. M. Miskovsky, and P. H. Cutler. Classical and quantum responsivities of geometrically asymmetric metal-vacuum-metal junctions used for the rectification of infrared and optical radiations. 29(4):041802, 2011.
- [32] A. Mayer, M. S. Chung, B. L. Weiss, N. M. Miskovsky, and P. H. Cutler. Three-dimensional analysis of the geometrical rectifying properties of asymmetric metal-vacuum-metal junctions and extension for energy conversion. *Phys. Rev. B*, 77:085411, Feb 2008.
- [33] R. A. Millikan and Carl F. Eyring. Laws governing the pulling of electrons out of metals by intense electrical fields. *Phys. Rev.*, 27:51–67, Jan 1926.
- [34] N. M. Miskovsky, P. H. Cutler, A. Mayer, B. L. Weiss, Brian Willis, T. E. Sullivan, and P. B. Lerner. Nanoscale devices for rectification of high frequency radiation from the infrared through the visible: A new approach. *Journal of Nanotechnology*, 2012.
- [35] Moichiro Nagae. Response time of metal-insulator-metal tunnel junctions. *Japanese Journal of Applied Physics*, 11(11):1611–1621, 1972.
- [36] H.Q. Nguyen, P.H. Cutler, T.E. Feuchtwang, Z.-H. Huang, Y. Kuk, P.J. Silverman, A.A. Lucas, and T.E. Sullivan. Mechanisms of current rectification in an stm tunnel junction and the measurement of an operational tunneling time. *Electron Devices, IEEE Transactions on*, 36(11):2671 – 2678, nov 1989.
- [37] Nordheim. *Z. f. Physik*, 46:833, 1928.
- [38] S. Nudelman. The detectivity of infrared photodetectors. *Appl. Opt.*, 1(5):627–636, Sep 1962.
- [39] Sophocles J. Orfanidis. *Electromagnetic Waves and Antennas*. 2008.
- [40] Edward D. Palik. *Handbook of Optical Constants of Solids*. Academic Press, 1985.

- [41] Mihir Parikh. Corrections to proximity effects in electron beam lithography.(i. theory)(ii. implementation). *Journal of Applied Physics*, 50(6):4378–4382 and 4383, 1979.
- [42] Mihir Parikh. Calculation of changes in pattern dimensions to compensate for proximity effects in electron lithography. *Journal of Applied Physics*, 51(1):705 – 709, 1980.
- [43] Martin Peckerar, Robert Bass, and Kee Woo Rhee. Sub-0.1 μ m electron-beam lithography for nanostructure development. volume 18, pages 3143–3149. AVS, 2000.
- [44] Martin Peckerar, David Sander, Ankur Srivastava, Adakou Foli, and Uzi Vishkin. Electron beam and optical proximity effect reduction for nanolithography: New results. volume 25, pages 2288–2294. AVS, 2007.
- [45] Juraj Racko, Miroslav Mikolek, Ralf Granzner, Juraj Breza, Daniel Donoval, Alena Grmanov, Ladislav Harmatha, Frank Schwierz, and Karol Frhlich. Trap-assisted tunnelling current in mim structures. *Central European Journal of Physics*, 9:230–241, 2011. 10.2478/s11534-010-0027-7.
- [46] A. Rogalski. Infrared detectors for the future. *Acta Physica Polonica A*, 116(3):389, 2009.
- [47] D. Rutledge and M. Muha. Imaging antenna arrays. *Antennas and Propagation, IEEE Transactions on*, 30(4):535 – 540, jul 1982.
- [48] E. Sakuma and K. Evenson. Characteristics of tungsten-nickel point contact diodes used as laser harmonic-generator mixers. *Quantum Electronics, IEEE Journal of*, 10(8):599 – 603, aug 1974.
- [49] Schottky. *Z. f. Physik*, 14:80, 1923.
- [50] J G Simmons. Conduction in thin dielectric films. *Journal of Physics D: Applied Physics*, 4(5):613, 1971.
- [51] John G. Simmons. Generalized formula for the electric tunnel effect between similar electrodes separated by a thin insulating film. *Journal of Applied Physics*, 34(6):1793 –1803, jun 1963.
- [52] John G. Simmons. Generalized thermal j-v characteristic for the electric tunnel effect. *Journal of Applied Physics*, 35(9):2655–2658, 1964.
- [53] J. G. Small, G. M. Elchinger, A. Javan, Antonio Sanchez, F. J. Bachner, and D. L. Smythe. ac electron tunneling at infrared frequencies: Thin-film m-o-m diode structure with broad-band characteristics. *Applied Physics Letters*, 24(6):275–279, 1974.

- [54] D. R. Sokoloff, A. Sanchez, R. M. Osgood, and A. Javan. Extension of laser harmonic frequency mixing into the 5 μm regions. *Applied Physics Letters*, 17(6):257–259, sep 1970.
- [55] T.E. Sullivan, Y. Kuk, and P.H. Cutler. Proposed planar scanning tunneling microscope diode: application as an infrared and optical detector. *Electron Devices, IEEE Transactions on*, 36(11):2659–2664, nov 1989.
- [56] Bor andlong Twu and S. E. Schwarz. Mechanism and properties of point ;contact metal ;insulator ;metal diode detectors at 10.6 μm . *Applied Physics Letters*, 25(10):595–598, nov 1974.
- [57] S. Y. Wang, T. Izawa, and T. K. Gustafson. Coupling characteristics of thin-film metal-oxide-metal diodes at 10.6 μm . *Applied Physics Letters*, 27(9):481–483, 1975.
- [58] N. Dhar F. Yesilkoy A. Akturk S. Potbhare M. Peckerar X. Shao, N. Goldsman. Simulation study of rectifying antenna structure for infrared wave energy harvesting applications. In *Proceedings of SISPAD*, pages 249–252, Denver, CO, USA, September 2012.
- [59] Filiz Yesilkoy, Kwangsik Choi, Mario Dagenais, and Martin Peckerar. Implementation of e-beam proximity effect correction using linear programming techniques for the fabrication of asymmetric bow-tie antennas. *Solid-State Electronics*, 54(10):1211–1215, 2010.
- [60] Filiz Yesilkoy, Sunil Mittal, Neil Goldsman, Mario Dagenais, and Martin Peckerar. A new process for the fabrication of planar antenna coupled ni/niox/ni tunnel junction devices. *Microelectronic Engineering*, 98(0):329–333, 2012. Special issue MNE 2011.
- [61] Jianyun Zhou and XiaoMin Yang. Monte carlo simulation of process parameters in electron beam lithography for thick resist patterning. *Journal of Vacuum Science & Technology B: Microelectronics and Nanometer Structures*, 24(3):1202–1209, 2006.